THESIS

TIME-FILTERED INVERSE MODELING OF LAND-ATMOSPHERE CARBON EXCHANGE

Submitted by

Nicholas M. Geyer

Department of Atmospheric Science

In partial fulfillment of the requirements

For the Degree of Master of Science

Colorado State University

Fort Collins, Colorado

Spring 2015

Master's Committee:

Advisor: Scott Denning

Jennifer Hoeting and Christopher O'Dell

TABLE OF CONTENTS

LIST OF TABLES

LIST OF FIGURES

CHAPTER 1

INTRODUCTION

In May 2014, carbon dioxide (CO_2) measurements taken by the National Oceanic and Atmospheric Administration (NOAA) indicated that atmospheric levels of CO_2 had risen above 400 parts per million (ppm) for the first time in recorded human history (ESRL 2014). This was determined to be the result of human activities including increased global fossil fuel consumption, cement production, and land-use change over the last 150 years (IPCC 2013; ESRL 2014). As seen in Figure 1.1, the Intergovernmental Panel on Climate Change (IPCC) Assesment Report 5 (AR5) estimates for future anthropogenic emissions of CO_2 ranged between anwhere from 6 to 25 PgC (1 PgC = 10^{15} gC), with resultant atmospheric concentrations of CO_2 estimated as somewhere between 400 and 950 parts per million (ppm) (IPCC 2013). The large range in estimated concentrations indicate that current global climate models (GCMs) are unable to accurately match historical observations and predict future emissions (IPCC 2013). This severely restricts the ability of researchers to accurately measure the effects of policy on global warming. A large contributor to the high levels of uncertainty in current estimates comes from a lack of understanding the location and magnitude of carbon cycle sinks from the atmosphere (Friedlingstein et al. 2006; Hoffman et al. 2014).

Determination of the atmospheric sources and sinks of CO_2 is a fundamental goal of carbon science for predicting future climate change. Earth's carbon cycle is comprised of both inactive and active pools of carbon. The inactive pool is carbon stored in sedimentary rock, while the three active carbon pools consist of the atmosphere, ocean, and terrestrial biosphere (UNH 2014). The estimates of the influence of CO_2 on the atmospheric and ocean pools are well observed, but biospheric CO_2 estimates need to be improved upon. Observational studies during the 1950s and 1960s suggested that in order to resolve the carbon budget there must exist a net sink of CO_2 into

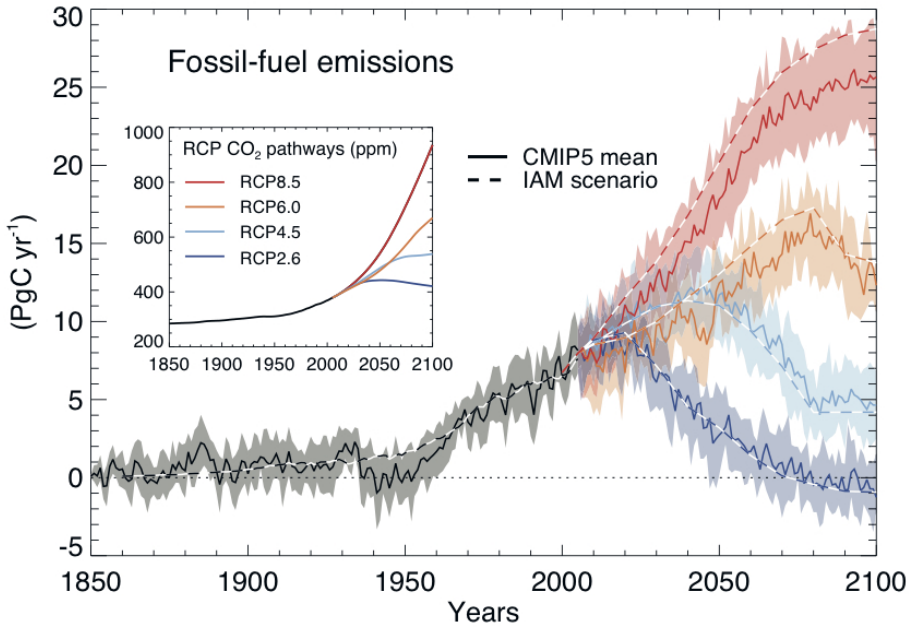

FIG. 1.1. Fossil fuel emissions scenarios from the IPCC AR5 and CMIP5 experiments. Each line represents a different emission scenario civilization could take in the future. The solid line represents the mean emissions and shaded represent the variablility the scenario could take. The nested graph represents the equivalent atmospheric concentration of CO_2. Diagram courtesy of (IPCC 2013).

both the oceans and terrestrial biosphere (Bolin and Eriksson 1958; Bolin and Keeling 1963). Over the next 50 years, observational estimates of this sink suggested that roughly 50% of anthropogenic CO_2 emissions remain in the atmosphere, while the other 50% are fluxed into the ocean and terrestrial biosphere pools (Bolin and Bischoff 1970; IPCC 2013). Oceans are well known and estimated chemistry driven sinks of CO_2 (Drever 1988; Sabine et al. 2004). The magnitude of the oceanic sink was observed to be a quarter of anthropogenic CO_2 emissions, while the other quarter is accounted for by terrestrial biosphere to close the balance (Bolin and Bischoff 1970; Ciais et al. 1995; Sabine et al. 2004). Recent estimates suggested that of the 555 PgC that humans have emitted into the atmosphere since the 1800s, the oceans and biosphere were responsible for sinking 155 ± 30 PgC and 160 ± 90 PgC, respectively (IPCC 2013). The biosphere sink estimate has an uncertainty estimation that is over half of the flux itself. Uncertainty associated with these recent estimates was

due to both the sparse number of observations available and the lack of understanding biological processes involving carbon.

To understand the biological sink, it is important to accurately measure the locations and strengths of sources and sinks of biospheric CO_2. One of the difficulties in attaining an accurate estimate of the biospheric sink is due to the fact that biology can adapt to different conditions of CO_2. Shown in figure 1.2 are the IPCC's estimations from the Coupled Model Intercomparison Project Phase 5 (CMIP5) experiment's variations of the CO_2 sink partition. These estimates showed that unlike oceans and atmosphere, the land portion of the sink varied between being a carbon source and sink of about 1 $\frac{GtC}{yr}$ to -4 $\frac{GtC}{yr}$ since the 1800s. The IPCC noted that in both the 4th and 5th assessment reports (AR4, AR5) a large source of this variation occured because of the highly sensitive reactions of global climate models' (GCMs) locations of carbon sources and sinks as well as the sensitivity of biological parameterizations (Friedlingstein et al. 2006; Hoffman et al. 2014). A way to determine the magnitude and location of this sink is through inversion modeling.

1.1. Inversion Modeling

Inversion modeling is a popular technique designed to help resolve the biases, locations, and strengths of the sources and sinks of CO_2. The inversion is a statistical model that allows an initial estimation of CO_2 fluxes, then uses an atmospheric transport model to estimate CO_2 concentrations. The inversion then uses observations to optimize biospheric fluxes in order to match CO_2 concentrations (Evensen 1994). In general, CO_2 inversion models have many more parameters to estimate than observations to constrain them. This underconstrained problem in Bayesian statistics leads to infinite solutions for flux estimates. To compensate for the lack of observations, inversion frameworks introduced aggressive regularizations to allow for more constrained estimates of CO_2.

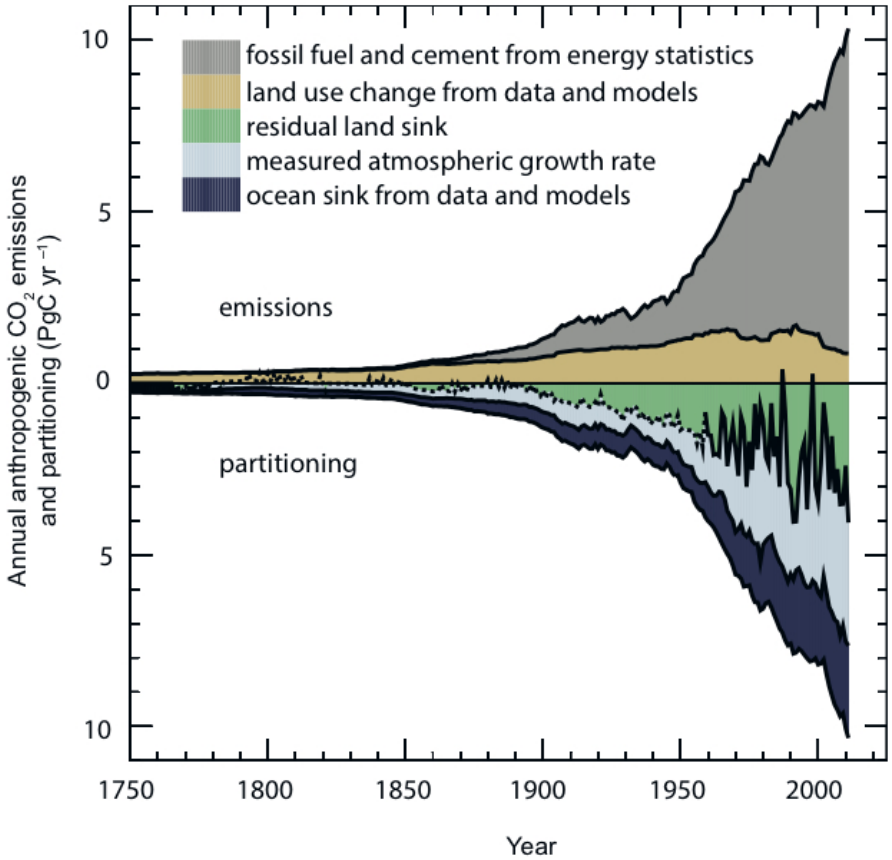

FIG. 1.2. Estimations of how anthropogenic emissions of CO_2 are being partitioned and evolving by the land and ocean carbon pools over time. Diagram courtesy of (IPCC 2013)

The creation of a large carbon flask observing network and eddy-covariance towers made it possible to use pre-aggregated observations and biological regions as early regularizations. Pre-aggregation refers to using the coarse observational network of fluxes and concentrations to associate basic flux patterns or "basis functions" with particular regions of the world. In this manner, the number of estimated flux parameters in the inversion framework is substantially lowered to compensate for the relative concentrations of available CO_2 observations. In the late 1980s, early inversion studies using spatial aggregation showed that a large Northern Hemispheric mid-latitude land CO_2 sink of 2.0 to 3.4 $\frac{PgC}{yr}$ was responsible for closing the carbon budget. This early work was plauged with source-sink errors in atmospheric transport and a sparse observational network over

the whole globe (Tans et al. 1990). In the 1990s and early 2000s, Atmospheric Tracer Transport Model Intercomparison Project (TransCom) series of experiments was one intercomparison study used to determine the strength and causes of a bias between inversion frameworks and observations (Gurney and Denning 2007). The project found the Northern Hemipheric sink estimates that generally agreed with estimates derived from eddy-covariance towers and historical carbon budget studies, however the model fluxes were lacking in precision (Baldocchi and Coauthors 2001; Baldocchi 2008; Houghton 1999). The sources of bias and uncertainty with the flux estimates were noted to be from errors arising from a combination of a sparse observing network, coarse spatial resolution, poor atmospheric transport, and poor land-model parameterizations (Law et al. 1996; Denning et al. 1999; Gurney et al. 2002, 2004; Bakwin et al. 1998; Baker et al. 2006; Kawa et al. 2004). To resolve these issues and make a better global sink estimate, the spatial resolution of observations and the models themselves had to be better. In the mid-2000s, research was focused on addressing the observing network.

By the early-to-mid-2000s, the advancements in computational resources and better models allowed studies of the problems associated with poor spatial resolution estimates. Studies during this time focused on estimating the regional-scale fluxes scaled to the resolution of the atmospheric transport model to assess the aggregation of errors when prescribed fluxes are not accurately assigned within regions (Kaminski et al. 1999; Rödenbeck et al. 2003). These studies showed that the sparse observations of fluxes and transport model resolution limits can violate the assumptions associated with the underlying Bayesian statistics of inversion models (Michalak et al. 2004). Efforts to alleviate this problem were accomplished by introducing pseudo-observations to fill in the observational gaps and incorporating either correlation length scales or geostatistical smoothing between grid-cells (Kaminski et al. 1999; Rödenbeck et al. 2003; Michalak et al. 2004; Michalak

2008). These studies reproduced similar magnitude fluxes but at a higher precision than previous work.

With spatial estimates of CO_2 fluxes possible, the focus of inversion regularizations shifted toward providing additional constraint to the background flux estimates. Prior fluxes must be measured at a regular frequency to constrain observational and modeled background fluxes. CarbonTracker and the Carbon Monitoring System (CMS) are inversion projects currently being employed for CO_2 inversions that use continuous observations of CO_2 to make estimates of these prior fluxes (Chevallier et al. 2009; Peters et al. 2007). These projects make use of a refined pre-aggregation methodology called ecoregions. Ecoregions are large expanses of land that generalize ecosystems with similar characteristics. These can be patterned on a 1° by 1° spatial grid, but are preaggregated to produce 6552 estimated parameters per year in a weekly global inversion (Peters et al. 2007; CarbonTracker 2014). Ecoregions coupled with higher resolution transport models, better land models, and eddy-covariance towers tightly constrained regional estimations of CO_2 fluxes on a weekly basis, but when downscaled to the spatial grid are not verified by flux observations (Peters et al. 2007, 2010; CarbonTracker 2014). These inversions were further constrained by including temporally regular and spatially even measurements through the use of satellite data (Liu et al. 2014). Results of these studies so far show flux estimates were comparable to TransCom3 (Chevallier et al. 2007, 2009; Chevallier and O'Dell 2013). With high resolution and temporally regular measurements of CO_2 now available, it was suggested uncertainty studies should be focused on making better biological process models (Peters et al. 2007; CarbonTracker 2014; Hurtt and Kang 2014).

Since observational platforms can provide reasonable and frequent observations, the most pressing problem remaining for improvement of inversion estimates is the development of better

land-atmosphere models. A way land-atmosphere models can be improved is through the isolation of the biological flux biases incurred from spatio-temporal flux correlations, model mistiming, and other systematic model errors on several spatio-temporal timescales. Several studies used special variants of the Bayesian inversion frameworks like maximum likelihood ensemble filters (MLEF) and ensemble Kalman filters to remove adjoint models and the need for prior fluxes in the Bayesian framework (Zupanski et al. 2007; Michalak et al. 2004). These allowed isolation of regional and global bias estimation as well as improvement in modeled fluxes using a modest number of ensemble members even with low observational constraint (Zupanski et al. 2007; Lokupitiya et al. 2008). These studies assumed that biases from net ecosystem exchange (NEE) biological fluxes were produced by the land-atmosphere models were persistant and long-lived in the estimation of gross primary production (GPP) and ecosystem respiration (RESP). This contrasts with the assimilation used by CarbonTracker in that the biases and flux estimates only had to be updated every few months rather than every week. When compared to CarbonTracker, these algorithims reduced the time dimensionality of the inversion problem by lowering the number of parameters estimated from 52 to 6 per year. This lowers the computational requirements for the inversion, which then increased the spatial resolution by design. In these frameworks rather than adjusting for the NEE biases themselves, GPP and RESP are adjusted in the following manner:

$$NEE(\lambda, \phi, t) = (1 + \beta_{RESP})RESP(\lambda, \phi, t) - (1 + \beta_{GPP})GPP(\lambda, \phi, t) \tag{1.1}$$

In this formulation, β is the bias correction factor and can vary in both time and space to correct NEE using GPP and RESP. Splitting the gross fluxes apart has two advantages. The first is increased insight into the mechanisms causing the biases in GPP and RESP separately. The second is the ability to capture the "slow-varying" biases, since both opposing gross fluxes have known

time signals, unlike more noisy NEE measurements. This methodology prevents "wasting" precious information content of the atmospheric observations on estimation of well-known ecosystem properties by focusing the corrections on persistent, scientifically valuable and statistically stable quantities with predictive power. The applications of this methodology have shown to substantially reduce large-scale carbon biases and variability and produce accurate high-resolution flux estimates (Schuh et al. 2009, 2010, 2013). While isolating the biological biases improves inversion estimates, the usage of a single term does not identify the particular slow processes in a model that make the bias. This does not provide information on where or how to improve model prior estimates. This must be addressed to provide additional constraint on inversion estimates of biological souces and sinks of CO_2.

1.2. Purpose

In each of the previously mentioned regularization methods, errors in estimated fluxes come from one or more of the following problems:

(1) Inability to isolate multiple slow-varying biases in a continuous manner.

(2) Week-to-week assimilation updates with no *a priori* knowledge of previous CO_2 fluxes.

(3) Inability to properly reconstruct the component CO_2 fluxes.

(4) Necessity for decorrelation length scales in space.

(5) Unable to estimate bias with poor observational constraints.

These issues are the focus of present day studies, but with more observational information available every day this may not be most useful route for estimating future biospheric sink studies. This research presents an alternative to using a conventional spatio-temporal regularization method by shifting the temporal aspect to a yearly temporal harmonic smoothing regulation instead. This is

accomplished by adapting the work of Zupanski et al. (2007), Schuh et al. (2009), and Lokupitiya et al. (2008) to fit a harmonic smoother to isolate multiple long-term biases in flux estimates.

A temporal smoothing regularization that is capable of assessing slow-varying flux biases in a continuous manner must be capable of assessing biases on several timescales and having the ability to "learn" about the biases over time. Under the formulation presented equation (1.1), the bias coefficients are updated every few months using both accumulated observational data and the previous assimilation cycle's posterior estimates and uncertainties in the current assimilation step (Zupanski et al. 2007; Lokupitiya et al. 2008). By doing this, the bias coefficients estimates are updated and adjusted slowly in such a way that these estimates can "learn" about the bias in order to adjust toward a stable solution as more data is assimilated in a non-isotropic way. However, these formulations are only able to estimate biases on one timescale. A single bias coefficient is insufficient to fully describe the errors from the biological parameterizations in present day land-models. For instance, errors from long-lived soil pool turnover times and shorter-lived Q^{10} parameters may result in an aliased persistent bias in respiration that is not controlled by one variable on one timescale. Using a single bias coefficient makes attribution of model parameter errors more difficult to do in a temporal regularization. A more realistic formulation can be accomplished by deconstructing the bias coefficient in equation (1.1) into several terms that are associated with yearly, seasonal, and sub-seasonal timescale flux biases as seen equation (1.2).

$$\beta = \overline{\beta} + \beta' + \beta'' \tag{1.2}$$

Where $\overline{\beta}$ is associated with yearly biases, β' is identified with seasonal scale biases, and β'' is paired with sub-seasonal bias noise. Under this decomposition, flux biases can be better attributed with the responsible mechanisms and parameterizations in models while retaining the same ability to

"learn" about the biases as more observations are assimilated. These bias coefficients can be either discretely estimated similar to present-day studies or in a harmonic sense to provide continuous estimates of flux biases. This research uses equation (1.2) in a continuous harmonic formulation estimated every year as opposed to present day week-to-week assimilation systems.

The bias coefficients of equation (1.2) should be updated annually rather than on week-to-week or monthly timescales. This effectively retains the number of estimated parameters and spatial improvements of the studies from Zupanski et al. (2007); Schuh et al. (2009); Lokupitiya et al. (2008), but allows for full years to be assimilated at once rather than in increments. Modeling efforts must be focused toward seasonal, interannual, and decadal timescales because these are the timescales needed to properly assess the growth and decay of an ecosystem. Parameterized ecological processes like the fraction of photosynthetically active radiation (fPAR), soil pool turnover times, and Q^{10} parameters are poorly understood slow varying parameterizations in land models which can produce long term variations in flux estimates that week-to-week bias corrections cannot properly address since the assimilation cycle window is too small. Errors in parameterizations like radiation, temperature, and precipitation can be assessed in a week-to-week assimilation cycle, but these are better understood and fast varying processes which need minor addressing. The flux estimates from CarbonTracker and CMS are generally good at correcting these week-to-week variations in NEE, but they are incapable of properly correcting the longer processes that can systematically underestimate or overestimate annual carbon budgets. These techniques could much more efficient if the numerical power of the observations were focused toward longer timescale biases of model flux estimates rather than week-to-week variations. There are two gains to the assimilation process when temporally smoothing to isolate long-lived biases. First, is that the flux bias estimates are fundamentally better constrained with observations. Since the bias coefficients of equation

(1.2) require at least a year's worth of data to be estimated, they are inherently better constrained with more observations. This strengthens the Gaussian assumptions in CO_2 inversions over that of weekly updates. The second advantage is that there is a computational gain by only estimating 3 to 11 bias coefficients rather than 52 bias coefficients. As previously mentioned, spatial smoothing algorithms like CarbonTracker are able to estimate a bias coefficient every week for each ecoregion. Placing this into a computational context, these regularization algorithms can estimate 52 bias coefficients every year for each ecoregion over the globe which is computationally straining and unneccessary. If the focus of the numerical power of observations were focused toward long lived biases over a yearly assimilation cycle, then the number of estimated parameters becomes 3 to 11 bias coefficients per ecoregion per year rather than 52. This means temporal smoothing regularizations require a number of operations less than or equal to that of spatial regularizations while retaining a similar spatial resolution. There is a clear advantage in using temporal smoothing regularizations over that of current regularizations, but this power is only gained once there is enough observations.

Since equation (1.2) requires at least a long enough time series of fluxes and the uncertainties of those fluxes to resolve the longest scale biases, there is an issue with obtaining a global time series of fluxes. Spatial regularizations were originally designed to compensate statistically for this lack of CO_2 observations to constrain estimates. While useful, spatial methods suffer from biases involving unequal sampling coverage and issues with decorrelation length scales. With the dawn of new carbon observing satellites like OCO-2 in orbit, there now exists the possibility to globally quantify CO_2 fluxes and their uncertainties down to roughly 250 m and below with even temporal frequency. This provides an opportunity to aggregate satellite data over a long enough time to produce a time series of fluxes for each cell or ecoregion over the globe at the resolution

of the satellite. This eliminates the unequal sampling coverage problem as well as the need for decorrelation length scales. Unfortunately, these satellite products have not been in aggregated for long enough to provide sufficient amounts of data for this study. Instead, this reasearch is developed as site-level prototype of the temporal smoothing regularization that uses eddy covariance towers from the FLUXNET network that provide hourly and half hourly observations of fluxes and the daily flux uncertainty estimates from (Barr et al. 2013) as the observational constraints over a variety of years. The usage of this data provides this study with an overconstrained inversion problem for the bias coefficients, which serves as a test bed for examining the limits of observational constraints and uncertainty for both week-to-week and temporal smoothing regularizations.

In summary, this thesis presents a technique to isolate the longer lived biases by purposely temporally smoothing modeled fluxes to remove shorter timescale variations. This can more appropriately address the biases associated with poorly understood slowly varying processes, which should produce a much better estimate of seasonal, interannual, and decadal timescale CO_2 fluxes. Through the use yearly timeseries of daily averaged GPP, RESP, and NEE observed and modeled fluxes as well as their uncertainties at an eddy covariance tower, there will be enough data to overconstrain the inversion problem and test the limits of a control algorithm mimicking week-to-week assimilation cycles and a continuous harmonic formulation of equation (1.2).

To further understand the biospheric sink, this thesis addresses the following hypotheses:

(1) A time smoothing regularization provides a better *a posteriori* interannual average of the NEE flux than that of current week-to-week assimilation algorithms across many ecosystems and uncertainty scenarios.

(2) A time smoothing regularization provides a better *a posteriori* estimate of the seasonal cycle of the NEE flux than that of current week-to-week assimilation algorithms across many ecosystems and uncertainty scenarios.

(3) A time smoothing regularization provides a better *a posteriori* interannual average of the NEE flux than that of current week-to-week assimilation algorithms when using NEE as the only constraining observational flux across many ecosystems and uncertainty scenarios.

(4) A time smoothing regularization provides a better *a posteriori* estimate of the seasonal cycle of the NEE flux than that of current week-to-week assimilation algorithms when using NEE as the only constraining observational flux across many ecosystems and uncertainty scenarios.

(5) A time smoothing regularization accurately estimates the seasonal cycle and interannual average of GPP and RESP when using NEE as the only constraining observational flux across many ecosystems and uncertainty scenarios.

(6) A time smoothing regularization provides a better *a posteriori* interannual average of the NEE flux than that of current week-to-week assimilation algorithms when using NEE and a component flux as the constraining observations across many ecosystems and uncertainty scenarios.

(7) A time smoothing regularization provides a better *a posteriori* estimate of the seasonal cycle of the NEE flux than that of current week-to-week assimilation algorithms when using NEE and a component flux as the constraining observations across many ecosystems and uncertainty scenarios.

(8) A time smoothing regularization accurately estimates the seasonal cycle and interannual average of GPP and RESP when using NEE and a component flux as the constraining observations across many ecosystems and uncertainty scenarios.

CHAPTER 2

METHODS

2.1. BIAS CORRECTION FACTORS

As seen in equation (1.2), the time smoothing algorithm was conceived by separating faster more well-understood processes like radiation and temperature from the slower less-understood processes like biogeochemistry and phenological triggers. The mapping of modeled to observed gross fluxes at any time for NEE, GPP, and RESP are given in equations (2.1) and (2.2).

$$\begin{aligned} NEE_{obs}(t) &= [1 + \beta_{RESP}(t)]\, RESP_{model}(t) - [1 + \beta_{GPP}(t)]\, GPP_{model}(t) + \epsilon \\ &= [1 + \beta_{NEE}(t)]\, NEE_{model}(t) + \epsilon \end{aligned} \tag{2.1}$$

$$\begin{aligned} GPP_{obs}(t) &= [1 + \beta_{GPP}(t)]\, GPP_{model}(t) + \epsilon \\ RESP_{obs}(t) &= [1 + \beta_{RESP}(t)]\, RESP_{model}(t) + \epsilon \end{aligned} \tag{2.2}$$

Where β is the bias correction and ϵ is an error term between the observed and modeled fluxes. GPP and RESP are capable of being optimized as a standalone fluxes or simultaneously using NEE. In these equations, β represents a multiplicative correction term to map the two vectors of fluxes on the measurement timescale. This method allows for the fluxes to vary on hourly to decadal timescales, but assumes flux biases persist on timescales longer than that of the fluxes. A single bias coefficient used in this form gives little information for what could be responsible for the errors in our models because these bias coefficients are "wasting" valuable statistical information on correcting for well-known ecosystem properties. To overcome this, β can be decomposed into three terms to separate the unknown and well-known biases, as seen in equation (1.2). Seen in table 2.1, studies have shown that the biases in our land-atmosphere are associated with various

phenological, physiological, location based biases. These parameters are multiplicative in nature,

TABLE 2.1. Possible sources of bias in SiB4

	GPP	RESP
$\overline{\beta}$	fPAR or V_{max}	Soil Pool Turnover Times ($\tau_{soil\,pools}$)
β'	Growing Degree Days or Soil Moisture	Temperature Sensitivity (Q^{10})

thus requiring the bias correction term to be multiplicative rather than additive. By decomposing β in this way, the statistical power and stability of the observational information is used toward estimating the biases in slow-varying processes only.

A continuous timeseries of the biases coefficients is preferable to discrete estimates suggested in equation (1.2). In a discrete formulation of β, there are possibilities in the winter and mistimed crops which can misrepresentative values of the biases or cause discontinuities in the estimation. To overcome this issue, a continuous formulation of the bias coefficients can be implemented. Equation (2.3) was used to introduce a harmonic and continunous timeseries of the bias coefficients.

$$\beta = \overline{\beta} + \sum_{k=1}^{L} \left(\beta_{A,k} \cos \frac{2\pi k i \Delta t}{N} + \beta_{B,k} \sin \frac{2\pi k i \Delta t}{N} \right) + \beta'' \tag{2.3}$$

$$1 < L \leq \frac{N}{2} \tag{2.4}$$

Where L is the number of total number of harmonics, k is the wavenumber, i is the i'th day of year, and N is the number of days in a year. In this formulation, the long term $\overline{\beta}$ correction and noisy β'' were retained, but β' is decomposed into component bias harmonics over a yearly timescales (I.E. N=365). As seen in equation (2.4), the βs from equation (2.3) are limited to the Nyquist frequency of the timeseries or in our case a half-yearly time signal. The benefits of estimating biases in this manner are that the interannual, seasonal, and sub-seasonal cycles are all harmonic in nature. This

means that harmonic bias coefficients can resolve these cycles much more naturally than a discrete formulation.

2.2. Kalman Filter for Harmonic βs

The optimization algorithm used in this study to estimate the bias coefficients using the observational and modeled data was the Kalman filter. The choice of the Kalman filter over the more advanced methods comes down to the fact that the length of the observational record being used is much larger than number of parameters. This means that this study, by design, is well-constrained and a Kalman filter can be used without issue.

The Kalman filter is a special case of a Bayesian Optimum Filter. This filter uses Bayes Theorem to predict the optimal gaussian distribution between a state and observations. By definition the Kalman Filter is a recursive linear Gauss-Markov least-squares unbiased estimator of a state parameter given some observations. Shown below in equation (2.5) is Bayes Theorem with respect to a state ($\vec{m}$) and the observations (d). It states that the conditional probability distribution (CDF), or likelihood, of $\vec{m}$ given a set of observations ($\vec{m}|\mathbf{d}$), the posterior, is proportional to the PDF of $\vec{m}$, the prior, times the likelihood of the measurements given the priors ($\mathbf{d}|\vec{m}$) (Evensen 2009; Welch and Bishop cited 2006).

$$P(\vec{m}|\mathbf{d}) = \frac{P(\vec{m})P(\mathbf{d}|\vec{m})}{P(\mathbf{d})} \tag{2.5}$$

To comprise the Kalman Filter, the first assumption must be to assume linearity and Markovian processes between states and observations.

$$\vec{m}_{pre} = \mathbf{A}\vec{m}_{est,prior} \tag{2.6}$$

$$\mathbf{d}_{pre} = \mathbf{G}\vec{m}_{pre} \tag{2.7}$$

Where $\mathbf{m}_t$ is the state prediction, $\mathbf{A}_{t-1}$ is the state transition matrix, $\mathbf{m}_{t-1}$ is the prior state estimation, $\mathbf{d}_{pre}$ is the observation prediction, $\mathbf{G}$ is an observational jacobian matrix. These are Markovian because the prediction of a state parameter is solely dependent upon its previous state. The last assumption is that the PDFs that formulate the state parameters and the observations are multivariate gaussian distributions in nature.

$$\begin{aligned} P(\vec{m}_t|\vec{m}_{t-1}) \sim & \mathcal{N}(\vec{m}_{t-1}, \mathbf{C}_\beta) \\ = & \frac{1}{\sqrt{(2\pi)^k|\mathbf{C}_\beta|}} e^{-\frac{1}{2}(\vec{m}-\vec{m}_{t-1})^T\mathbf{C}_\beta^{-1}(\vec{m}-\vec{m}_{t-1})} \end{aligned} \tag{2.8}$$

$$\begin{aligned} P(\mathbf{d}|G\vec{m}_t, \mathbf{C}_d) \sim & \mathcal{N}(G\vec{m}_t, \mathbf{C}_d) \\ = & \frac{1}{\sqrt{(2\pi)^k|\mathbf{C}_d|}} e^{-\frac{1}{2}(\mathbf{d}-\mathbf{G}\vec{m})^T(\mathbf{C}_d)^{-1}(\mathbf{d}-\mathbf{G}\vec{m})} \end{aligned} \tag{2.9}$$

Where $\mathbf{C}_d$ and $\mathbf{C}_\beta$ are the observational and state covariance matrices. When these are combined using Bayes Theorem, the resulting gaussian PDF describes the state in relation to the observations.

$$P(\vec{m}_t|\mathbf{d}, \mathbf{C}_d) \propto e^{-\frac{1}{2}\left[(\vec{m}-\vec{m}_{t-1})^T\mathbf{C}_\beta^{-1}(\vec{m}-\vec{m}_{t-1})+(\mathbf{d}-\mathbf{G}\vec{m})^T(\mathbf{C}_d)^{-1}(\mathbf{d}-\mathbf{G}\vec{m})\right]} \tag{2.10}$$

The exponent in equation (2.10) represents a cost function (Ψ) which is a balance of what is the best possible estimate of what state is between the observations and prior state estimate, seen in

equation (2.11).

$$\Psi = \left[(\vec{m} - \vec{m}_{t-1})^T \mathbf{C}_{\beta}^{-1}(\vec{m} - \vec{m}_{t-1}) + (\mathbf{d} - \mathbf{G}\vec{m})^T (\mathbf{C}_d)^{-1}(\mathbf{d} - \mathbf{G}\vec{m})\right] \tag{2.11}$$

This balance is determined by how much variance there is between both the observations and the state estimates themselves (Evensen 2009). The cost function is minimized by taking the derivative of the estimated state and setting the resulting equation equal to zero. When this occurs, the state estimation the PDF of the posterior estimates of $\vec{m}$ will be maximized. From the minimization of this function, the evidence to have strong prior state estimates can be seen. If the state is well constrained with strong estimates, then belief can be high in the posterior state estimates. With some algebra following from (Evensen 2009), the minimization of the cost function becomes what is commonly known as the Kalman filter equations.

The Kalman filter equations used in this study with respect to β are seen in (2.12) through (2.19).

$$\mathbf{d}_{pre} = \mathbf{G}\vec{m}_{est,prior} \tag{2.12}$$

$$\mathbf{C}_{\beta,pre} = \mathbf{C}_{\beta,est,prior} \tag{2.13}$$

$$\mathbf{S} = \mathbf{G}^T\mathbf{C}_{\beta,pre}\mathbf{G} + \mathbf{C}_d \tag{2.14}$$

$$\mathbf{K} = \mathbf{S}^{-1}\mathbf{G}^T\mathbf{C}_{\beta,pre} \tag{2.15}$$

$$\tilde{\mathbf{I}} = \mathbf{d} - \mathbf{G}\vec{m}_{prior} \tag{2.16}$$

$$\begin{aligned} \vec{m}_{est} &= \vec{m}_{pre} + \mathbf{K}\tilde{\mathbf{I}} \\ &= \vec{m}_{pre} + \left(\mathbf{G}^T\mathbf{C}_{\beta,pre}\mathbf{G} + \mathbf{C}_d\right)^{-1}\mathbf{G}^T\mathbf{C}_{\beta,pre}\left(\mathbf{d} - \mathbf{G}\vec{m}_{prior}\right) \end{aligned} \tag{2.17}$$

$$\mathbf{C}^*_{\beta,est} = (\mathbf{I} - \mathbf{KG})\mathbf{C}_{\beta,pre}(\mathbf{I} - \mathbf{KG})^T + \mathbf{KC}_d\mathbf{K}^T \tag{2.18}$$

$$\mathbf{C}_{\beta,est} = \mathbf{C}^*_{\beta,est}(W) + \mathbf{C}_{\beta,pre}(1 - W) \tag{2.19}$$

Where $\mathbf{G}$ is a jacobian matrix for $\vec{m}$ to map the state onto the observations, $\mathbf{d}$ is a matrix of observations, and $\vec{m}$ is now a vector of the state of β either prior or posterior. The terms $\tilde{\mathbf{I}}$ and $\mathbf{S}$ represent the innovation matrices for both the predicted state and covariance states of β. The K matrix is known as the "Kalman Gain" matrix and it moderates the predicted values to make $\vec{m}_{est}$ and $C_{\beta,est}$. Equation (2.18) for $C_{\beta,est}$ is known as the "Joesph's Form" of the state covariance update equation. This is not typically seen in many studies because it is usually a little more computationally inefficient than what is usually shown for the Kalman filter, but if the Kalman Gain is optimal it will coverge toward usual optimal solution. The reason this is being used is that the state covariance update step can be vulnerable to round off errors, which breaks a symmetry

assumption during the derivation. If this occurs, then update step will become negative. This is not allowed by the filter's assumptions and will break the algorithm entirely. Additionally, W is a tuning parameter between 0 and 1 that artificially inflates the posterior covariance matrix of β. This is done because there lies another mathematical possibility that the filter will become too certain of the estimates that the covariance of the PDFs will converge to zero. If this occurs, it is impossible to estimate or update the state and mathematically this will lead to the filter estimating infinite solutions. The form for covariance inflation used in equation (2.19) was originally proposed by (Zhang et al. 2004).

The initialization of $\vec{m}$ used in this study is prescribed in equation (2.20).

$$\vec{m}_{prior} = \Re^{M\times 1} = \begin{pmatrix} 1 \\ \overline{\beta} \\ \beta_{A,j=1} \\ \beta_{B,j=1} \\ \vdots \\ \beta_{A,j=L} \\ \beta_{B,j=L} \end{pmatrix} = \begin{pmatrix} 1 \\ 0 \\ \vdots \\ 0 \end{pmatrix} \tag{2.20}$$

Where M is the number of β to be estimated and j is the harmonic number from 1 to the maximum harmonic number, L. J is currently designed to be manually assigned by the user, but can be assigned in three ways. The first is to simply assign an arbitrary number of harmonics (I.E. L = 3 harmonics). The second way is to use known harmonics in the flux cycle (I.E. seasonal (k=1), daily (k=365), etc). The final way is to use a fourier transform to obtain the wavenumbers associated with a particular percent of the variance with the errors between the observations and the model.

The jacobian matrix, $\mathbf{G}$, is assigned as the following:

$$G = N \times M \tag{2.21}$$

$$= \begin{pmatrix} Mod_{i=1} & Mod_{i=1} & Mod_{i=1}\cos(\omega_1 1) & Mod_{i=1}\sin(\omega_1 1) & \cdots & Mod_{i=1}\cos(\omega_j 1) & Mod_{i=1}\sin(\omega_j 1) \\ \vdots & \vdots & \vdots & \vdots & \vdots & \vdots & \vdots \\ Mod_{i=N} & Mod_{i=N} & Mod_{i=N}\cos(\omega_1 i) & Mod_{i=N}\sin(\omega_1 i) & \cdots & Mod_{i=N}\cos(\omega_j i) & Mod_{i=N}\sin(\omega_j i) \end{pmatrix}$$

$$\omega_j = \frac{2\pi j}{N} \tag{2.22}$$

Where N is the number of observation/modeled data points. For each harmonic or the mean, two corresponding timeseries of modeled gross flux values are multiplied by the corresponding harmonic. This allows isolation of just the mean and harmonic coefficients for β.

The observation and state covariance matrices are assigned as seen in (2.23) through (2.25).

$$\mathbf{d} = \mathfrak{R}^{N\times 1} = \begin{pmatrix} Obs_{i=1} \\ \vdots \\ Obs_{i=N} \end{pmatrix} \tag{2.23}$$

$$\mathbf{C}_\beta = \mathfrak{R}^{M\times M} = \begin{pmatrix} \sigma_1^2 & 0 & \cdots & \cdots & 0 \\ 0 & \sigma_{\overline{\beta}}^2 & 0 & \cdots & \vdots \\ \vdots & 0 & \sigma^2_{\beta_{A,k=1}} & 0 & \vdots \\ \vdots & \vdots & 0 & \ddots & 0 \\ 0 & \cdots & \cdots & \cdots & \sigma^2_{\beta_{B,k=L}} \end{pmatrix} \tag{2.24}$$

$$\mathbf{C}_d = \mathfrak{R}^{N\times N} = \begin{pmatrix} \sigma^2_{obs,i=1} & 0 & \cdots & \cdots & 0 \\ 0 & \sigma^2_{obs,i=2} & 0 & \cdots & \vdots \\ \vdots & 0 & \sigma^2_{obs,i=3} & 0 & \vdots \\ \vdots & \vdots & 0 & \ddots & 0 \\ 0 & \cdots & \cdots & \cdots & \sigma^2_{obs,i=N} \end{pmatrix} \tag{2.25}$$

The off-diagonal terms in the observational covariance matrix are assumed to be zero for a 1 flux observation filter (a 2-flux filter is later described). This is because the flux uncertainty estimates used here were summed in quadrature and are independent of one another (Barr et al. 2013).

The filter should be implemented in a algorithm similar to the flow chart presented in 2.1

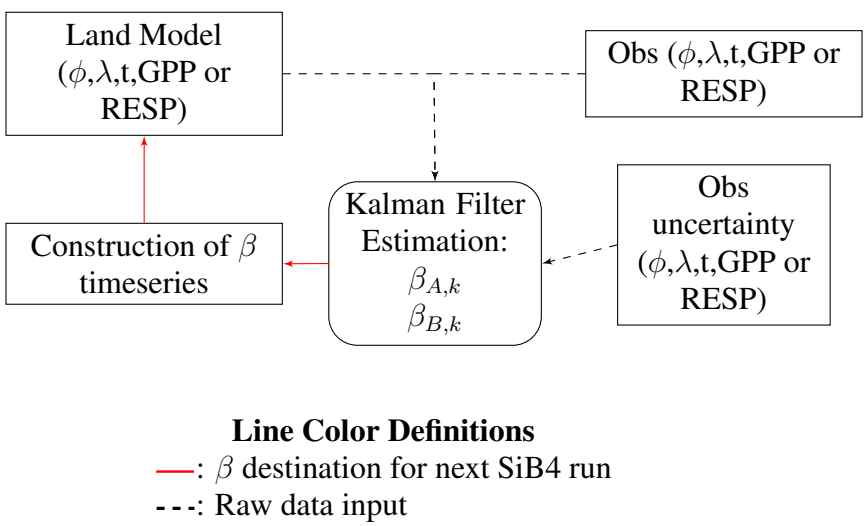

FIG. 2.1. Kalman Filter estimation procedure. Shown is one assimilation cycle.

2.3. CARBON FLUX TOWER NETWORK

This study used flux records from 8 different eddy covariance (EC) towers from FLUXNET network to comprise the observational data used in equation (2.23) of the Kalman filter. The usage of flux towers allowed this study to use high quality direct measurements of the component and

net fluxes to well-constrain the inversion to test the hypotheses. Figure 2.2 shows the location of all the EC towers we used. A brief site summary and references to more indepth EC tower site descriptions and methods are given in Table 2.2. When choosing these sites, it was important to choose towers that had complete or very near-complete (>99%) data records of NEE, RESP, and GPP. At the lowest level of quality control, most sites have long "missing data" gaps for various reasons that make conventional statistical methods difficult to handle with strong significance. To avoid this problem, we used data from the the North American Carbon Program Site Synthesis Dataset.

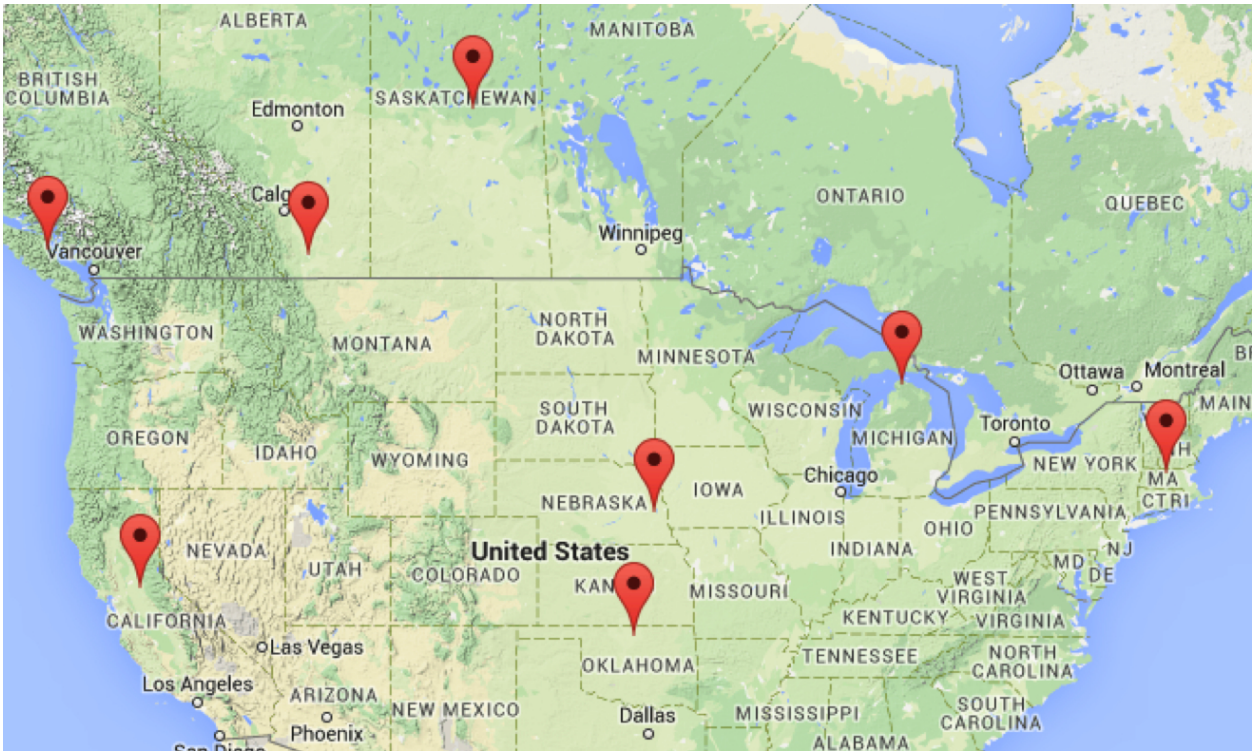

FIG. 2.2. Map of tower sites used in this study. Created using Google Maps.

TABLE 2.2. Observational Site Descriptions

Site Name	Site Code	Latitude	Longitude	PFT Type	Years Used	PI	Site References
Lethbridge	CA-Let	49.709	-112.940	C3 grass	2000-2006	Lawrence Flanagan	(Flanagan and Adkinson 2011)
Campbell River	CA-Ca1	49.867	-125.333	ENF	1998-2006	Andrew T. Black	(Krishnan et al. 2009)
U of Michigan Biological Station	US-UMB	45.559	-84.713	DBF	2004-2006	Gil Bohrer	(Gough et al. 2008)
Vaira Ranch	US-Var	38.406	-120.950	C3 grass	2001-2007	Dennis Baldocchi	(Ma et al. 2007)
Mead-Irrigated	US-Ne1	41.165	-96.476	Maize/Soy, Wheat	2002-2012	Andrew E. Suyker	(Verma et al. 2005) (Suyker and Verma 2010)
Harvard Forest	US-Ha1	42.537	-72.171	DBF	1997-2004	Bill Munger	(Urbanski et al. 2007)
ARM-Oklahoma SGP Main	US-ARM	36.605	-97.488	Maize/Soy, Wheat	2003-2006	Marc Fischer	(Fischer et al. 2007)
Old Black Spruce	CA-Obs	53.987	-105.118	ENF	2000-2006	Andrew T. Black	(Krishnan et al. 2008) (Kljun et al. 2006)

2.3.1. North American Carbon Program (NACP) Site Synthesis

The primary source of observed fluxes were provided by The North American Carbon Program (NACP). This was a multiyear integrated research program supported designed to understand, predict, and quantify the budgets and fluxes of carbon dioxide, carbon monoxide, and methane over North America. The site synthesis was an intercomparison of 39 EC towers from FLUXNET simulated by 24 different land-atmosphere models from the beginning of a EC tower's flux record until 2006, if capable.

NACP tower NEE, RESP, and GPP measurements are empirically derived quantities eddy-covariance measurements using modified FLUXNET-Canada decomposition technique. Measured NEE was the result of summing eddy-covariance and air-column storage fluxes of CO_2 integrated from 10 Hz measurements of eddy covariance measurements every 30 minutes. NEE measurements were adjusted for known energy closure issues using the Bowen Ratio and filtered for low nighttime friction velocity measurements. NEE was then regressed with temperature to derive an emperical exponential relationship each year. This relationship is then applied to respiration over the year of record. When photosynthesis was favorable, GPP was estimated as the difference between measured respiration and NEE, otherwise it was assumed to be zero. GPP and RESP missing data gaps were filled by estimating using the linear regression coefficient of a 100 point moving window between modeled and observed GPP or RESP measurements. Please see Barr et al. (2004) for a more indepth analysis of the data preparation.

Sources of uncertainty accounted for in this dataset are from gap-filling algorithm, random variations, threshold friction velocity and partitioning uncertainties (Schaefer et al. 2012). Random and threshold friction velocity uncertainties were estimated using the from the 95% confidence interval from a 1000 Monte Carlo realizations of a RESP, NEE, and GPP estimates (Barr

et al. 2013; Richardson and Hollinger 2007). Gap filling uncertainty was formulated from the standard deviation between 15 different methodolgies and the fraction of filled gaps per day (Moffat et al. 2007). Partitioning uncertainty was derived from the standard deviations of 23 different partitioning methodologies and observed values (Desai et al. 2008). These uncertainties are summed in quadrature and are assumed to be uncorrelated (Schaefer et al. 2012). The estimates used are provided on several timescales from half-hourly to annual estimates (Barr et al. 2013). These uncertainty estimates are used for the observational covariance matrix seen in equation (2.25).

2.4. Simple Biosphere Model 4

The land model data used the $\mathbf{G}$ Jacobian matrix was the Simple Biosphere Model 4 (SiB4). SiB4 is the fourth and most advanced version of the Simple Biosphere model originally proposed by Sellers et al. (1986). The original SiB framework was built for usage in atmospheric general circulation models (AGCMs) to exchange mass and energy between the surface and the atmosphere. The second version of SiB, SiB2, was developed upon the work of Sellers et al. (1996b, 1992) and Denning et al. (1996). SiB2 introduced new C4 photosynthesis parameterizations, improved stomatal conductance parameterizations, and satellite based vegetation phenology (Collatz et al. 1992; Sellers et al. 1996a, 1992). SiB3 updated the SiB2 for more modern hydrology and energy exchange parameterizations between the surface and the atmosphere (Baker et al. 2008). The advancements within SiB4 presented a framework that combines the usage of prognostic phenology, crop, and terrestrial carbon pool models to grow, senesce and turnover several flows of carbon throughout the biosphere. Figure 2.3 shows schematically how SiB4 operates. Important model highlights are presented below, but refer to Haynes et al. (2013) for more technical specifics.

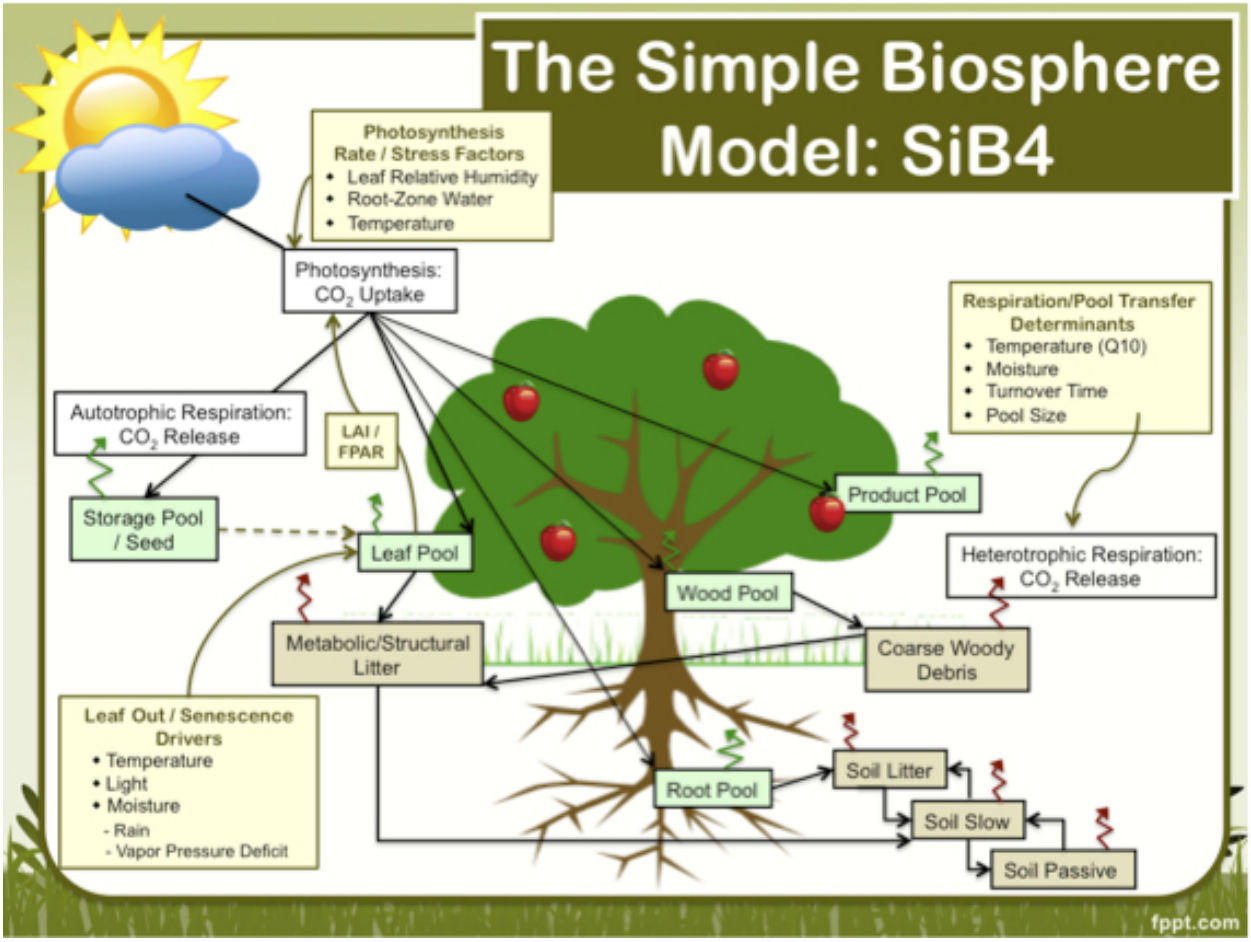

FIG. 2.3. Shown is a representation of how SiB4 treats the cycling of carbon. Figure is courtesy of Haynes et al. (2013).

2.4.1. SiB4: Prognostic Phenology and Photosynthesis

In SiB4 has the capability to prognostically derive phenological quantities for vegetation in its "Prognostic Phenology" module. The framework intakes emperically derived temperature, light, and moisture factors as well as carbon stock data to diagnose both leaf area index (LAI) and the fraction of photosynthetically active radiation (fPAR) as prognostic variables. By using both the leaf growth, environmental stresses and fPAR, SiB4 determines the magnitude of photosynthesis (Stöckli et al. 2008; Jolly et al. 2005; Stöckli et al. 2011).

Leaf-scale photosynthesis is based upon the stomatal conductance work of Collatz et al. (1992); Ball (1988) and limited by the carboxylation enzyme kinetics of rubisco (Farquhar et al. 1980; Collatz et al. 1991). This is upscaled into a bulk canopy photosynthesis integration and regulated by the canopy air space parameterizations for ecosystem-scale balancing (Sellers et al. 1996b; Baker et al. 2008).

2.4.2. SiB4: Respiration and Carbon Pools

SiB4 operates with 11 carbon pools to simulate the cycling of carbon through the biosphere. There are 5 living carbon pools and 6 inactive carbon pools which are updated daily in the model. As SiB4 photosynthesizes, the vegetation will either respire carbon via autotrophic respiration or allocate it into the living pools for building new biomass or maintainence. The magnitude of what is allocated into a living pool depends upon the ecosystem's phenological state and vegetation composition. Once introduced into the ecosystem as living biomass, SiB4 uses a cascading series of carbon pools each with their own turnover times and controls to limit the amount of carbon being passed through to the next stage in the series until it is released via heterotrophic respiration (Denning et al. 1996; Lokupitiya et al. 2009; Haynes et al. 2013).

The respiration in SiB4 is formulated from autotrophic and heterotrophic respiration between the plant and surface surface pools (Denning et al. 1996). Respiration in SiB4 is a function of soil moisture, temperature, and pool size. The autotrophic parameterizations are applied to the live pools and the heterotrophic respiration to the surface and soil pools. Every year the gross annual photosyntheic production is balanced by the respiration to allow for a net-zero annual NEE.

2.4.3. SiB4: Plant Functional Types

SiB4 uses 24 plant functional types (PFT) unlike prevous versions used that 15 IGPB Biome classifications of ecosystems. As seen in table 2.3, PFTs in SiB4 include 1 desert type, 8 tree types, 3 shrublands types, 5 grassland types, and 7 crops types. These are distinguished by vegetation characteristic and climate regime. Using PFTs over Biomes allows SiB4 to more accurately describe the phenological characteristics of an ecosystem. Beyond this SiB4 also has the capability of making a multi-PFT grid cell can represent the mosaic of land heterogeneity which is more representative of the real land cover rather than a single biome (Bonan et al. 2002).

Table 2.3. Description of PFTs present in SiB4

PFT Number	PFT Code	PFT Description
1	des_all	Desert
2	enf_tem	Temperate Evergreen Needleleaf Forest
3	enf_bor	Boreal Evergreen Needleleaf Forest
4	dnf_bor	Boreal Deciduous Needleleaf Forest
5	ebf_tro	Tropical Evergreen Broadleaf Forest
6	ebf_tem	Temperate Evergreen Broadleaf Forest
7	dbf_tro	Tropical Deciduous Broadleaf Forest
8	dbf_tem	Temperate Deciduous Broadleaf Forest
9	dbf_bor	Boreal Deciduous Broadleaf Forest
10	ebs_tro	Tropical Evergreen Broadleaf Shrub
11	dbs_tem	Temperate Deciduous Broadleaf Shrub
12	dbs_bor	Boreal Deciduous Broadleaf Shrub
13	c3g_tro	Tropical C3 Grass
14	c3g_tem	Temperate C3 Grass
15	c3g_bor	Boreal C3 Grass
16	c4g_tro	Tropical C4 Grass
17	c4g_tem	Temperate C4 Grass
18	cro_tro	Tropical Generic Crop
19	cro_tem	Temperate Generic Crop
20	mze_tro	Tropical Maize Crop
21	mze_tem	Temperate Maize Crop
22	soy_tro	Tropical Soy Crop
23	soy_tem	Temperate Soy Crop
24	wwt_tem	Temperate Winter Wheat Crop

2.4.4. SiB4: Model Set-up

SiB4 was run as a single point directly over the simulated sites. Inputs required include a vegetation phenology, physiology, and carbon pool look-up tables that SiB4 requires to initialize and calculate various quantities. The driver meteorology supplied to SiB4 was from the MERRA .5° by .5° gridded reanalysis dataset over the observed record. Additionally, a spin-up run to the model was required to bring the carbon pools to equilibrium. This spin-up was no more than 7 cycles over the length of observed record. Once our pools reached equilibrium, we ran SiB4 over the observed record one more time and stored the output for analysis.

2.5. Experimental Design

The net and component flux estimations are prepared for the hypotheses and their certainty tests by means of three different experiments involving the time smoothing algorithm and the control algorithm. These experiments were designed to mimic past, present, and future applications of this algorithm. The exact experiments are described below. As shown in table 2.4, the data created from these experiments are used to directly address the hypotheses outlined in section 1.2 in various manners.

Table 2.4. Experiments used to explore the hypotheses outlined in section 1.2

	Experiment 1	Experiment 2	Experiment 3
Hypothesis 1	✓	-	-
Hypothesis 2	✓	-	-
Hypothesis 3	-	✓	-
Hypothesis 4	-	✓	-
Hypothesis 5	-	✓	-
Hypothesis 6	-	-	✓
Hypothesis 7	-	-	✓
Hypothesis 8	-	-	✓

The control algorithm used in all three experiments to estimate NEE is analgous to the one used in CarbonTracker. The basic algorithm used in CarbonTracker is a weekly updated bias

coefficient for estimates of NEE only. These bias coefficients are estimated once and are not used as *a priori* information for future assimilation cycles. Furthermore, the updated state covariance matrix does not progress forward in time either. Thus the control algorithm estimates 52 separate and independent single bias coefficients of NEE in a year (CarbonTracker 2014). It has been shown to be highly useful for estimating week-to-week variations in CO_2, but may be unable to properly match the yearly and annual cycles of CO_2.

The control algorithm in this study used the same Kalman filter and initial conditions as the time smoothing algorithm, but instead of yearly assimilation cycles with progressive state covariance updates, it used a new initializations of the state priors and covariance matrix.

A summary of the set ups and tests for the three experiments between the control and time smoothing algorithms are seen in table 2.5.

TABLE 2.5. Experiment 1, 2, and 3's set up for variables and tests

	Time Smoothing	Control
Experiment 1: Variable(s) Optimized	NEE	NEE
Experiment 2: Variable(s) Optimized	NEE	NEE
Experiment 3: Variable(s) Optimized	NEE and GPP	NEE
Experiment 1: Variable(s) Used	NEE	NEE
Experiment 2: Variable(s) Used	GPP and RESP	NEE
Experiment 3: Variable(s) Used	GPP and RESP	NEE
Number of harmonics (L)	5	N/A
Experiment 1: Number of Parameters Optimized	11	52
Experiment 2: Number of Parameters Optimized	22	52
Experiment 3: Number of Parameters Optimized	22	52
Observational Uncertainty	(Barr et al. 2013)	(Barr et al. 2013)
Observational Uncertainty Tests	2x, 5x, 10x	2x, 5x, 10x
Initial β Uncertainty	.9	.9
Tuning Parameter (W)	0.4	0

2.5.1. Experiment 1: NEE optimized from NEE

The first experiment is an "apples-to-apples" comparison of the estimation of the mean and seasonal errors of modeled NEE given direct measurements of NEE. This is analagous to estimating NEE from CO_2 in a conventional atmospheric inversion because only NEE changes the concentrations of atmospheric CO_2.

The equations being used by time-smoothing algorithm and the control algorithms in Experiment 1 are shown in equations (2.26) and (2.27).

$$NEE_{obs,control}(t) = [1 + \beta_{NEE}(t)]\, NEE_{model}(t) + \epsilon \tag{2.26}$$

$$NEE_{obs,TS}(t) = \left[1 + \overline{\beta} + \sum_{k=1}^{L} \left(\beta_{A,k} \cos \frac{2\pi k i \Delta t}{N} + \beta_{B,k} \sin \frac{2\pi k i \Delta t}{N} \right) \right] NEE_{model}(t) + \epsilon \tag{2.27}$$

As previously stated, both algorithms used the same initial conditions and Kalman filter equations. The initial (β) uncertainty was set to .9 for all parameters ($\sigma_\beta = .9$) and was inflated during the update step with a weighting factor of .5 (W=0.5). The observational uncertainty was prescribed from Barr et al. (2013) and updated for each assimilation cycle.

Once each algorithm were run using the prescribed condition, additional tests were run using various amounts of uncertainty in both β and the observations. Since atmospheric inversions have problems with dilution and wind advection of the NEE signal, flux towers provide much stronger observational constraint. It is reasonable to assume that if the findings of this study were applied to a full scale atmospheric inversion, tests of the observational certainty must be done. To do this, this experiment applied increased observational uncertainties of 2, 5, and 10 times the given the estimates from Barr et al. (2013).

2.5.2. Experiment 2: GPP and RESP optimized from NEE

The second experiment attempted to use the component GPP and RESP fluxes to formulate a prior NEE estimate which was optimized by observed NEE. This experiment is similar previous studies by (Zupanski et al. 2007), (Lokupitiya et al. 2008), and (Schuh et al. 2009, 2010, 2013). NEE is still being optimized by observed NEE, however the estimated biases are now representative of the patterns in GPP and RESP, not NEE.

The control algorithm remained composed from equation (2.26), but the time smoothing algorithm was updated to optimize equation (2.28).

$$NEE_{obs,TS}(t) = \left[1 + \overline{\beta}_{RESP} + \sum_{k=1}^{L}\left(\beta_{RESP,A,k}\cos\frac{2\pi ki\Delta t}{N} + \beta_{RESP,B,k}\sin\frac{2\pi ki\Delta t}{N}\right)\right] RESP_{model}(t)$$
$$- \left[1 + \overline{\beta}_{GPP} + \sum_{k=1}^{L}\left(\beta_{GPP,A,k}\cos\frac{2\pi ki\Delta t}{N} + \beta_{GPP,B,k}\sin\frac{2\pi ki\Delta t}{N}\right)\right] GPP_{model}(t) + \epsilon \quad (2.28)$$

When solving for both β_{GPP} and β_{RESP} at the same time using NEE state estimation, reformulation of the $\mathbf{G}$, $\vec{m}$, and $\mathbf{C}_\beta$ matrices was needed. These matrices are changed via equations (2.29) through (2.31) and are subbed into the Kalman filter accordingly.

$$\vec{m}_{prior} = \Re^{2M\times 1} = \begin{pmatrix} 1 \\ \overline{\beta}_{RESP} \\ \beta_{RESP,A,k=1} \\ \beta_{RESP,B,k=1} \\ \vdots \\ \beta_{RESP,A,k=L} \\ \beta_{RESP,B,k=L} \\ 1 \\ \overline{\beta}_{GPP} \\ \beta_{GPP,A,k=1} \\ \beta_{GPP,B,k=1} \\ \vdots \\ \beta_{GPP,A,k=L} \\ \beta_{GPP,B,k=L} \end{pmatrix} = \begin{pmatrix} 1 \\ 0 \\ \vdots \\ 0 \\ 1 \\ 0 \\ \vdots \\ 0 \end{pmatrix} \tag{2.29}$$

$$\mathbf{G} = \Re^{N\times 2M}$$

$$= \begin{pmatrix} SiB_{R,1} & SiB_{R,1} & SiB_{R,1}\cos(\omega_k 1) & SiB_{R,1}\sin(\omega_k 1) & -SiB_{G,1} & -SiB_{G,1} & -SiB_{G,1}\cos(\omega_k 1) & -SiB_{G,1}\sin(\omega_k 1) \\ \vdots & \vdots & \vdots & \vdots & \vdots & \vdots & \vdots & \\ SiB_{R,N} & SiB_{R,N} & SiB_{R,N}\cos(\omega_k N) & SiB_{R,N}\sin(\omega_k N) & -SiB_{G,N} & -SiB_{G,N} & -SiB_{G,N}\cos(\omega_k N) & -SiB_{G,N}\sin(\omega_k N) \end{pmatrix} \tag{2.30}$$

$$\mathbf{C}_\beta = \Re^{2M\times 2M} = \begin{pmatrix} \sigma^2_{1,RESP} & 0 & \cdots & \cdots & \cdots & \cdots & \cdots & 0 \\ 0 & \sigma^2_{\overline{\beta}_{RESP}} & 0 & \cdots & \cdots & \cdots & \cdots & \vdots \\ \vdots & 0 & \sigma^2_{\beta_{RESP,A,k=1}} & 0 & \cdots & \cdots & \cdots & \vdots \\ \vdots & \vdots & 0 & \ddots & \cdots & \cdots & \cdots & \vdots \\ \vdots & \cdots & \cdots & 0 & \sigma^2_{\beta_{RESP,B,k=L}} & 0 & \cdots & \vdots \\ \vdots & \cdots & \cdots & \cdots & 0 & \sigma^2_{1,GPP} & 0 & \vdots \\ \vdots & \cdots & \cdots & \cdots & \cdots & 0 & \ddots & 0 \\ 0 & \cdots & \cdots & \cdots & \cdots & \cdots & 0 & \sigma^2_{\beta_{GPP,B,k=L}} \end{pmatrix} \tag{2.31}$$

The initial (β) uncertainty was set to .9 for all parameters ($\sigma_\beta = .9$) and was inflated during the update step with a weighting factor of .5 (W=0.5). GPP and RESP were reconstructed for hypothesis and significance testing via equations (2.32) and (2.33).

$$RESP_{est,TS}(t) = \left[1 + \overline{\beta}_{RESP} + \sum_{k=1}^{L}\left(\beta_{RESP,A,k}\cos\frac{2\pi ki\Delta t}{N} + \beta_{RESP,B,k}\sin\frac{2\pi ki\Delta t}{N}\right)\right] RESP_{model}(t) + \epsilon \tag{2.32}$$

$$GPP_{est,TS}(t) = \left[1 + \overline{\beta}_{GPP} + \sum_{k=1}^{L}\left(\beta_{GPP,A,k}\cos\frac{2\pi ki\Delta t}{N} + \beta_{GPP,B,k}\sin\frac{2\pi ki\Delta t}{N}\right)\right] GPP_{model}(t) + \epsilon \tag{2.33}$$

Like Experiment 1, once each algorithm was using the prescribed conditions, applications of increased observational uncertainties of 2, 5, and 10 times the given the estimates from Barr et al. (2013) were used to test limits of the algorithms.

2.5.3. Experiment 3: RESP and GPP optimized from NEE and GPP

The third experiment is analgous to a CO_2 inversion where additional observational data such as fluorescence or carbonyl sulfide is able to constrain one of the two component fluxes. With the advent of more advanced carbon observing satellites like GOSAT and OCO-2, these satellite products are able becoming more likely to be used in the future to help constrain inversion estimates. This experiment replicates the uncertainty tests of the first two experiment, but this time uses both observed NEE and GPP fluxes to diagnose the biases in modeled GPP and NEE.

The control algorithm remained composed from equation (2.26). The time smoothing algorithm was updated to use equations (2.33) and (2.27) in tandem for prior estimates of GPP and NEE. Ideally, this should not only optimize NEE and GPP, but also optimize RESP by construction. The Kalman filter algorithm was updated with $\vec{m}$ and $\mathbf{C}_\beta$ matrices from equations (2.29) and

(2.31). The matrices $\mathbf{d}$, $\mathbf{G}$, and $\mathbf{C}_d$ are updated to equations (2.34) through (2.36). This observational covariance matrix now has off-diagonal elements to communcate changes between day-to-day uncertainty estimates between GPP and NEE. This was not part of the original uncertainty estimates provided, but it was found that there are issues when assuming zero value off-diagonal covariances in this version of the assimilation algorithm.

$$\mathbf{d} = \Re^{2N\times 1} = \begin{pmatrix} NEE_{i=1} \\ \vdots \\ NEE_{i=N} \\ GPP_{i=1} \\ \vdots \\ GPP_{i=N} \end{pmatrix} \tag{2.34}$$

$$\mathbf{G} = \Re^{2N\times 2M}$$

$$= \begin{pmatrix} SiB_{R,1} & SiB_{R,1} & SiB_{R,1}\cos(\omega_k 1) & SiB_{R,1}\sin(\omega_k 1) & -SiB_{G,1} & -SiB_{G,1} & -SiB_{G,1}\cos(\omega_k 1) & -SiB_{G,1}\sin(\omega_k 1) \\ \vdots & \vdots & \vdots & \vdots & \vdots & \vdots & \vdots & \\ SiB_{R,N} & SiB_{R,N} & SiB_{R,N}\cos(\omega_k N) & SiB_{R,N}\sin(\omega_k N) & -SiB_{G,N} & -SiB_{G,N} & -SiB_{G,N}\cos(\omega_k N) & -SiB_{G,N}\sin(\omega_k N) \\ 0 & 0 & 0 & 0 & SiB_{G,1} & SiB_{G,1} & SiB_{G,1}\cos(\omega_k 1) & SiB_{G,1}\sin(\omega_k 1) \\ \vdots & \vdots & \vdots & \vdots & \vdots & \vdots & \vdots & \\ 0 & 0 & 0 & 0 & SiB_{G,N} & SiB_{G,N} & SiB_{G,N}\cos(\omega_k N) & SiB_{G,N}\sin(\omega_k N) \end{pmatrix} \tag{2.35}$$

$$\mathbf{C}_d = \mathfrak{R}^{2N\times 2N} = \begin{pmatrix} \sigma^2_{NEE,obs,i=1} & 0 & \cdots & \sigma^2_{NEE,GPP,obs,i=1} & \cdots & 0 \\ 0 & \ddots & 0 & \cdots & \cdots & \vdots \\ \vdots & 0 & \sigma^2_{NEE,obs,i=N} & 0 & \cdots & \sigma^2_{NEE,GPP,obs,i=N} \\ \sigma^2_{GPP,NEE,obs,i=1} & \cdots & 0 & \sigma^2_{GPP,obs,i=1} & 0 & \vdots \\ \vdots & \cdots & \cdots & 0 & \ddots & 0 \\ 0 & \cdots & \sigma^2_{GPP,NEE,obs,i=N} & \cdots & 0 & \sigma^2_{GPP,obs,i=N} \end{pmatrix} \tag{2.36}$$

Where $\sigma^2_{NEE,GPP,obs}$ for any particular day was computed from equation (2.37).

$$\sigma^2_{NEE,GPP,obs} = \frac{\sigma^2_{NEE,obs} - \sigma^2_{GPP,obs}}{2} \tag{2.37}$$

2.6. Hypotheses Testing and Significance

As stated in section 1.2, there are four hypotheses being tested by the time smoothing algorithm in this study. Once the data was prepared in one of the experiments in section 2.5, this study then administered a possible five step evaluation to provide visual, qualitative, and quantitative evidence of the time smoothing algorithms fit. NEE estimates were evaluated against the control and time smoothing algorithms. The component fluxes were solely evaluated against observations as the control algorithm did not provide component flux estimates. The suite of tests run on various hypotheses are outlined in table 2.6. Full elaboration of these methods are explained in this section.

TABLE 2.6. The methods that will be employed to statistically verify the hypotheses outlined in section 1.2

	Annual Average	RMSE Test	Paired T-test	Cross Cor/Autocor	Ljung-Box Test	Mean Φ Spectrum
$\overline{NEE}_{TF} \leq \overline{NEE}_{Control}$	✓	✓	✓	-	-	-
$\overline{GPP}_{TF} = \overline{GPP}_{Obs}$	✓	✓	✓	-	-	✓
$\overline{RESP}_{TF} = \overline{RESP}_{Obs}$	✓	✓	✓	-	-	✓
$NEE_{TF,seasonal} = NEE_{Control,seasonal}$	-	-	-	✓	✓	✓
$GPP_{TF,seasonal} = GPP_{Obs,seasonal}$	-	-	-	✓	✓	✓
$RESP_{TF,seasonal} = RESP_{Obs,seasonal}$	-	-	-	✓	✓	✓
Observational Uncertainty Tests	✓	-	-	-	-	-

2.6.1. ANNUAL AVERAGES

This study employed equations (2.38) and (2.39) from the update step of the optimization as a both visual and qualitative evaluation the annual average, interannual pattern, and associated uncertainty in a particular year.

$$\overline{NEE}_{posterior} = \vec{k}_m \mathbf{G} \vec{m}_{est} \tag{2.38}$$

$$\sigma^2_{\overline{NEE}_{posterior}} = \vec{k}_m \mathbf{G}^T \mathbf{C}_{\beta,est} \mathbf{G} \vec{k}_m^T \tag{2.39}$$

Where k_m an averaging vector as seen in equation (2.40). These are applied to the observational, time smoothing and control algorithms, if applicable.

$$\vec{k}_m = \Re^{1\times N} = \begin{pmatrix} \frac{1}{365} & \frac{1}{365} & \cdots & \frac{1}{365} \end{pmatrix} \tag{2.40}$$

2.6.2. FRACTIONAL ROOT MEAN SQUARE ERROR REDUCTION

Another visual, but more quantitative test to suggest whether the mean and variance of the error has been lowered was a fractional root mean square error (RMSE) reduction test. This test is similar to the one used in (**?**) and follows equation (2.41)

$$\text{Fractional Reduction of RMSE} = 1 - \frac{RMSE_{posterior}}{RMSE_{prior}} \tag{2.41}$$

Where the RMSE is determined on an annual basis between the observations and the estimates of the pre-assimilation flux and an algorithm's flux estimate. The basic conclusions can be seen in equation (2.42).

$$\text{Conclusion} = \begin{cases} RMSE_{posterior} < RMSE_{prior}, & \text{if } 0 < \text{Fractional Reduction of RMSE} \leq 1 \\ RMSE_{posterior} = RMSE_{prior}, & \text{if Fractional Reduction of RMSE} = 0 \\ RMSE_{posterior} > RMSE_{prior}, & \text{if Fractional Reduction of RMSE} < 0 \end{cases} \tag{2.42}$$

This can be used as a suggestion that the estimated fluxes are better than that of the pre-assimilation flux, control or other algorithm variant. However, this method does not give statistical certainty validation and was for qualitative use.

2.6.3. Error Autocorrelation and Cross Correlation

A more rigorous statistical test of the interannual mean and seasonal cycles was evaluated according to the reduction of the error between the observed flux and a corresponding optimized fit. Seen in equations (2.43) and (2.44) are examples of the difference in *a posteriori* estimates of NEE from the control or time smoothing algorithms and the observations.

$$\Delta NEE_{Obs-TF}(t) = NEE_{Obs}(t) - NEE_{TF,est}(t) \tag{2.43}$$

$$\Delta NEE_{Obs-Control}(t) = NEE_{Obs}(t) - NEE_{Control,est}(t) \tag{2.44}$$

The first evaluation was to see if these two error timeseries are correlated or independent and identically distributed (IID). This was evaluated by the cross correlation across a number of lags (τ). An example of the cross correlation function when $\Delta NEE_{Obs-Control}$ lags ΔNEE_{Obs-TF} is

seen in equation (2.45).

$$r_{\Delta NEE_{Obs-Control},\Delta NEE_{Obs-TF}}(\tau) = \frac{\sum_{i=1+\tau}^{N}\left[(\Delta NEE_{Obs-Control}(i)'\Delta NEE_{Obs-TF}(i-\tau)')\right]}{\sigma_{\Delta NEE_{Obs-Control}}\sigma_{\Delta NEE_{Obs-TF}}} \tag{2.45}$$

$$\Delta NEE_{Obs-Control}(i)' = \Delta NEE_{Obs-Control}(i) - \overline{\Delta NEE}_{Obs-Control}(i) \tag{2.46}$$

$$\Delta NEE_{Obs-TF}(i-\tau)' = \Delta NEE_{Obs-TF}(i-\tau) - \overline{\Delta NEE}_{Obs-TF}(i) \tag{2.47}$$

An example of the null hypothesis and alternative hypotheses for the cross correlation function in (2.45) are seen in equations (2.48) and (2.49).

$$H_o : r_{\Delta NEE_{Obs-Control},\Delta NEE_{Obs-TF}}(\tau) = 0 \tag{2.48}$$

$$H_a : r_{\Delta NEE_{Obs-Control},\Delta NEE_{Obs-TF}}(\tau) \neq 0 \tag{2.49}$$

If the two timeseries are correlated in some way, the correlation coefficient of a particular lag will exceed a critical certainty bounds defined by a critical t-statistic at the 95th percentile adjusted by the Bonferroni correction as defined in equation (2.50).

$$C_{bound} = \pm\frac{t_{crit,\frac{\alpha}{2*N}}}{\sqrt{N}} \tag{2.50}$$

$$\alpha = 0.05$$

In equation (2.51), the autocorrelation function of the error timeseries was used to detect white noise as the remaining signal of the error timeseries.

$$r_{\Delta NEE,\Delta NEE}(\tau) = \frac{\sum_{i=1+\tau}^{N}\left[(\Delta NEE(i)'\Delta NEE(i-\tau)')\right]}{\sigma^2_{\Delta NEE}} \tag{2.51}$$

Example residuals, $\Delta NEE(i)'$ and $\Delta NEE(i-\tau)'$, are defined in equations (2.46) and (2.47).

If the autocorrelation function is 0 across all lags, then it can be assumed the error timeseries is white noise. Therefore, the autocorrelation functions of the error timeseries were evaluated by the example hypothesis tests in equations (2.52) and (2.53).

$$H_o : r_{\Delta NEE,\Delta NEE}(\tau) = 0 \tag{2.52}$$

$$H_a : r_{\Delta NEE,\Delta NEE}(\tau) \neq 0 \tag{2.53}$$

These hypotheses were evaluated against the same certainty bounds in equation (2.50).

2.6.4. Paired T-Test

The direct evaluation of the annual averages was from the paired T-test. In the event that the cross-correlation suggested that the error timeseries of NEE may be correlated slightly above the confidence bound there should not an issue of normality in the tested distribution as the length of the data series always is much greater than 30. The an example of the paired T-test for NEE is shown in equation (2.54).

$$t_{score} = \frac{\overline{\Delta NEE_{Obs-TF}(t) - \Delta NEE_{Obs-Control}(t)}}{\sqrt{\frac{\sigma^2_{TF-Control}}{N_{TF-Control}}}} \tag{2.54}$$

$$|t_{score}| > |t_{crit,1-\alpha,N_{TF-Control}-1}|$$

$$p_{value} < \alpha$$

$$\alpha = 0.05$$

Example null and alternative hypotheses being tested for NEE in this step are shown in equations (2.55) and (2.56).

$$H_o : \overline{\Delta NEE_{Obs-TF}} \geq \overline{\Delta NEE_{Obs-Control}} \tag{2.55}$$

$$H_a : \overline{\Delta NEE_{Obs-TF}} < \overline{\Delta NEE_{Obs-Control}} \tag{2.56}$$

The T-test and hypotheses being tested for GPP and RESP in this step are shown in equations (2.57) through (2.59).

$$H_o : \overline{(GPP/RESP)_{TF}} = \overline{(GPP/RESP)_{Control}} \tag{2.57}$$

$$H_a : \overline{(GPP/RESP)_{TF}} \neq \overline{(GPP/RESP)_{Control}} \tag{2.58}$$

$$t_{score} = \frac{\overline{(GPP/RESP)_{TF}(t) - (GPP/RESP)_{Obs}(t)}}{\sqrt{\frac{\sigma^2_{TF-Obs}}{N_{TF-Obs}}}} \tag{2.59}$$

$$|t_{score}| > |t_{crit,1-\frac{\alpha}{2},N_{TF-Control}-1}|$$

$$p_{value} < \frac{\alpha}{2}$$

$$\alpha = 0.05$$

If the paired T test used in this study is able to reject the null hypothesis, then it can be assumed that the mean error between the time smoothing algorithm and the observations is equal to or lower than the mean error between the control algorithm and observations.

2.6.5. Ljung-Box Test

If the autocorrelation function of an error timeseries was found to be within the bounds to suggest some presence of only white noise, then to fully quantify these findings a Ljung-Box test

was used to confirm or deny only white noise remains in the error timeseries. The Ljung-Box test of the autocorrelation function is seen in equation (2.60).

$$Q = N(N+2)\sum_{\tau=1}^{H}\frac{r_\tau}{N-\tau} \tag{2.60}$$

$$Q > \chi^2_{1-\alpha,H}$$

$$p_{value} < \alpha$$

$$\alpha = 0.05$$

Where H is the number of lags, Q is the Q-score, and $\chi^2_{1-\alpha,h}$ is the χ^2 value at the α-quantile of H number of lags. The hypothesis test being evaluated of the Ljung-Box test at the 95th quantile is seen in equations (2.61) and (2.62).

$$H_o \text{ :The data are independent as a result of white noise} \tag{2.61}$$

$$H_a \text{ :The data are not independent and display some sort of correlation} \tag{2.62}$$

If the null hypotheses of this experiment was retained then it can be assumed that both the annual mean and seasonal cycle of the given error timeseries are well-fitted. This infers that a particular time smoothing algorithm variant or the control are able to resolve the annual and seasonal cycles of the flux in question.

2.6.6. Mean Power Spectrum

If both the autocorrelation and Ljung-box tests suggest there was the presence of some correlation in the error timeseries, then the conclusions of a well fitted seasonal cycle may not be dismissed as other unresolved errors could be to blame. A mean power spectrum was used to

identify which part of the error timeseries signal were being unresolvede. The number of spectral estimates that formulate this mean power spectrum is seen in equation (2.63).

$$M_{ch} = 2N_{years} - 1 \tag{2.63}$$

Where N_{years} is the number of year in the timeseries and M_{ch} is the number of spectral estimates. Furthermore, a particular spectral estimate will estimated from a Kaiser window filter applied to the timeseries over a window length of 365 days. The usage of a Kaiser window is preferred since it can mimic the spectral qualities many other windows filters given the a particular shape parameter, γ. The Kaiser window used is seen in equation (2.64).

$$w(t) = \begin{cases} 0 & -\frac{N_{days}-1}{2} > t \\ I_0 \frac{\left(\gamma\sqrt{1-\frac{4t^2}{(N_{days}-1)^2}}\right)}{I_0(\gamma)} & -\frac{N_{days}-1}{2} \leq t \leq \frac{N_{days}-1}{2} \\ 0 & t > \frac{N_{days}-1}{2} \end{cases} \tag{2.64}$$

$$\gamma = 14$$

$$N_{days} = 365$$

Where I_0 is the zeroth order Modified Bessel Function. Since the window tapers off giving only maximum representation to a minimal number of actual points in the power spectrum, every spectral estimate will begin at every half year. This means the final year of a timeseries will only have half of its data fully represented. This should not cause any misinterpretation given a substantial number of spectral estimates in a timeseries.

The power spectrum of each spectral estimate is then computed and averaged together to make the mean power spectrum using equation (2.65).

$$\overline{\phi}(\omega) = \frac{\sum_{i=1}^{M_{ch}} \phi_i(\omega)}{M_{ch}} \tag{2.65}$$

Where ω is a particular frequency and i is the ith spectral estimate. The mean power spectrum is then evaluated against the corresponding red noise spectrum and critical red noise spectrum in given in equations (2.66) and (2.67)

$$\phi_{red}(\omega) = \frac{2T}{1 + T^2\omega^2} \tag{2.66}$$

$$\phi_{red,crit}(\omega) = F_{crit,\alpha,2*N_{years},N_{days}}\phi_{red} \tag{2.67}$$

$$T = -\frac{1}{ln(r_{\tau=1})}$$

$$\alpha = 0.05$$

Where T is the e-folding timescale of the red noise spectrum based on the lag-1 autocorrelation of the error timeseries. If the particular power of wavenumber, k, is greater than the critical red noise timeseries, then this harmonic signal is not red noise, but indicative of an important signal missed in the fit. The seasonal signal will be evaluated from the hypotheses in equations (2.68) and (2.69).

$$H_o : \overline{\phi}(\omega)_{k=1} \geq \phi(\omega)_{red,crit,k=1} \tag{2.68}$$

$$H_a : \overline{\phi}(\omega)_{k=1} < \phi(\omega)_{red,crit,k=1} \tag{2.69}$$

If the first wavenumber is less than the critical red noise spectrum, then the assumption can be made that there was modest fit of the seasonal cycle from either a variant of the time smoothing algorithm or the control algorithm.

CHAPTER 3

RESULTS

3.1. HOW MANY HARMONICS ARE NECESSARY

Shown in figure 3.1 is the percent variance explained by wavenumbers from the averaged yearly power spectrum of the normalized flux errors between at three different ecosystems and climate regimes. The three ecosystems have at least 60% of their error variance explained by the first 3 to 6 wavenumbers in any gross flux and decreases to 0 to 2% for the remaining wavenumbers. This suggests that the errors between the model and observations are the most persistant for the slowest of timescales.

It is worth mentioning that there should be a discrepancy between the realistic number of harmonics needed to optimize for just NEE alone and the number of harmonics needed to optimize for NEE when using the component fluxes. This is because when optimizing using two contrasting component fluxes that vary differently than the net flux, the result in this case is a quicker variation in the net flux. As a general rule for this methodology use the number of significant harmonics present. If we are optimizing NEE using RESP and GPP, then the highest number of significant harmonics between GPP and RESP should be used. An example of this would be in the deciduous broadleaf forest where only need 3 harmonics to optimize for NEE alone, but 6 harmonics to optimize NEE using GPP and RESP. As a result, figure 3.1 shows that the choice of 3 to 6 harmonics are justified for the optimization process.

3.2. EXPERIMENT 1

The purpose of the first experiment was to evaulate the time-smoothing algorithm against the control algorithm using only observed the NEE flux to optimize for the modeled NEE flux. As

stated in the methods, the algorithm optimizes for 12 bias coefficients and uses a portion of both the posterior and prior model covariance estimates rather than the 52 independent weekly bias coefficients. Table 3.1 shows the results of all statistical significance tests done to the optimizations of the first experiment and whether or not the statistical hypothesis tests were met.

3.2.1. Experiment 1: The NEE Estimation and RMSE reduction

The first experiment only produced estimates of the NEE model bias from assimilated NEE observations. Figure 3.2 shows the daily estimations of NEE from both the control and the time smoothing algorithm. These algorithms both show good estimation of both the seasonal and annual cycles of NEE for both Harvard Forest and Vaira Ranch across all years. Closer examination of the visual fits show the control algorithm appears to be better at estimating the faster time variations and the time smoothing algorithm is better at obtaining the slower time variations of the observations. This same result was seen across all 8 sites. The goodness of these estimations is incapable of being diagnosed just from this visual comparison and so more rigorous testing is needed.

The first test was the reduction of the RMSE between the prior and posterior estimates of NEE. The top panel of figure 3.3 shows the annual RMSE reduction between the control and the time smoothing algorithms across all 8 sites. Visually, this test demonstrates that in most circumstances the reduction of RMSE of NEE for the time smoothing algorithm is as good or worse than the control. An example of control outperformance is seen at Harvard Forest. This site only experienced a reduction between .19 and .2 for the time smoothing algorithm, while the control demonstrated a reduction between .22 and .32. These results suggest that either the annual means or variance may be underestimated by the time smoothing algorithm.

3.2.2. Experiment 1: Annual Sources and Sinks

Examination of the annual mean estimation will give way to supporting the results of the RMSE reductions and the overarching hypotheses. Example annual CO_2 sources and sinks under increasing amounts of observational uncertainty from the first experiment are seen in figure 3.5 for Harvard Forest and Vaira Ranch. In the top left panel of these figures, the standard optimization using no variations in observational uncertainty are observed. Under the prescribed conditions, both algorithms estimate basically the same annual average and interannual variations at both sites. This was observed at the other 6 sites as well. Thus, a definitive result about the performance of the time smoothing algorithm compared the control difficult to deduce from the annual means alone.

Quantitative evidence of both the cross correlation function and paired T test of the error means show that the error timeseries of both algorithms are statistically different but nearly indistinguishable from one another. Beginning with the cross correlation, figure 3.7 shows the cross correlation functions for the error timeseries at Harvard Forest and Vaira Ranch. The cross correlation functions at both sites suggested that when either error timeseries lags the other, there some periodicity and correlation between the two timeseries that exceeds the 95th percentile certainty bounds. The maximum exceedence of the confidence interval is at lag-0, but the general exceedence is on the order of .05 which is within the relative certainty of the significance bounds given the sample size N. This is true across all sites. This result indicates the two optimizations cannot be seen as IID from one another in this test. Since violation of the certainty bounds is small and the sample size much larger in comparison to the statistical test requirements of the paired T-test can still be used. The paired T-test resulted demonstrated that the interannual source or sink estimate from the time smoothing algorithm was as equal to or greater than the control algorithm for 6 of the 8 sites estimated to within the 95th percentile. Campbell River and Vaira Ranch both resulted in statistically

significant better annual estimates than the control algorithm. Consequently, these two statistical tests verify the qualtitative results of the annual NEE averages and RMSE reductions.

3.2.3. Experiment 1: Increasing Observational Uncertainty

When exposed to increasing amounts of observational uncertainty, the time smoothing algorithm was more resilient to observational uncertainty changes than the control. The other three panels of figures 3.5 and 3.6 show the effects of 2, 5, and 10 times observational uncertainty estimates for Harvard Forest and Vaira Ranch, respectively. The both algorithms first reverted toward the prior estimate of NEE before moving toward the original estimations of SiB4 flux. At all sites, it was evident that the control algorithm regressed toward the prior much sooner than the time smoothing algorithm. The effect of this increase was moderated by how much original certainty the observations had. Therefore, a well-observed flux was good for both algorithms, but only the time smoothing algorithm was more robust over more poorly-observed sites.

3.2.4. Experiment 1: Seasonality

When seasonality was examined, the time smoothing and control algorithms showed that neither algorithm was particularly skilled at estimating the seasonal cycle. Figure 3.7 shows the autocovariance functions of the NEE error timeseries for both algorithms. The autocorrelation functions for Harvard Forest indicates that on a yearly basis, both algorithms are correlated with themselves outside of the 95th percentile certainty bounds. The location of this error was representative of a fall or spring mismatch where NEE crosses zero. This pattern was observed at all sites except for ARM-SGP and Vaira Ranch. The general correlation exceedence of the confidence bounds at these sites was about .06 and .11 for the control and time smoothing algorithms. The autocorrelation function at Vaira Ranch indicated the presence of white noise. When this result

was tested on the Ljung-Box test, Vaira Ranch was shown to still have some correlation remaining in the error at the 99th confidence level. In general, the magnitude and timing of error varied from site-to-site, but these results suggest there was still some residual of seasonality to be estimated.

The mean power spectra for the first 20 harmonics for both Harvard Forest and Vaira Ranch are seen in figure 3.8. These two sites show that there was still statistically significant power within at least the first 5 harmonics for both algorithms. The zeroth and seasonal harmonic (k=0,1) suggested that neither the general mean or seasonal cycle is fully resolved in either timeseries. These power spectra results are not generalized to all sites. The other 6 sites were actually able to fully resolve both the mean and seasonality of the NEE signal to within red noise spectrum of 95th percentile, but not the normal red noise spectrum.

3.3. Experiment 2

The purpose of the second experiment was to evaulate the time-smoothing algorithm against the control algorithm using only observed the NEE flux to optimize for the modeled GPP and RESP fluxes. As stated in the methods, this version of the algorithm optimizes for 24 bias coefficients and uses a portion of both the posterior and prior model covariance estimates rather than the 52 independent weekly bias coefficients. Table 3.2 shows the results of all statistical significance tests done to the optimizations of the second experiment and whether or not the statistical hypothesis tests were met.

3.3.1. Experiment 2: The Flux Estimation and RMSE reduction

The flux recovery from the second experiment indicated that while NEE is better estimated it is at the cost of the GPP and RESP signals. Example component flux estimates for Harvard Forest and Vaira Ranch from the second experiment are shown in figure 3.9. As can be seen at both sites,

the second experiment is capable of recovering excellent estimates for any year of the NEE signal. The RESP and GPP estimates are do not resemble the observations and are physically unrealistic. These results were seen across all sites. These visual results are supported by the fractional RMSE reduction.

In the middle panel of figure 3.3, the RMSE reduction of NEE shows that the second experiment is skilled at making a better prediction than that of the prior estimate and control. For example, the RMSE reduction of NEE at Harvard Forest for experiment 2 is on the order of .25 to .45, which is nearly a .2 better than the control algorithm. All sites showed improvement and better performance in the fractional RMSE reduction of NEE, however this came at the cost an increase in RMSE for the component fluxes. In figure 3.4, the fractional RMSE reduction for the component fluxes are seen for the second and third experiments. Across 7 sites for both GPP and RESP, the second experiment resulted in negative RMSE reductions upwards of -.1 to -3. This suggests that both component fluxes lost estimation skill upwards of 400% in some circumstances. Vaira Ranch was the only site to have both positive fractional RMSE reductions for both GPP and RESP. As a result of these two tests, the other statistical tests were used show the cause and benefit of this result.

3.3.2. Experiment 2: Annual Sources and Sinks and Uncertainty Increases

The annual NEE mean estimation gave way to supporting the results of the RMSE of NEE reductions. Like the first experiment, example annual NEE averages from Harvard Forest and Vaira Ranch under increasing amounts of observational uncertainty for the second experiment are seen in figures 3.10 and 3.11. In the top left panel of these figures, the second experiment shows near better estimation of the annual NEE average over the control to within error estimates of observed NEE average. The interannual pattern is well estimated. In the other three panels of both

figures, there is virtually no change to the algorithms performance except with larger uncertainty bounds. This indicates that this version of the time smoothing algorith resulted robust estimation skill with upwards of 100 times more observational uncertainty. These same results were observed at the other 6 sites as well. This qualitative evidence is supported by both the cross correlation functions and paired T-test for the original uncertainty estimation. Quantitative evidence of both the cross correlation function and paired T test of the error means show that the error timeseries of both algorithms are statistically different but more distinguishable from one another than the first experiment. The cross correlation functions of Harvard Forest and Vaira Ranch in figure 3.12 show that the correaltion between the timeseries is lower than the first experiment. As demonstrated at Harvard Forest, 5 of the 8 sites exhibited some periodicity in the correlation on a yearly basis, but the only substantial maximum exceedence of the confidence interval is at lag-0 and in the final year of lags. The general exceedence is on the order of .07 which is within the relative certainty of the significance bounds given the sample size N. Vaira Ranch demonstrated how 3 of the 8 sites produced cross correlation functions that resemble nearly pure noise. These result suggest the error timeseries can be interpreted as IID from one another in this test and violation of the T-tests assumptions was kept to a minimum. The application of to the paired T-test demonstrated that at every site the time smoothing algorithm produced better estimates of the interannual source or sink over the control algorithm to within the 95th confidence level. These two statistical tests verified the results the annual NEE averages and RMSE of NEE reductions.

3.3.3. Experiment 2: Annually Averaged Component Fluxes

The evidence presented by the timeseries plots of GPP and RESP indicated that there would be little information about the plots of the annual average of GPP and RESP for any site however a discription of this error can still be seen by the cross correlation and paired T test between the

observations and the component fluxes. In figures 3.13 and 3.14 show the cross correlation functions between the observations and the component fluxes. At both sites, it is visually evident that there is a sinusoidal pattern that follows an biannual statistically significant pattern of correlation and anticorrelation. There are superimposed 5 harmonics within these cross correlation functions that are representative of the 5 harmonics used for the time smoothing algorithm. The general exceedence of the certainty bounds is on the average order of .2 for RESP and .3 for GPP. This result suggests the component fluxes at Harvard Forest sites are not IID from the observations, but this result does not necessarily hold true for all sites. Campbell River, Lethbridge, UMBS, and ARM-SGP all showed similar behaviors with respect to the harmonic structure, but indicated noise from the cross correlation functions. These 4 sites were assumed to be IID and evaluated in the paired T-test. When applied to the paired T-test, only 1 of the 4 IID sites showed the annual average of GPP for the time smoothing algorithm is equal to annual average of the observations within the 95th confidence level. Additionally, the paired T-test demonstrated that all four IID sites have annual average of RESP estimations that are equal to the annual average of the observations within the 95th confidence level.

3.3.4. Experiment 2: NEE Seasonality

When seasonality was examined, the second experiment was exceptional in obtaining the NEE seasonality while not particuarly skilled in obtaining the component flux seasonality. In figure 3.12 for both example sites visually show that the error autocorrelation functions of the time smoothing algorithm is basically noise. There is only minor periodicity that is substantially suppressed from the first experiment and with the exception of the first couple lags, autocovariance functions do not surpass the 95th percentile certainty bounds. This was true across all 6 other sites. When the autocorrelation functions were applied to the Ljung-Box Test, it was found that none of the 8 sites

only had white noise composing the error. The mean power spectra of NEE error analysis in figure 3.8 showed that for both example sites error timeseries of the second experiment does not have significant power above the red noise spectrum at the 95th certainty level for either the mean or the seasonal harmonics. In general, these results suggested the error between the observations and time smoothing algorithm at the mean and seasonal cycles are red noise at best, but there some residual sub-seasonal signal in the error.

3.3.5. Experiment 2: Component Flux Seasonality

As opposed to the successful results of the NEE seasonality analysis, the second experiment was not skilled in obtaining the component flux seasonality. Both example sites in figures 3.13 and 3.14 show that the autocorrelation functions of the component flux error timeseries are virtually noise except for the first 20 lags. At these lags for both component fluxes, the correlation is on the average about .3 above the 95th percentile certainty bounds. This was seen at 7 of the 8 flux towers with the exception of UMBS. Given the white noise nature of the remaining signal for the component fluxes, the Ljung-Box test revealed that white noise was not present in either error timeseries at any site. The mean power spectra of RESP flux error analysis in figure 3.15 that for both example sites the second experiment does not produce significant power above the red noise spectrum at the 95th confidence level for either the mean or the seasonal harmonics. This was true for all 8 sites. Futhermore, the mean power spectra of GPP flux error analysis in figure 3.15 showed mixed results concernting the annual and seasonal error power. For 7 of the 8 sites, the spectral power produced by GPP error timeseries was between the red noise time series and red noise spectrum at the 95th confidence level for both the mean or the seasonal harmonics. Harvard Forest was the only site that produced significant power at mean and seasonal harmonics, but in the first 10 harmonics, which could be an outlier result. In general, the combination of the

visual, qualitative, and quantitative tests done on the time smoothing timeseries suggested poor and unrealistic estimation of the component fluxes, but these results are not always statistically poor.

3.4. Experiment 3

The purpose of the third experiment was to evaulate the time-smoothing algorithm against the control algorithm using only observed the NEE and GPP fluxes to optimize for the modeled GPP and RESP fluxes. As stated in the methods, this version of the algorithm optimizes for 24 bias coefficients and uses a portion of both the posterior and prior model covariance estimates rather than the 52 independent weekly bias coefficients. Table 3.3 shows the results of all statistical significance tests done to the optimizations of the third experiment and whether or not the statistical hypothesis tests were met.

3.4.1. Experiment 3: The Flux Estimation and RMSE reduction

The flux recovery from the third experiment resulted in all three fluxes being well estimated. Example component flux estimates for Harvard Forest and Vaira Ranch from the third experiment are shown in figure 3.16. From these figures, the third experiment is capable of recovering all estimates for any year of the flux signal at Vaira Ranch and most years at Harvard Forest. Like the second experiment, the NEE signal is well followed, but the noise is smoothed out. Unlike the second experiment, the RESP and GPP estimates now resemble and follow the observations, which is more physically realistic. These results were seen across all sites except for Mead-Irrigated. At this site, the recovery resembled the second experiment. The visual results of these timeseries are supported by the fractional RMSE reduction.

In the bottom panel of figure 3.3, the RMSE reduction of NEE shows that the third experiment as skilled at making a better estimation as that of the second experiment. For example, the RMSE

reduction of NEE at UMBS for experiment 3 is on the order of .3 to .5, which is identical to that of the second experiment and about .2 better than the control. 6 of the 8 towers showed similar results. Old Black Spruce and Harvard Forest showed increased performance when compared the first experiment and control, but decreased performance when compared to the second experiment. In figure 3.4, the fractional RMSE reduction across all 8 sites showed that for both GPP, the third experiment resulted in now produces RMSE reductions upwards of .05 to .7. This was also true for RESP, but Mead-Irrigated was the only site to produce a negative RMSE reduction. This suggests that both component fluxes gained estimation skill upwards of 70% in some years. As a result of these tests, the other statistical tests were able to be used to statistically reinforce these results.

3.4.2. Experiment 3: Annual Sources and Sinks and Uncertainty Increases

Like the second experiment, the annual NEE mean estimation supported the results of the RMSE of NEE reductions. Example annual NEE averages from Harvard Forest and Vaira Ranch under increasing amounts of observational uncertainty for the third experiment are seen in figures 3.17 and 3.18. The annual NEE average estimated by the time smoothing algorithm over Vaira Ranch shows better estimation over the control to within error estimates of observed NEE average. This result was seen in all sites except for Harvard Forest. Harvard Forest resulted in better estimation of the annually averaged NEE than the control, but does not replicate the observational record over most years. The interannual pattern is well estimated to within error estimate at all sites except for Harvard Forest. Under increasing uncertainty, Vaira Ranch and the other 6 sites show virtually no change to the algorithm's performance except with larger uncertainty bounds. Harvard Forest showed increased performance under a doubling of observational uncertainty, similar to the initial estimation of Harvard Forest under the second experiment. This result was constant under the 5 and 10 times simulations for Harvard Forest as well. Qualitatively, this algorithm shows

nearly as good NEE source and sink estimation as the second experiment. This evidence is further supported by both the cross correlation functions and paired T-test. The cross correlation functions and paired T-test of the error means showed that the error timeseries of the third experiment's time smoothing algorithm is both statistically different from the control. In figure 3.19, the cross correlation functions of Harvard Forest and Vaira Ranch showed that the correlation between the two error timeseries was comparable to the results of the second experiment. The estimation at Harvard Forest demonstrated that when the control lags the time smoothing algorith there is evidence of periodicity in the correlation on a yearly basis, but not vice versa. when the time smoothing algorithm lags the control, there is evidence of only minor periodicity and noise to within the 95th percentile certainty bounds. This result was seen at 5 of the 8 sites, with the exceptions being of Vaira Ranch, ARM-SGP, and UMBS. At these 5 sites, the maximum location and mean exceedence of the confidence bound was at lag-0 and .07 across most sites that were not conisdered only noise. The cross correlation function at Vaira Ranch, ARM-SGP, and UMBS resemble noise and can be considered IID.

Since, the general of the exceedence is on the order of .07 which is within the relative certainty of the significance bounds given the sample size N the paired T-test was interpreted to all sites. The paired T-tests demonstrated that at every site the time smoothing algorithm produced better estimates of the interannual source or sink over the control algorithm to within the 95th confidence level. Thus, these two statistical tests of NEE verified the results seen in the annual NEE averages and RMSE of NEE reductions.

3.4.3. Experiment 3: Annually Averaged Component Fluxes

The timeseries plots of GPP and RESP indicated that there is strong evidence that annual average of GPP and RESP for any site may be well estimated. In figures 3.20 and 3.21 show the cross

correlation functions between the observations and the component fluxes. These two sites display nearly identical patterns on both wings of the cross correlation function. Furthermore, it is visually evident that there is a sinusoidal pattern that follows an biannual statistically significant pattern of correlation and anticorrelation similar to that of the second experiment. The general exceedence of the certainty bounds is on the average order of .4 for both RESP and GPP. This is result was seen for all sites. From this, these sites are not IID and are assumed to be indistinguishable from one another. Although the paired T-test cannot be used to statistically verify this experiment for component fluxes, the fact the two timeseries are indistinguishable from one another suggested means are the same as well.

3.4.4. Experiment 3: NEE Seasonality

Like the second experiment, the third experiment was skilled in estimating the NEE seasonality. In figure 3.19 for both example sites visually show that the error autocorrelation functions of the time smoothing algorithm is basically noise. There is only minor periodicity within the first few lags and passed this is effectively a white noise signal. These autocovariance functions do not surpass the 95th percentile certainty bounds with the exception of the first couple of lags. This was true across all other sites. When the autocorrelation functions were applied to the Ljung-Box Test, it was found that none of the 8 sites only had white noise composing the error, much like the second experiment. The mean power spectra of NEE error analysis in figure 3.8 showed that for both example sites error timeseries of the third experiment does not have significant power above the red noise spectrum at the 95th certainty level for any tested harmonics. This was seen for all sites. Harvard Forest, Lethbridge, UMBS, and Mead-Irrigated produced an NEE error mean power spectrum that is above the normal red noise spectrum, but not above the critical certainty level. In general, these results suggested the error between the observations and time smoothing algorithm

at the mean and seasonal cycles are red noise at best, but again there some minor sub-seasonal signal in the error.

3.4.5. Experiment 3: Component Flux Seasonality

Unlike the the second experiment, the third experient was skilled in obtaining the component flux seasonality. Both example sites in figures 3.20 and 3.21 show that the autocorrelation functions of the component flux error timeseries represent the most white noise signals resemblence of any experiment. There are no lags that exceed the 95th percentile certainty bounds beyond the first 10 lags. This was found at all sites as well. The Ljung-Box test discredited the presence of only white noise in any component flux error timeseries. The mean power spectra of RESP flux error analysis suggested that there was no significant power present within any harmonic in the first 20 harmonics. In figure 3.15, both example sites showed the third experiment does not produce significant power above the red noise spectrum at the 95th confidence level for RESP. This was found for the other 6 sites. At all sites, mean power spectra of GPP flux error analysis suggested that there was significant power present within in the first 20 harmonics, especially within the first 5 harmonics. The mean power spectra of GPP flux error analysis in figure 3.15 exceeded the baseline red noise spectrum all sites. Furthermore, the power spectrum for 5 of the 8 sites exceeded the red noise spectrum at the 95th confidence level. In general, these results in conjunction with the indistinguishable timeseries of the component fluxes compared to the observations suggests that these are just the minor differences between the observations and very similar component fluxes.

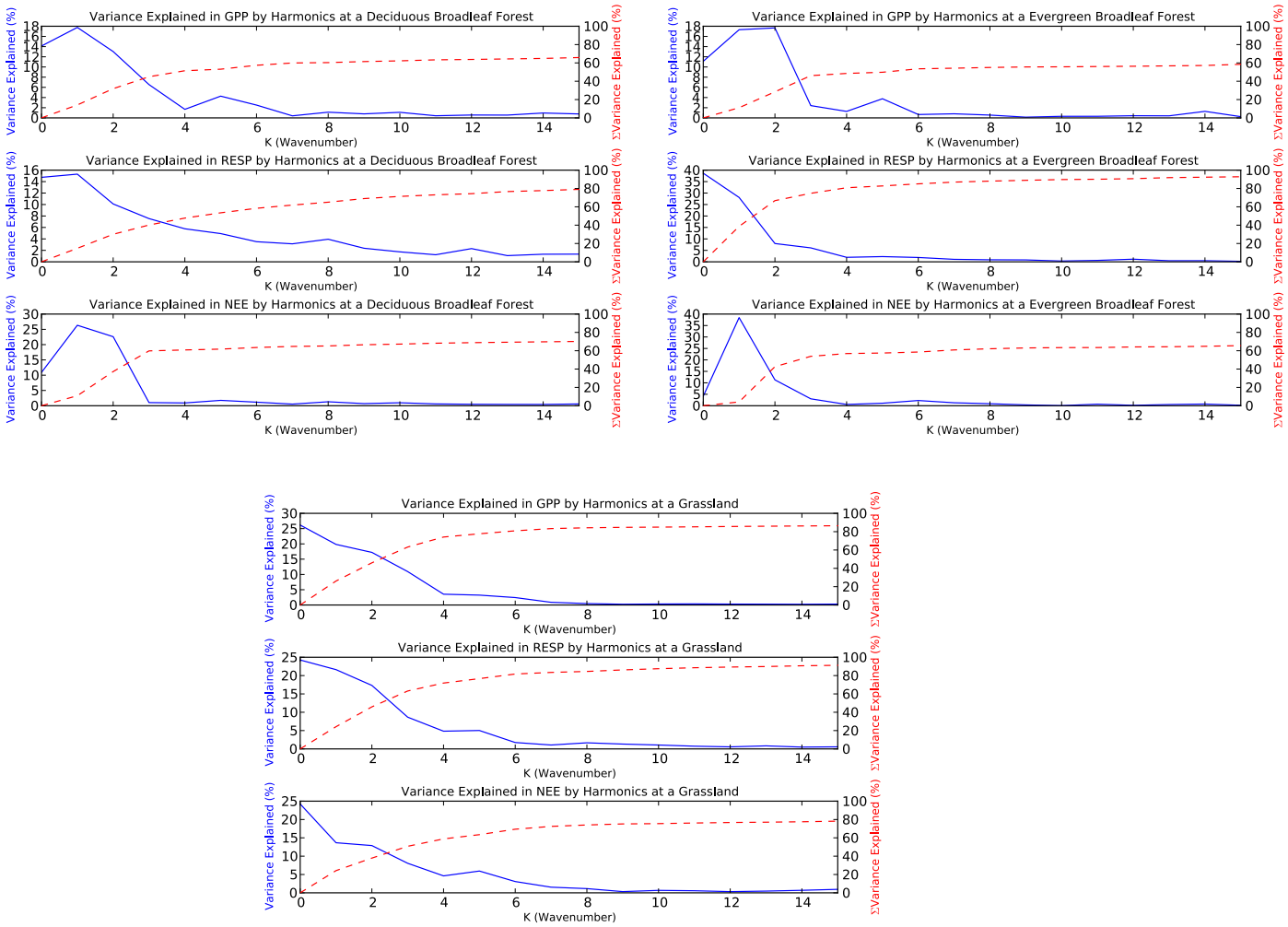

FIG. 3.1. Spectral plots of the percent of variance explained in the errors between the observed flux and the SiB4 flux. The blue curve is the percent of variance explained per wavenumber. The red curve is the partial integral of the blue curve signifying the sum of the variance explained. Upper Left: Harvard Forest, MA. Upper Right: KM67, Tapajos, Brazil. Bottom Center: Lethbridge, Canada

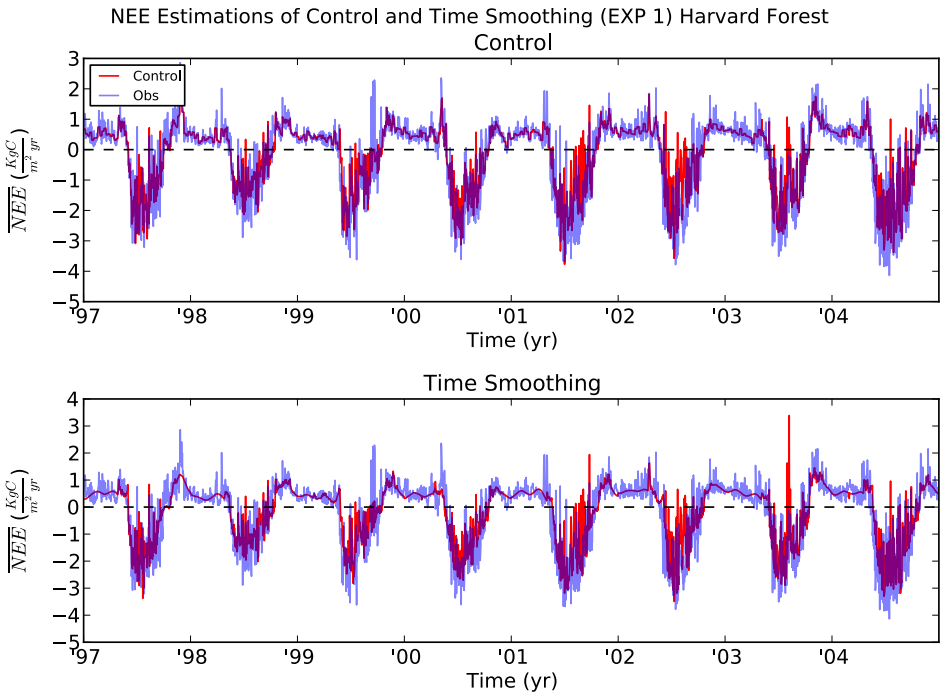

(A) Harvard Forest

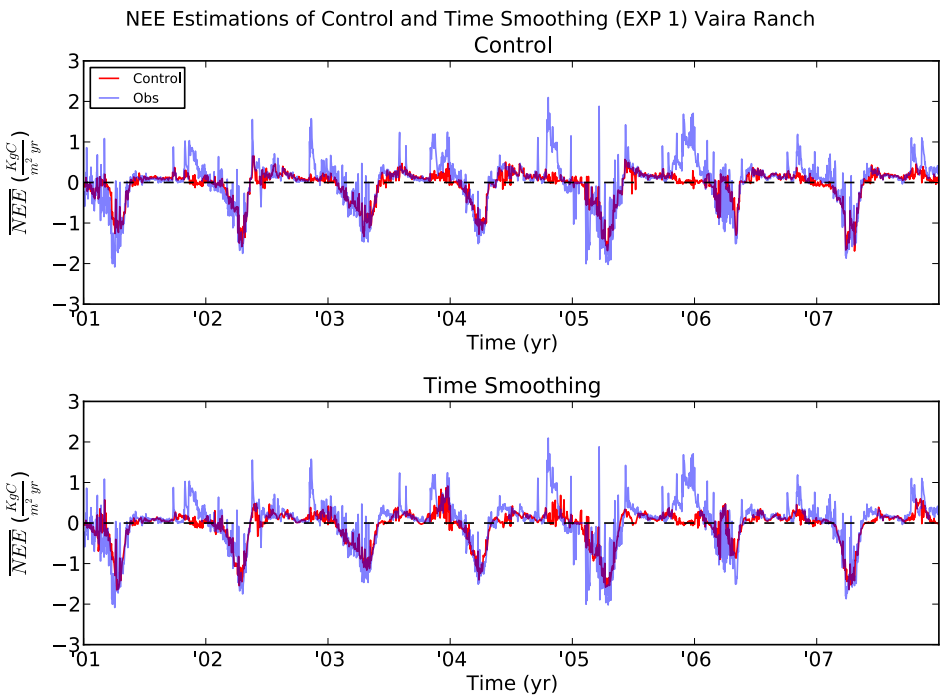

(B) Vaira Ranch

FIG. 3.2. Time evolution of the daily component fluxes at Harvard Forest and Vaira Ranch for the control and time smoothing estimates for Experiment 1. The blue lines are the observations. The red lines are the posterior estimates of a particular algorithm.

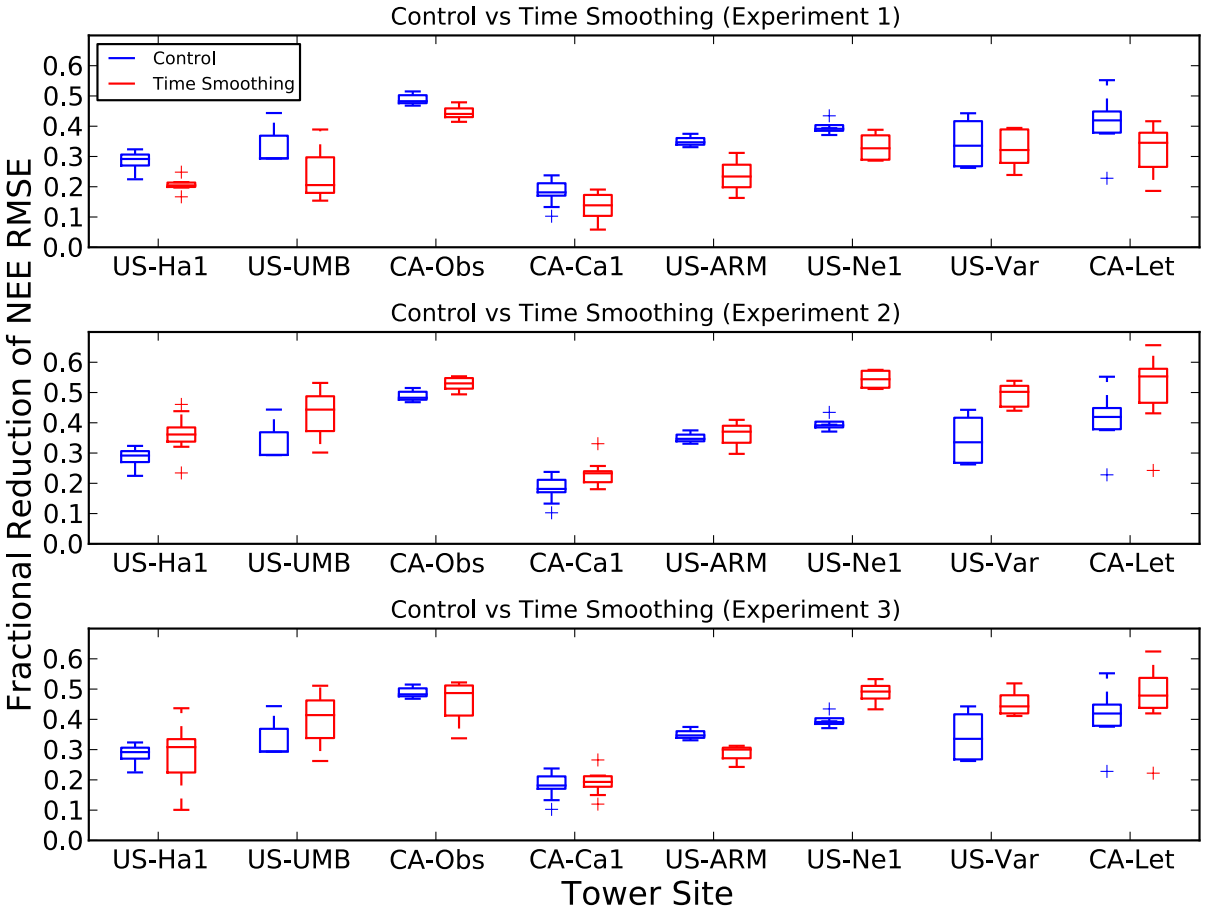

FIG. 3.3. Box-and-whiskers plots of the fractional reduction of RMSE of NEE estimations between the control and the three time smoothing algorithm variants across all sites. Blue and red boxes represent the control and time smoothing algorithm results. ”+” signs represent outliers.

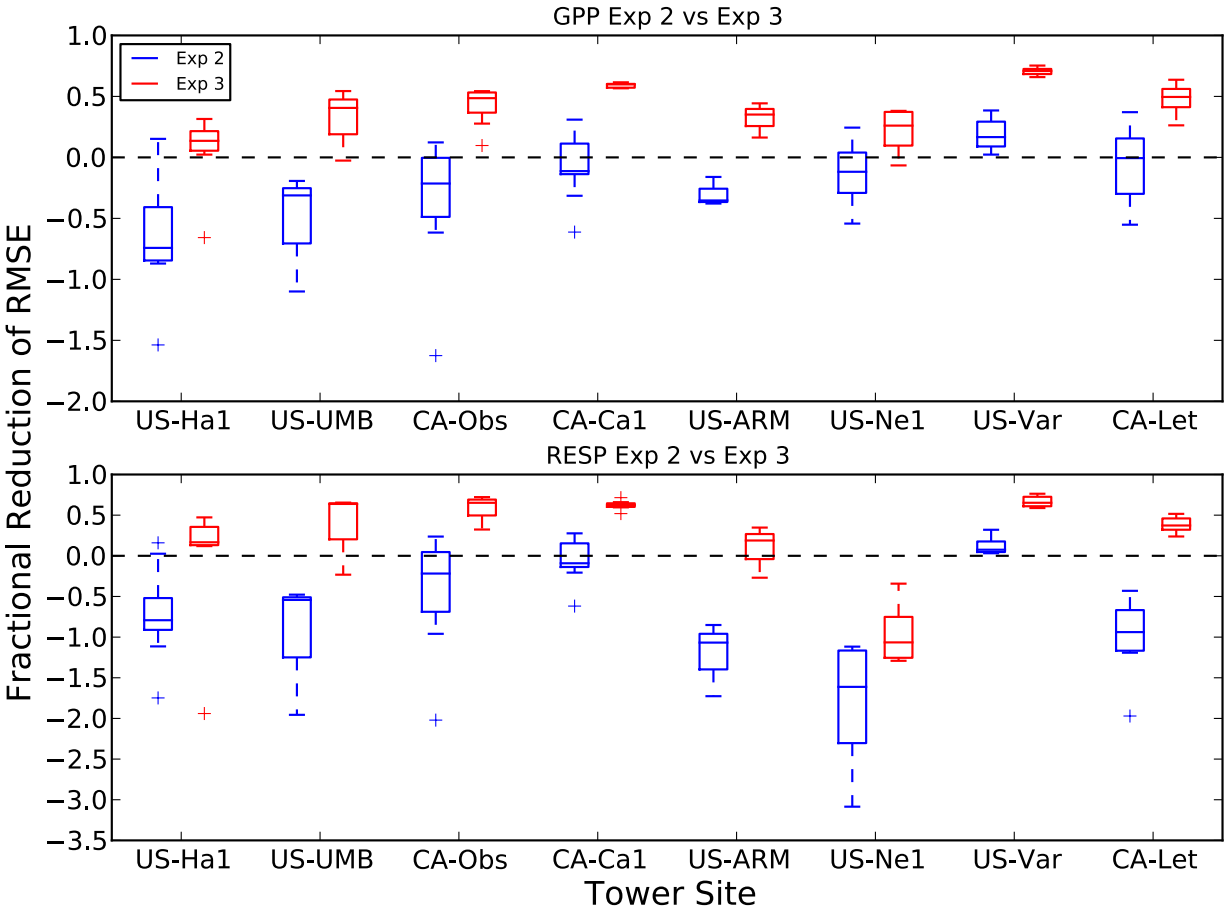

FIG. 3.4. Box-and-whiskers plots of the fractional reduction of RMSE of the component fluxes between the time smoothing algorithm of the 2nd and 3rd experiments. Blue and red boxes represent the 2nd and 3rd experiments fit of the particular component flux. "+" signs represent outliers.

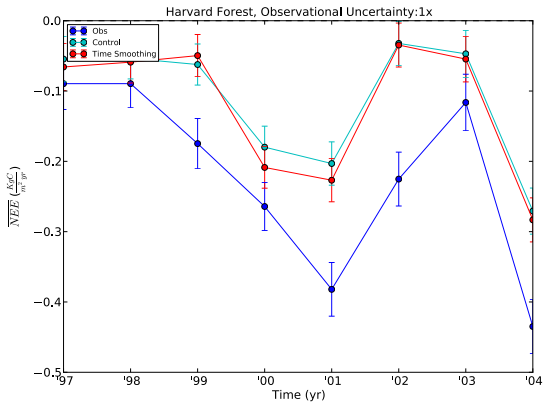

(A) Harvard Forest 1 Times Uncertainty

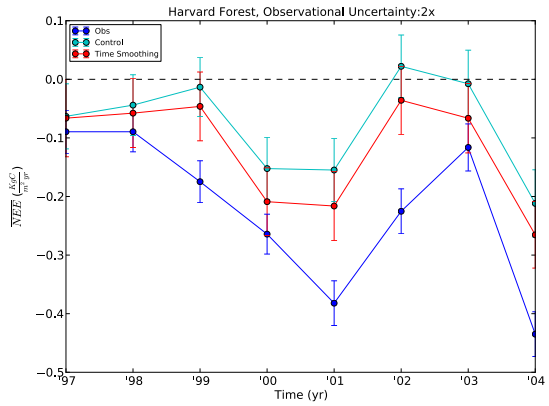

(B) Harvard Forest 2 Times Uncertainty

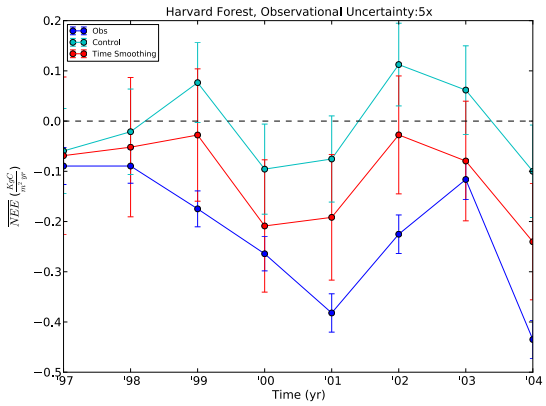

(C) Harvard Forest 5 Times Uncertainty

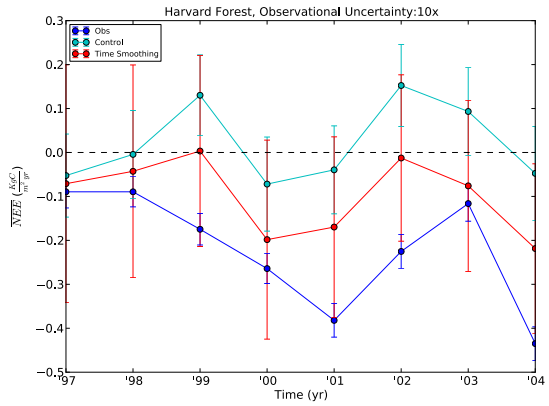

(D) Harvard Forest 10 Times Uncertainty

FIG. 3.5. Time evolution of the annually averaged NEE flux at Harvard Forest under varying amounts of observational uncertainty. Blue and cyan lines are the observations and control simulation. Purple lines are SiB4's simulation pre-assimilation. Green and red lines are the prior and posterior estimates of SiB4 during assimilation. Error bars represent the 1 standard deviation uncertainty in the flux.

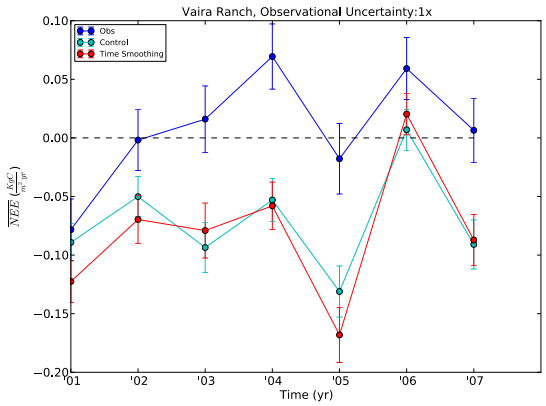

(A) Vaira Ranch 1 Times Uncertainty

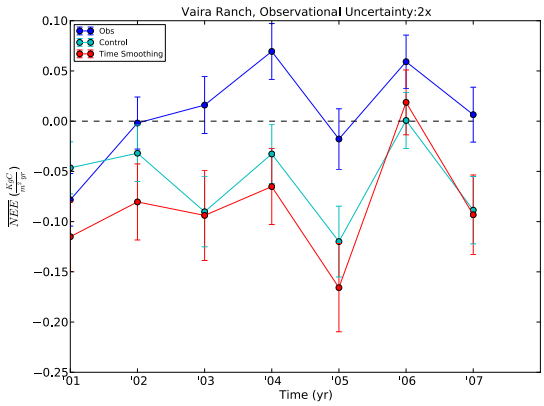

(B) Vaira Ranch 2 Times Uncertainty

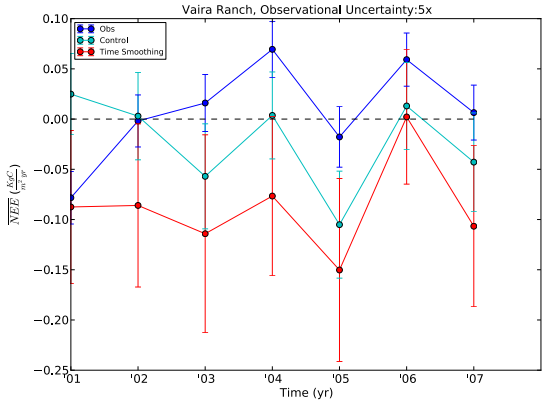

(C) Vaira Ranch 5 Times Uncertainty

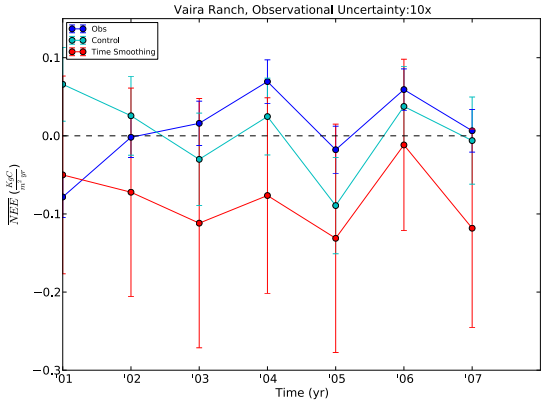

(D) Vaira Ranch 10 Times Uncertainty

FIG. 3.6. Time evolution of the annually averaged NEE flux at Vaira Ranch under varying amounts of observational uncertainty. Blue and cyan lines are the observations and control simulation. Purple lines are SiB4's simulation pre-assimilation. Green and red lines are the prior and posterior estimates of SiB4 during assimilation. Error bars represent the 1 standard deviation uncertainty in the flux.

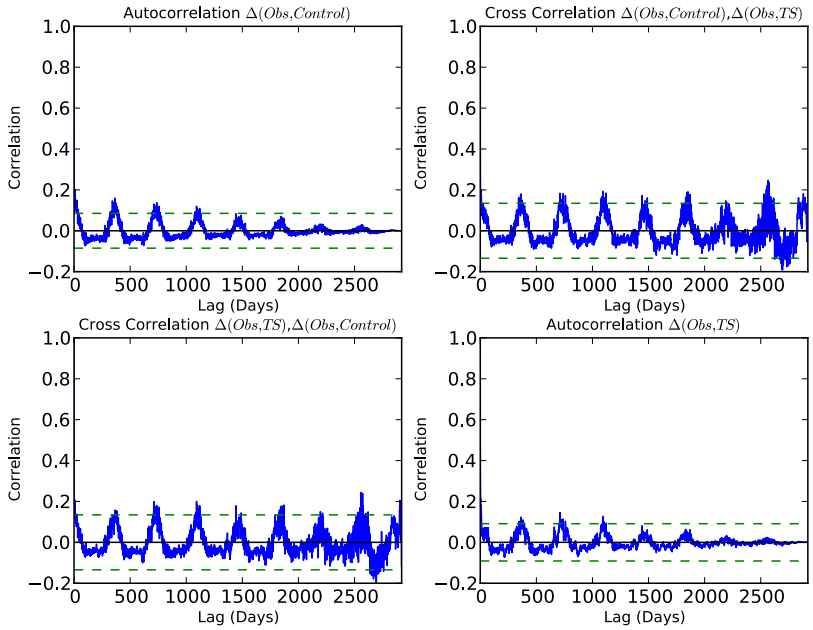

(A) Harvard Forest

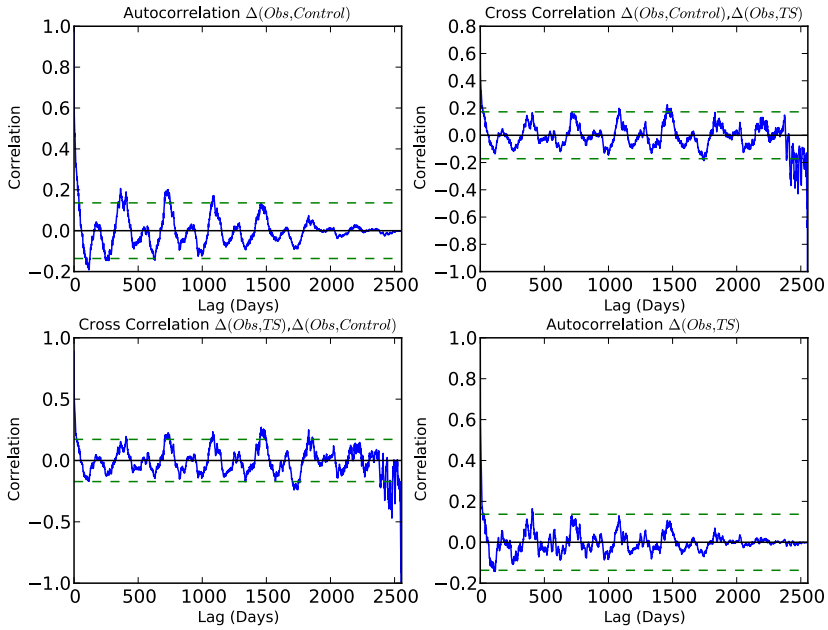

(B) Vaira Ranch

FIG. 3.7. Cross Correlation and Autocorrelation functions between the error timeseries of the control and time smoothing algorithm used in Experiment 1 Harvard Forest and Vaira Ranch. Top Left: Autocorrelation function of error timeseries of the control fit. Top Right: Cross Correlation function of error timeseries where control lags time smoothing. Bottom Left: Cross Correlation function of error timeseries where time smoothing lags control. Bottom Right: Autocorrelation function of error timeseries of the time smoothing fit.

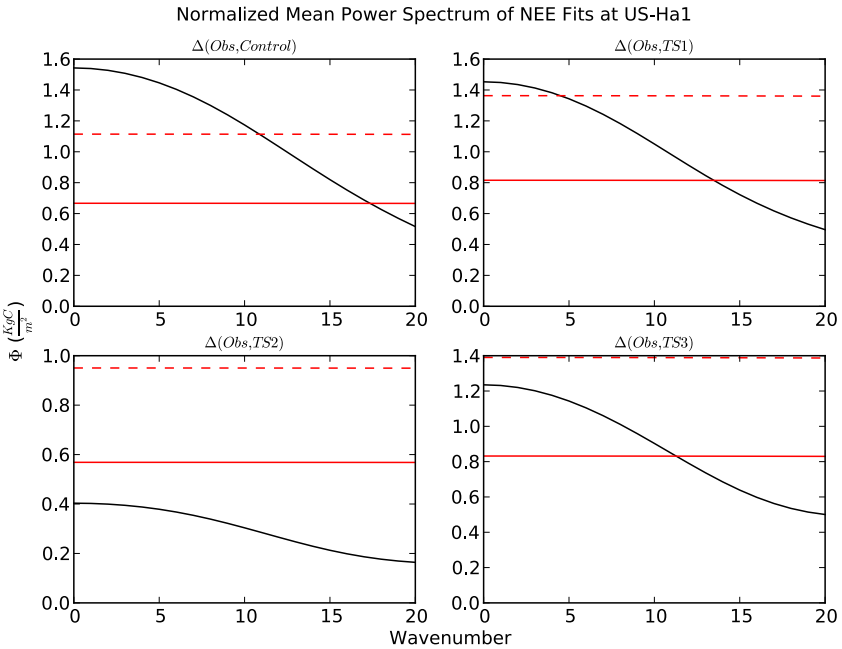

(A) Harvard Forest

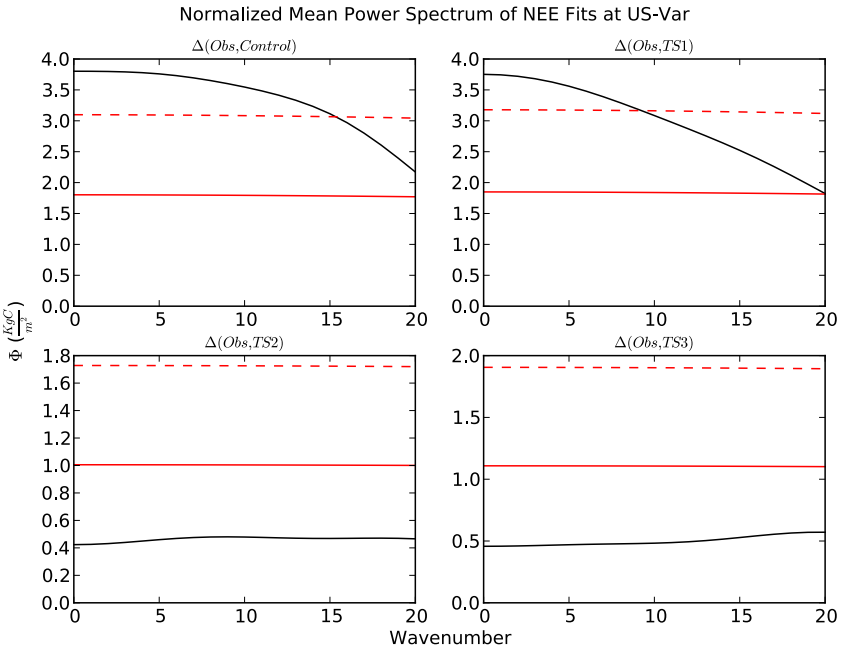

(B) Vaira Ranch

FIG. 3.8. Mean power spectrums for NEE error for all time smoothing variants and control at Harvard Forest and Vaira Ranch. Black lines are power. Red solid is the red noise power spectrum of the datum, and the dashed red line is the red noise spectrum at the 95th percentile. Top Left: Control. Top Right: Time smoothing algorithm for Experiment 1. Bottom Left: Time smoothing algorithm for Experiment 2. Bottom Right: Time smoothing algorithm for Experiment 3

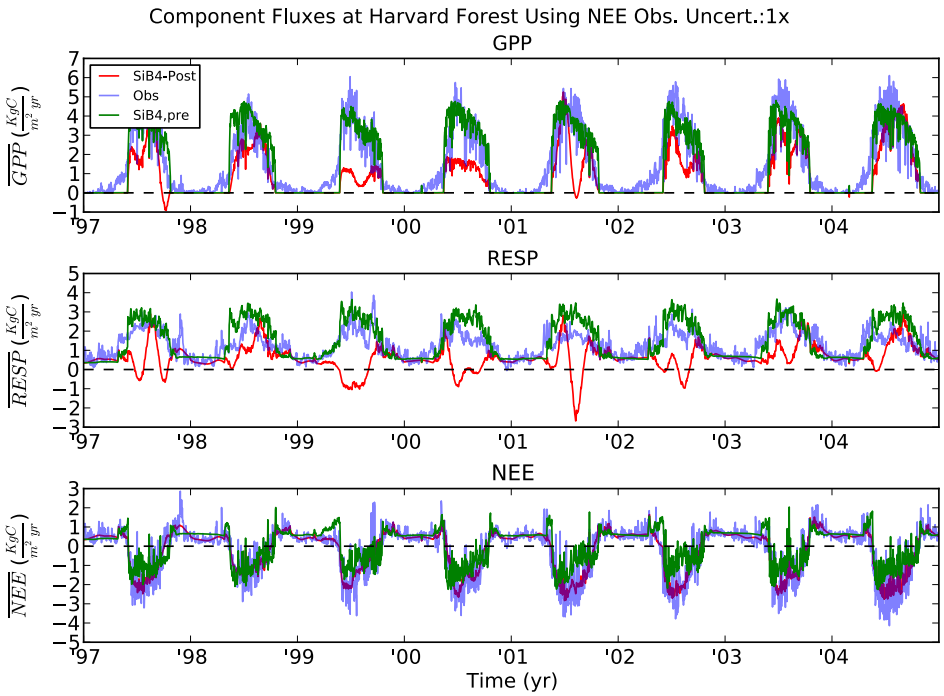

(A) Harvard Forest

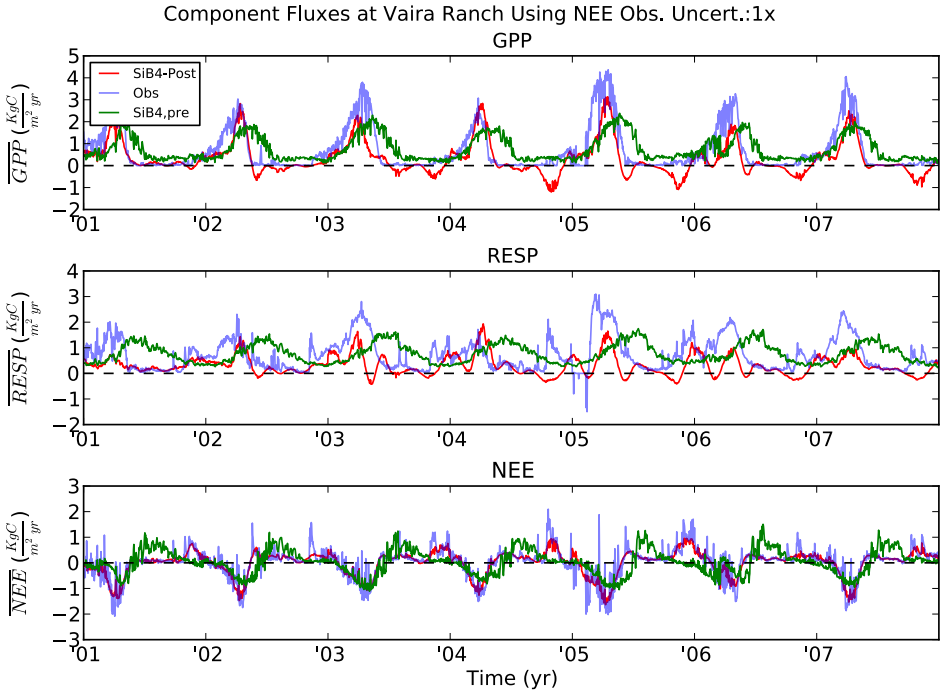

(B) Vaira Ranch

FIG. 3.9. Time evolution of the daily component fluxes of both Harvard Forest and Vaira Ranch as a result of the second experiment. The blue lines are the observations. The red lines are the posterior estimates.

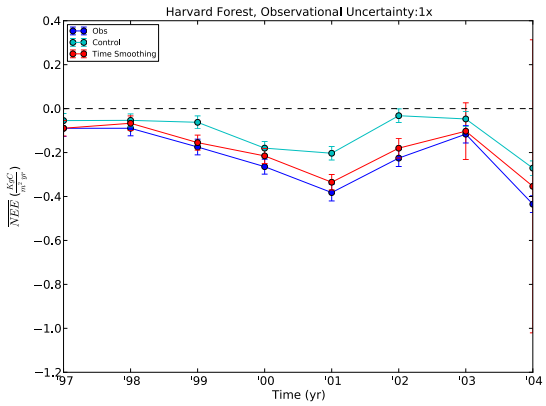

(A) Harvard Forest 1 Times Uncertainty

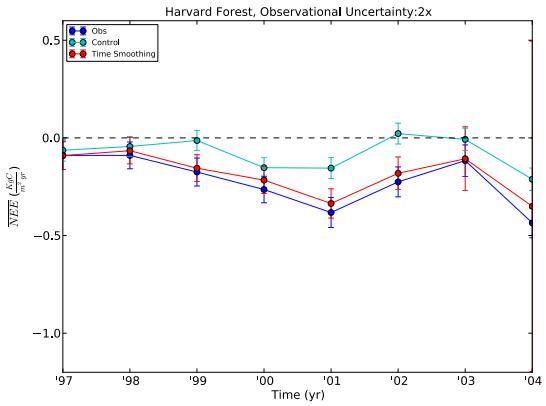

(B) Harvard Forest 2 Times Uncertainty

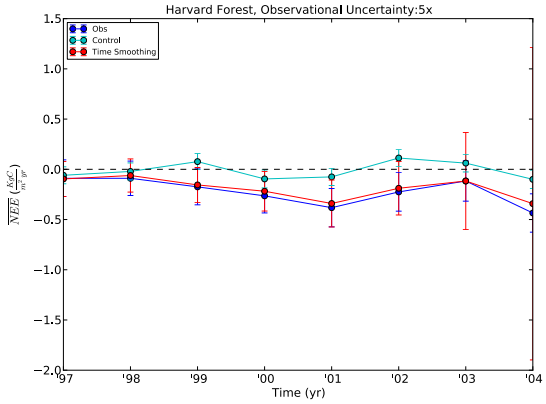

(C) Harvard Forest 5 Times Uncertainty

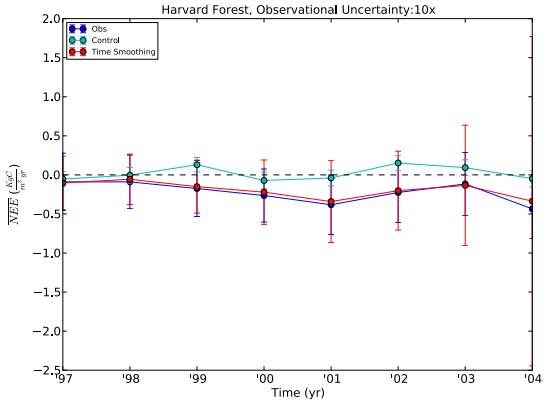

(D) Harvard Forest 10 Times Uncertainty

FIG. 3.10. Time evolution of the annually averaged NEE flux at Harvard Forest under varying amounts of observational uncertainty. Blue and cyan lines are the observations and control simulation. Purple lines are SiB4's simulation pre-assimilation. Green and red lines are the prior and posterior estimates of SiB4 during assimilation. Error bars represent the 1 standard deviation uncertainty in the flux.

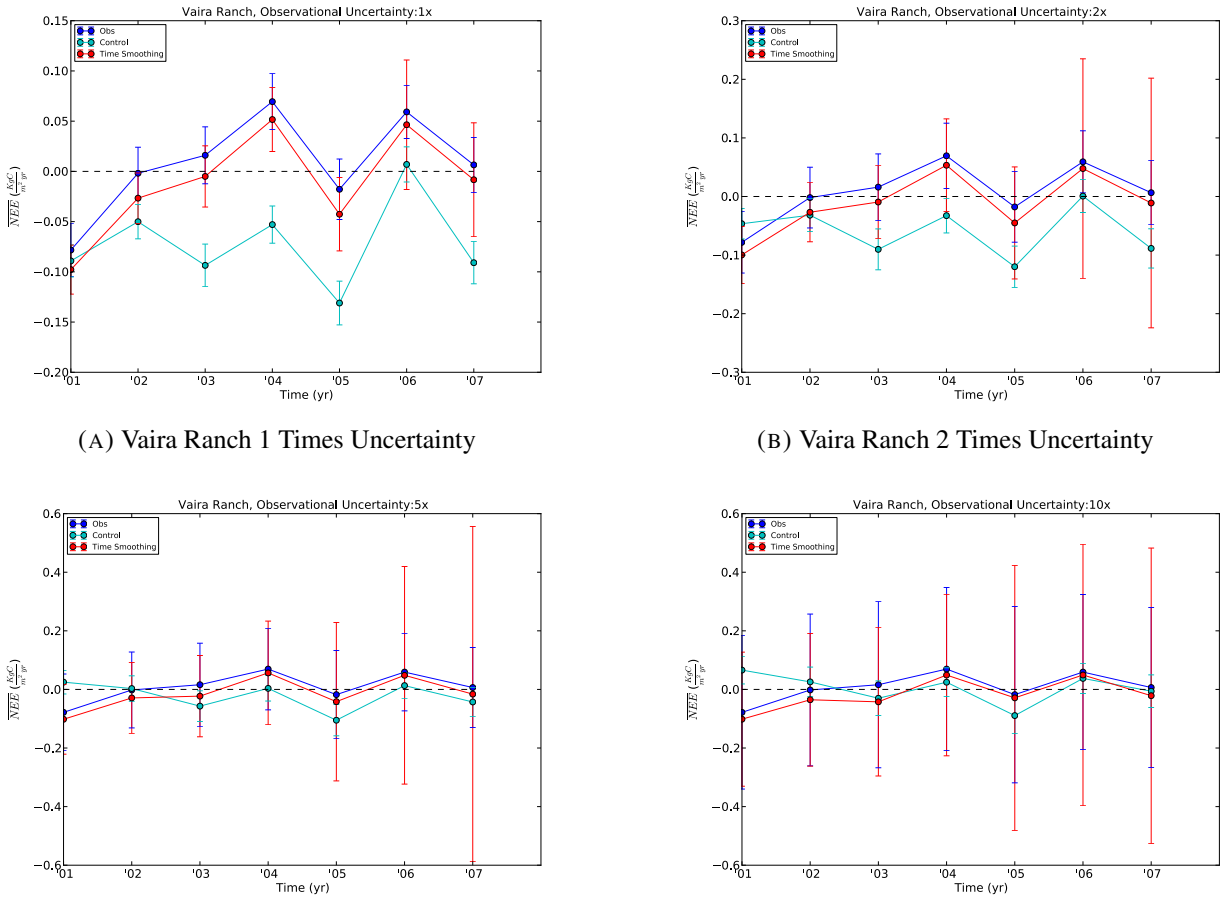

(A) Vaira Ranch 1 Times Uncertainty

(B) Vaira Ranch 2 Times Uncertainty

(C) Vaira Ranch 5 Times Uncertainty

(D) Vaira Ranch 10 Times Uncertainty

FIG. 3.11. Time evolution of the annually averaged NEE flux at Vaira Ranch under varying amounts of observational uncertainty. Blue and cyan lines are the observations and control simulation. Purple lines are SiB4's simulation pre-assimilation. Green and red lines are the prior and posterior estimates of SiB4 during assimilation. Error bars represent the 1 standard deviation uncertainty in the flux.

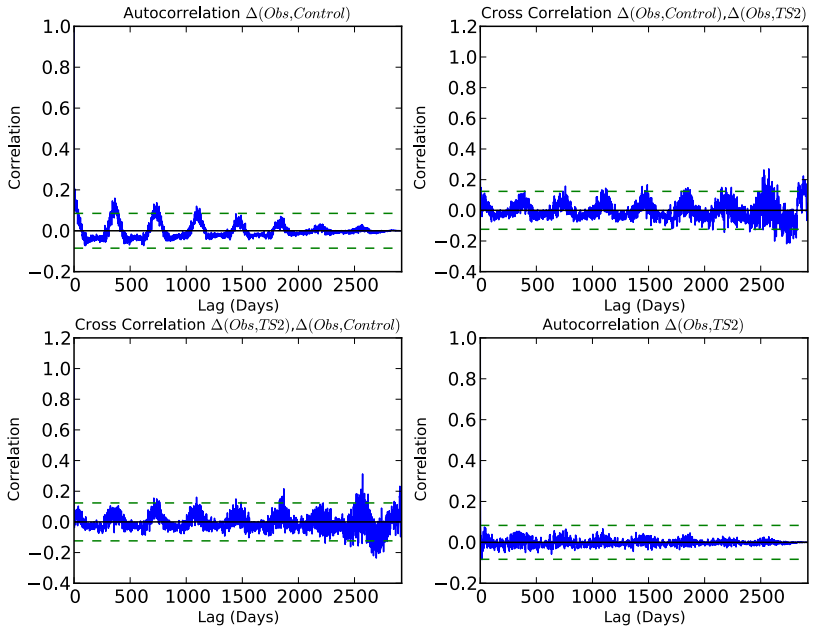

(A) Harvard Forest

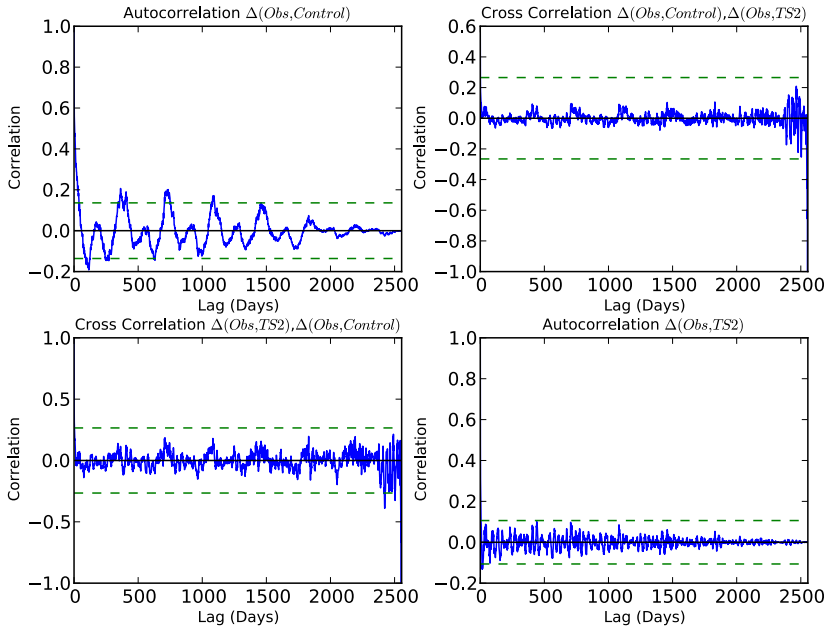

(B) Vaira Ranch

FIG. 3.12. Cross Correlation and Autocorrelation functions between the error timeseries of the control and time smoothing algorithm used in Experiment 2 Harvard Forest and Vaira Ranch. Top Left: Autocorrelation function of error timeseries of the control fit. Top Right: Cross Correlation function of error timeseries where control lags time smoothing. Bottom Left: Cross Correlation function of error timeseries where time smoothing lags control. Bottom Right: Autocorrelation function of error timeseries of the time smoothing fit.

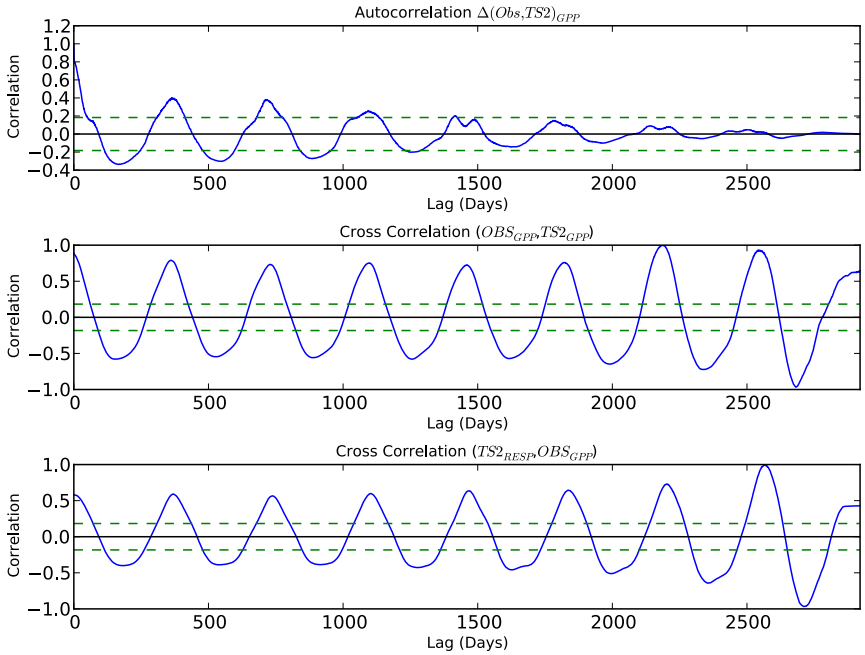

(A) Harvard Forest: GPP

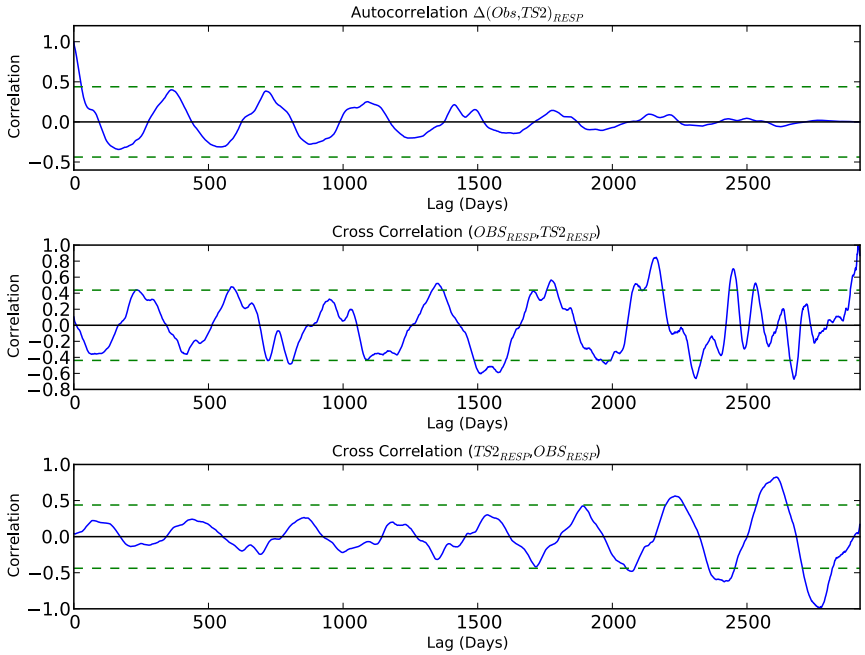

(B) Harvard Forest: RESP

FIG. 3.13. Cross Correlation and Autocorrelation functions between the error timeseries of the control and time smoothing algorithm used in Experiment 2 for Harvard Forest. Top: GPP. Bottom: RESP. First Panel: Autocorrelation function of error timeseries. Middle Panel: Observations lag Time Smoothing Algorithm

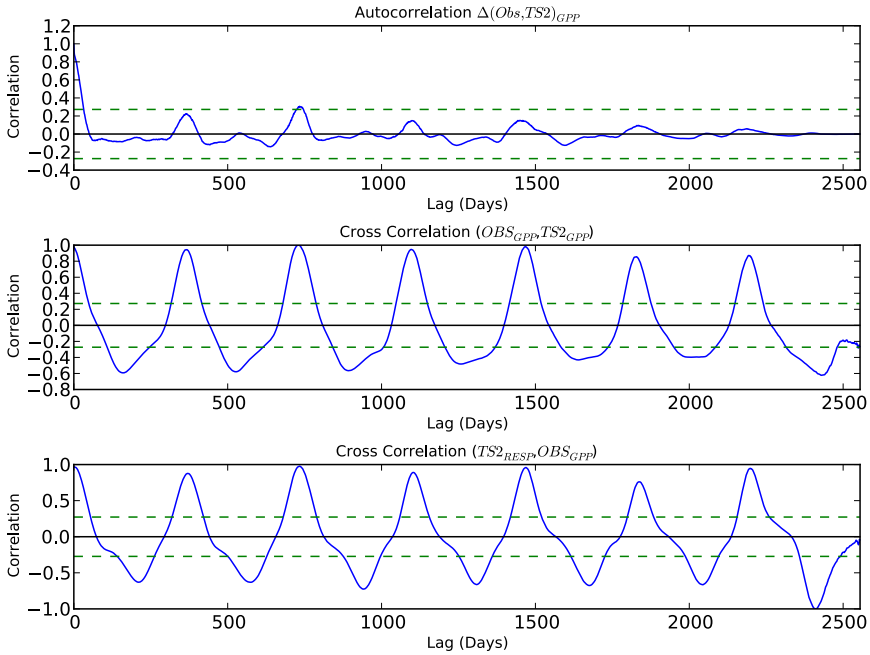

(A) Vaira Ranch: GPP

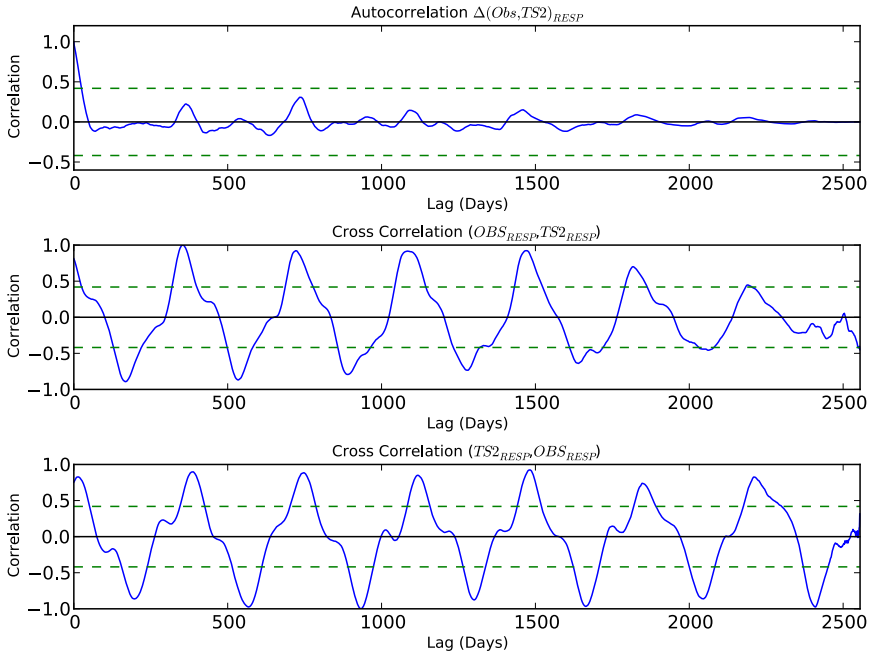

(B) Vaira Ranch: RESP

FIG. 3.14. Cross Correlation and Autocorrelation functions between observation and time smoothing estimation timeseries used in Experiment 2 for Vaira Ranch. Top: GPP. Bottom: RESP. First Panel: Autocorrelation function of error timeseries. Middle Panel: Observations lag Time Smoothing Algorithm

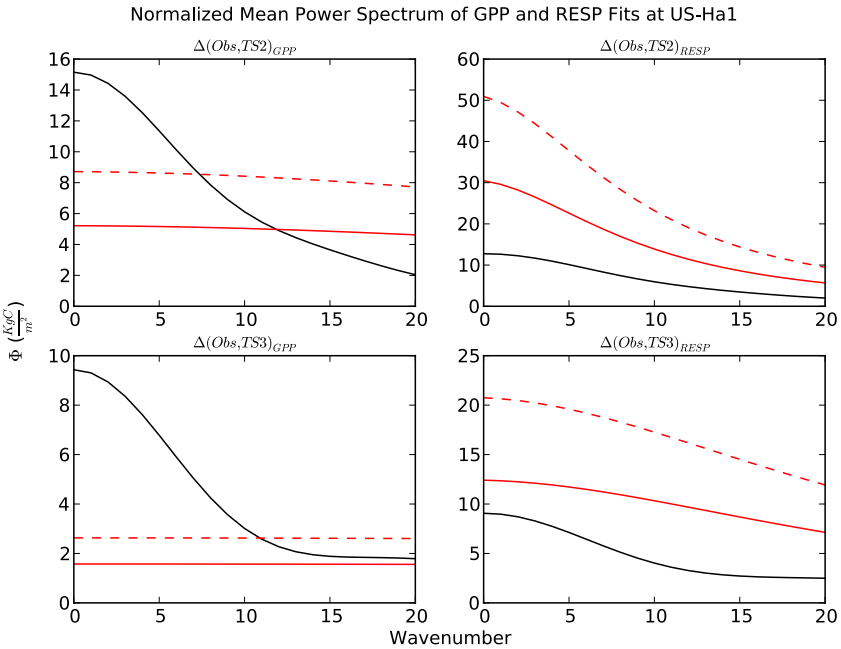

(A) Harvard Forest

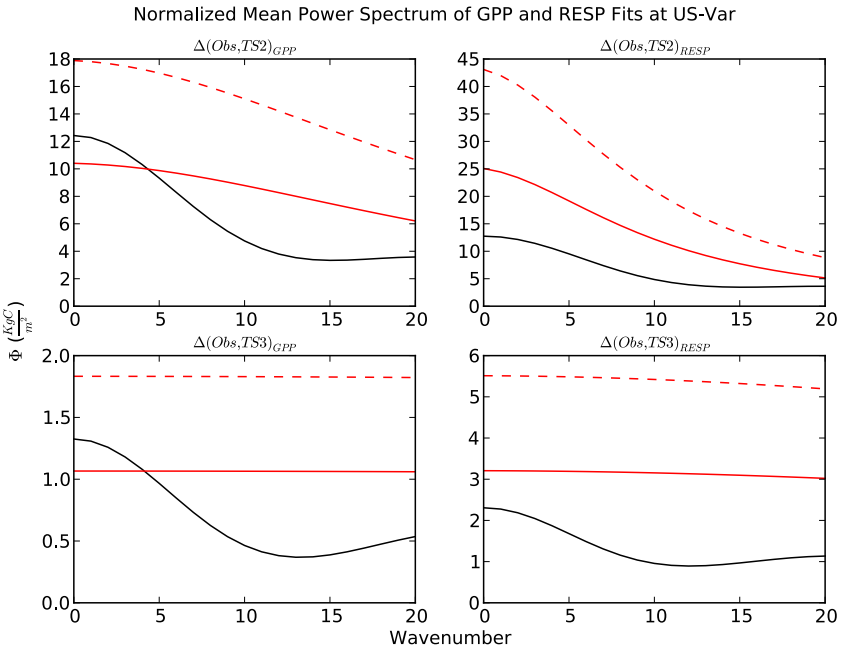

(B) Vaira Ranch

FIG. 3.15. Mean power spectrums of the component flux error for the second and third experiments at Harvard Forest and Vaira Ranch. Black lines are power. Red solid is the red noise power spectrum of the datum, and the dashed red line is the red noise spectrum at the 95th percentile. Top Left: GPP Experiment 2. Top Right: RESP Experiment 2. Bottom Left: GPP Experiment 3. Bottom Right: RESP Experiment 3.

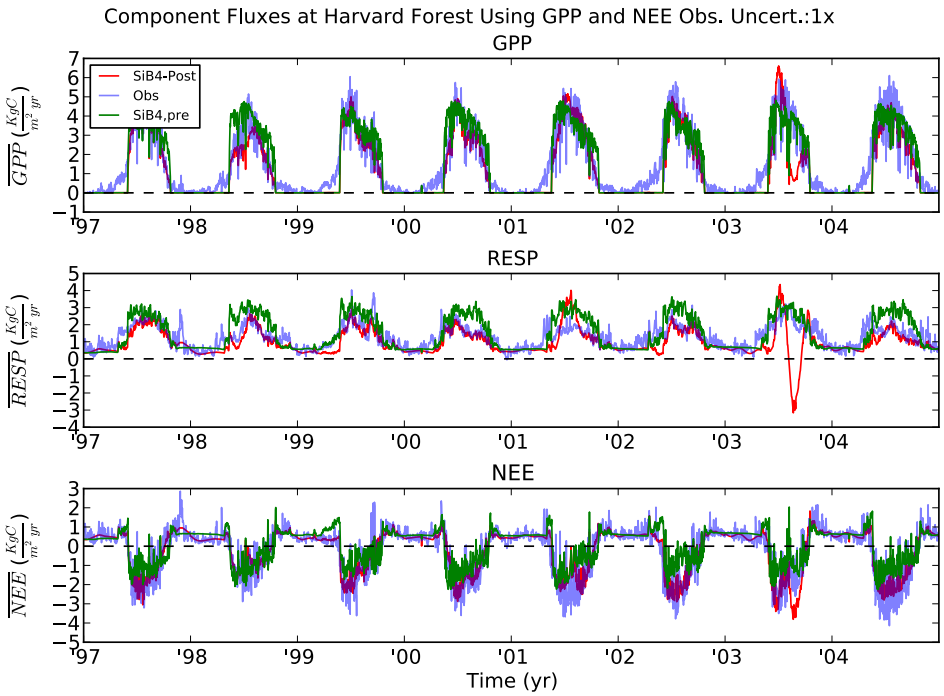

(A) Harvard Forest

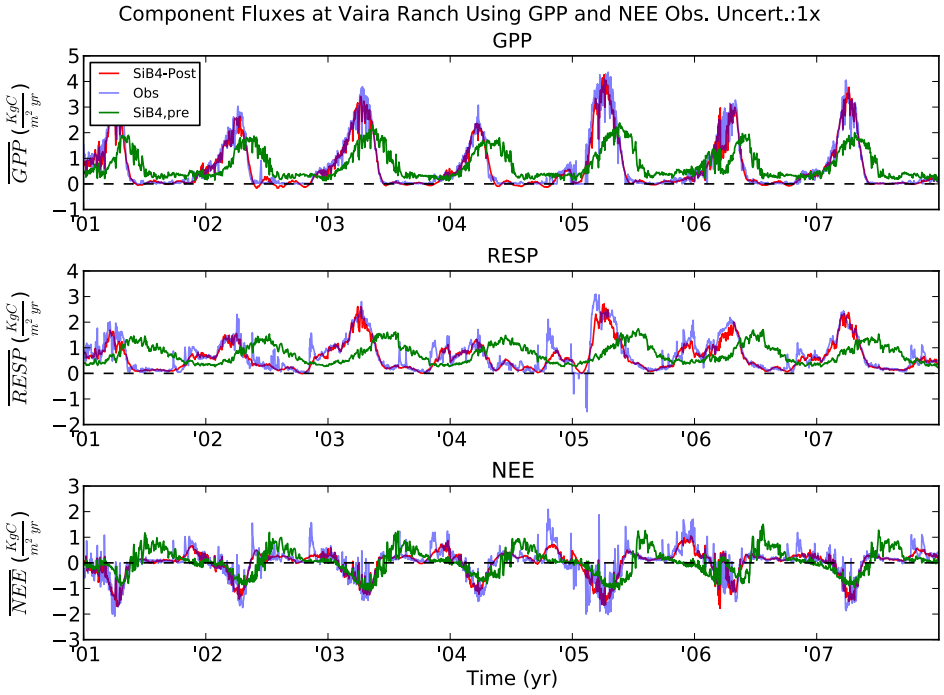

(B) Vaira Ranch

FIG. 3.16. Time evolution of the daily component fluxes of both Harvard Forest and Vaira Ranch as a result of the third experiment. The blue lines are the observations. The red lines are the posterior estimates.

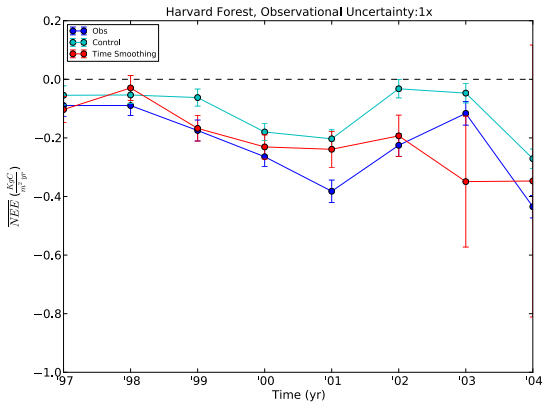

(A) Harvard Forest 1 Times Uncertainty

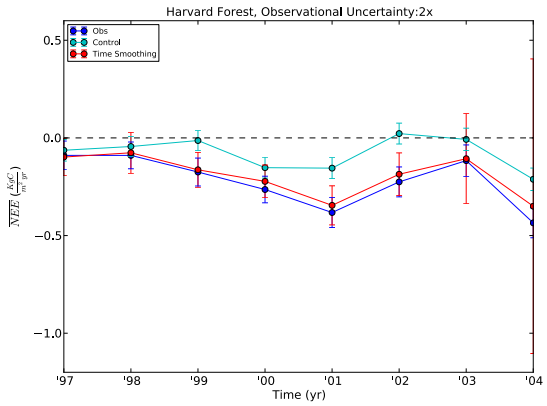

(B) Harvard Forest 2 Times Uncertainty

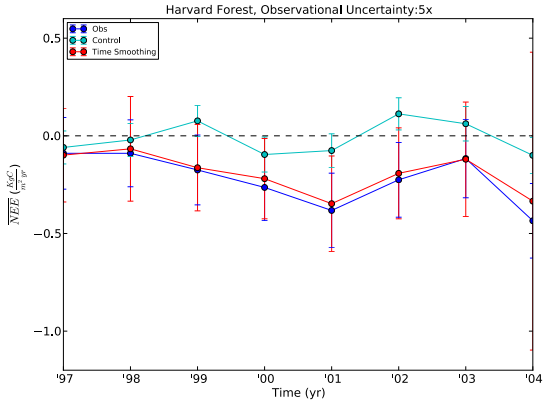

(C) Harvard Forest 5 Times Uncertainty

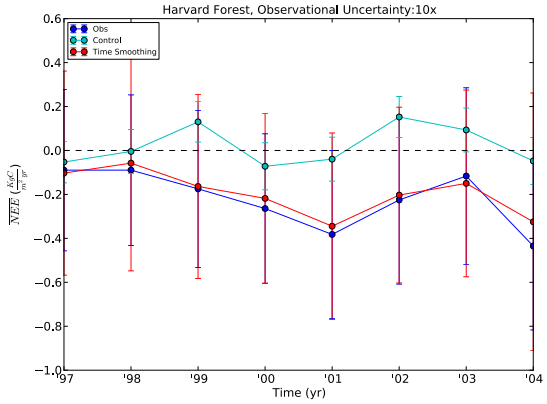

(D) Harvard Forest 10 Times Uncertainty

FIG. 3.17. Time evolution of the annually averaged NEE flux at Harvard Forest under varying amounts of observational uncertainty. Blue and cyan lines are the observations and control simulation. Purple lines are SiB4's simulation pre-assimilation. Green and red lines are the prior and posterior estimates of SiB4 during assimilation. Error bars represent the 1 standard deviation uncertainty in the flux.

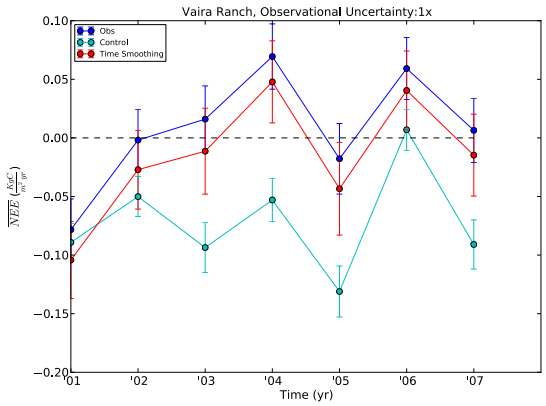

(A) Vaira Ranch 1 Times Uncertainty

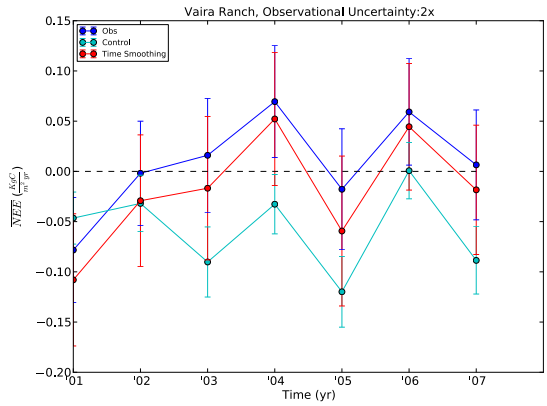

(B) Vaira Ranch 2 Times Uncertainty

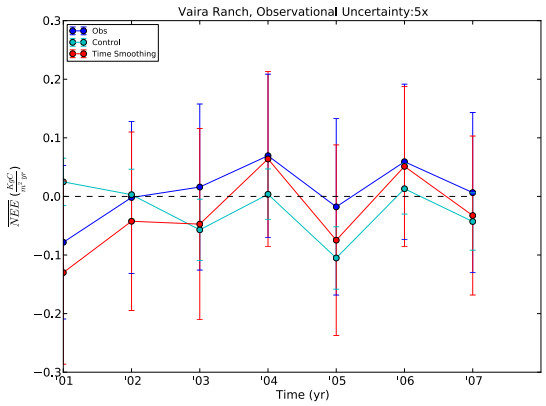

(C) Vaira Ranch 5 Times Uncertainty

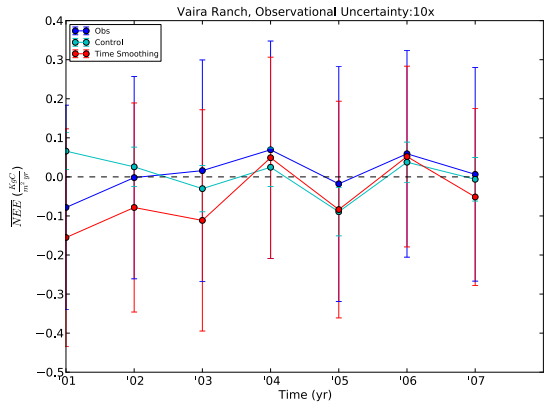

(D) Vaira Ranch 10 Times Uncertainty

FIG. 3.18. Time evolution of the annually averaged NEE flux at Vaira Ranch under varying amounts of observational uncertainty. Blue and cyan lines are the observations and control simulation. Purple lines are SiB4's simulation pre-assimilation. Green and red lines are the prior and posterior estimates of SiB4 during assimilation. Error bars represent the 1 standard deviation uncertainty in the flux.

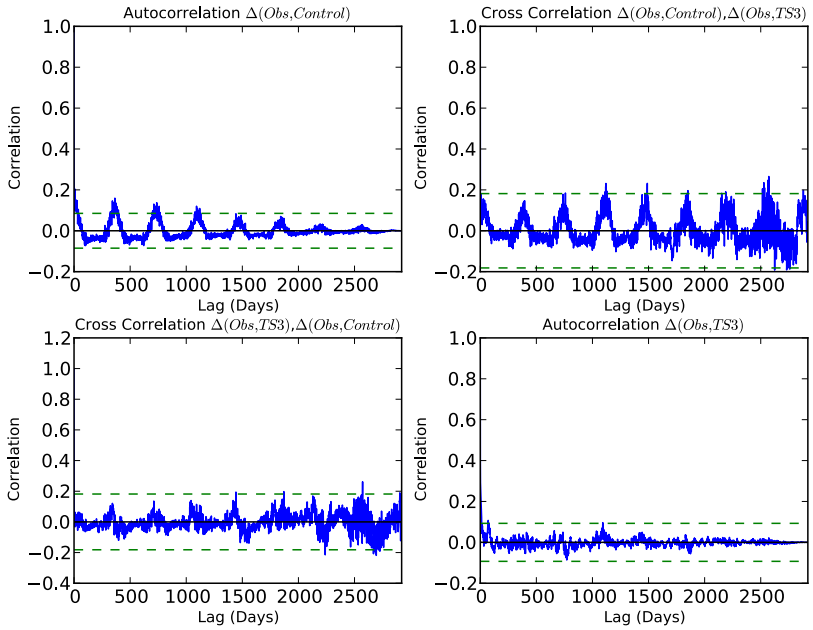

(A) Harvard Forest

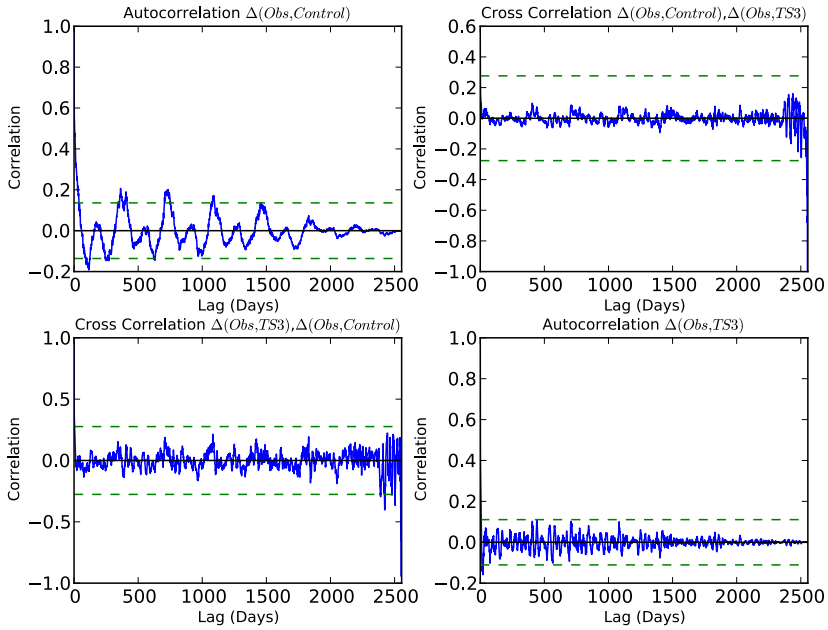

(B) Vaira Ranch

FIG. 3.19. Cross Correlation and Autocorrelation functions between the error timeseries of the control and time smoothing algorithm used in Experiment 3 Harvard Forest and Vaira Ranch. Top Left: Autocorrelation function of error timeseries of the control fit. Top Right: Cross Correlation function of error timeseries where control lags time smoothing. Bottom Left: Cross Correlation function of error timeseries where time smoothing lags control. Bottom Right: Autocorrelation function of error timeseries of the time smoothing fit.

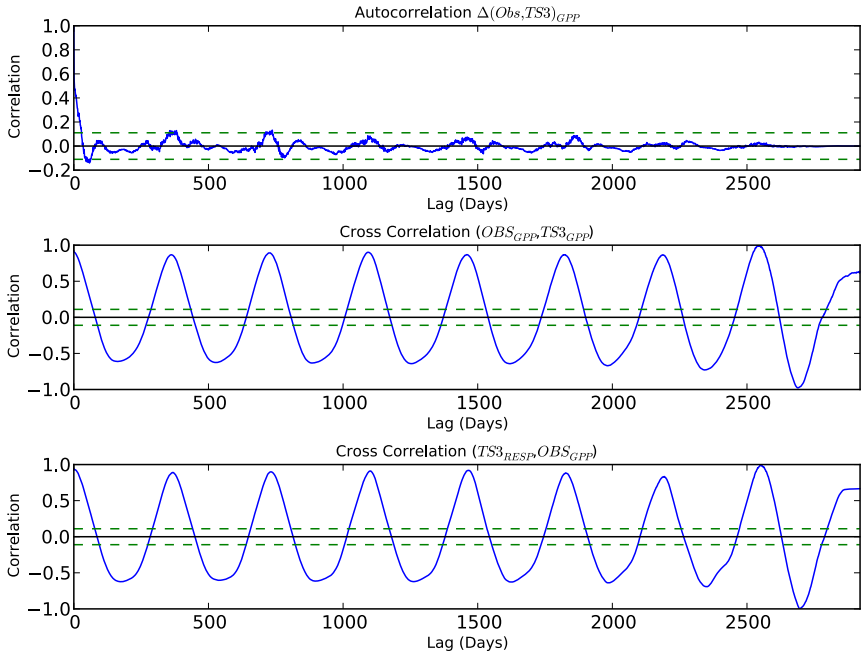

(A) Harvard Forest: GPP

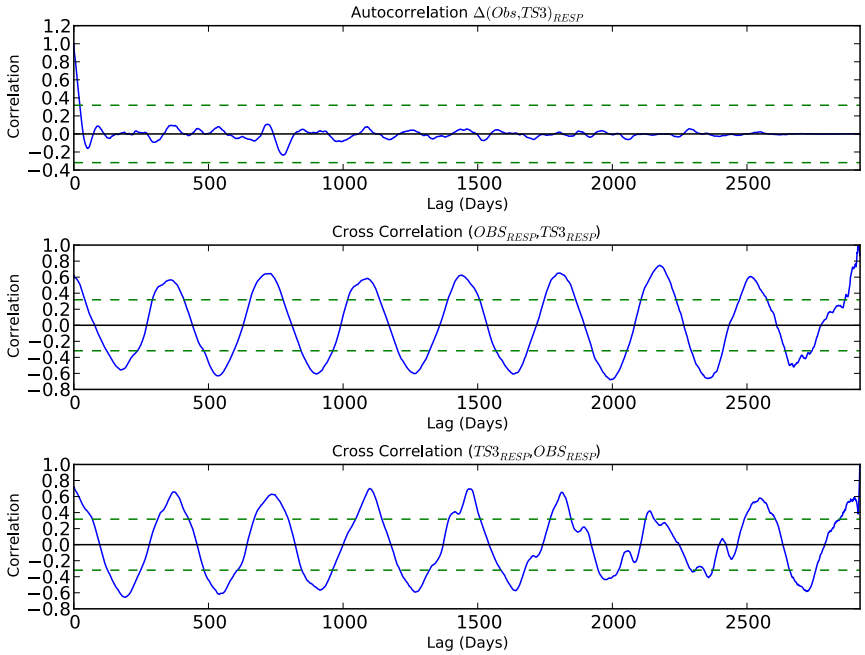

(B) Harvard Forest: RESP

FIG. 3.20. Cross Correlation and Autocorrelation functions between the error timeseries of the control and time smoothing algorithm used in Experiment 3 for Harvard Forest. Top: GPP. Bottom: RESP. First Panel: Autocorrelation function of error timeseries. Middle Panel: Observations lag Time Smoothing Algorithm

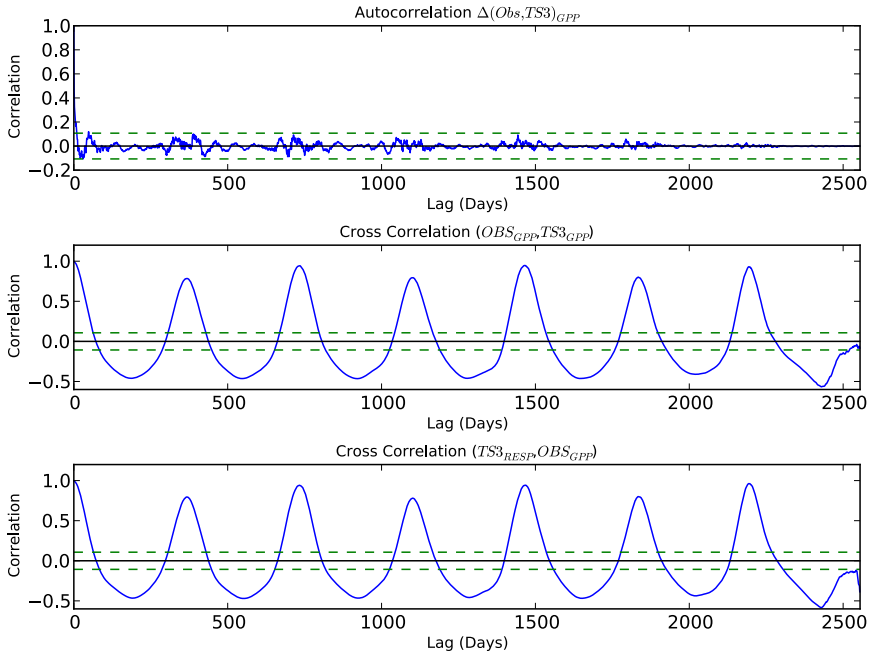

(A) Vaira Ranch: GPP

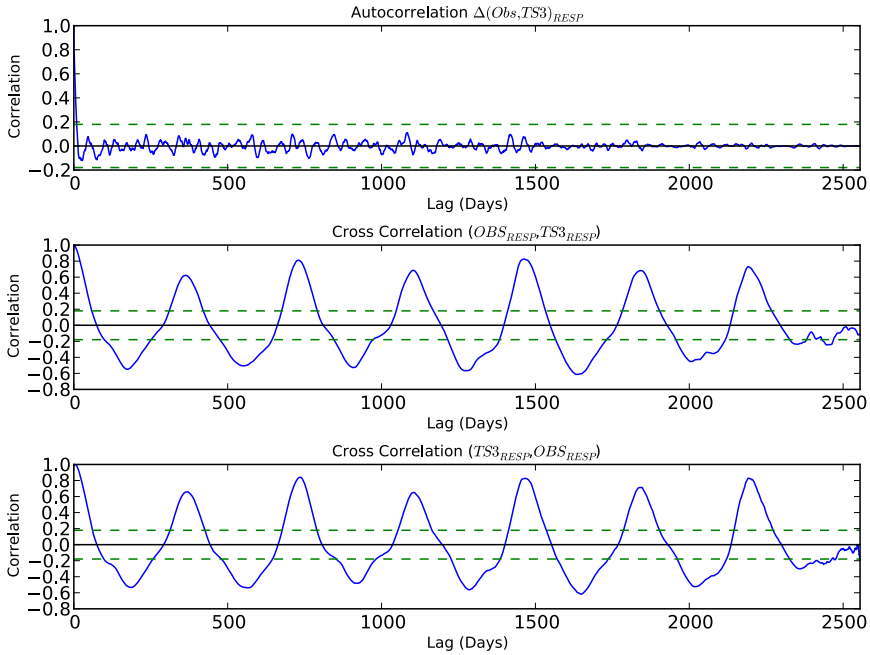

(B) Vaira Ranch: RESP

FIG. 3.21. Cross Correlation and Autocorrelation functions between observation and time smoothing estimation timeseries used in Experiment 3 for Vaira Ranch. Top: GPP. Bottom: RESP. First Panel: Autocorrelation function of error timeseries. Middle Panel: Observations lag Time Smoothing Algorithm

TABLE 3.1. Results of the suite of statistical tests performed on the data generated from Experiment 1. *P* means the statistical test rejected the null hypothesis and *F* means the statistical test failed to rejected the null hypothesis

(A) NEE

Site Name	Paired T-Test P-value	X-Corr (Control/TS) ΔZ_{crit} (Max, Mean, Min)	X-Corr (TS/Control) ΔZ_{crit} (Max, Mean, Min)	Autocorr (TS) ΔZ_{crit} (Max, Mean, Min)	Ljung-Box Test P-value	Mean Φ ($\overline{\Phi}$ k=1)
Harvard Forest	F 0.22	F 0.00, 0.03, 0.87	F 0.00, 0.04, 0.87	F 0.00, 0.05, 0.91	P 0.00	F 1.45, 1.36
U. of Mich. Biol. Stat.	F 0.15	F 0.00, 0.08, 0.81	F 0.00, 0.07, 0.81	F 0.00, 0.08, 0.86	P 0.00	P 1.67, 1.78
Old Black Spruce	F 0.39	F 0.00, 0.05, 0.88	F 0.00, 0.06, 0.88	P 0.00, 0.11, 0.89	P 0.00	P 1.36, 1.96
Campbell River	P 0.00	F 0.00, 0.05, 0.87	F 0.00, 0.03, 0.87	P 0.00, 0.12, 0.91	P 0.00	P 0.42, 1.51
ARM-SGP	F 0.99	P 0.02, 0.38, 0.73	P 0.01, 0.37, 0.73	P 0.00, 0.19, 0.85	P 0.00	P 1.35, 2.14
Mead-Irrigated	F 0.94	F 0.00, 0.08, 0.81	F 0.00, 0.09, 0.81	F 0.00, 0.10, 0.86	P 0.00	P 0.57, 2.07
Vaira Ranch	P 0.05	F 0.00, 0.06, 0.58	F 0.00, 0.05, 0.72	F 0.00, 0.17, 0.86	P 0.00	F 3.74, 3.18
Lethbridge	F 0.63	F 0.00, 0.07, 0.81	F 0.00, 0.10, 0.81	P 0.00, 0.10, 0.87	P 0.00	P 2.59, 2.76

TABLE 3.2. Results of the suite of statistical tests performed on the data generated from Experiment 2. *P* means the statistical test rejected the null hypothesis and *F* means the statistical test failed to rejected the null hypothesis

(A) GPP

Site Name	Paired T-Test P-value	X-Corr (Obs/TS) ΔZ_{crit} (Max, Mean, Min)	X-Corr (TS/Obs) ΔZ_{crit} (Max, Mean, Min)	Autocorr (TS) ΔZ_{crit} (Max, Mean, Min)	Ljung-Box Test P-value	Mean Φ ($\overline{\Phi}$ k=1)
Harvard Forest	P 0.00	F 0.00, 0.39, 0.82	F 0.00, 0.29, 0.82	F 0.00, 0.12, 0.82	P 0.00	F 14.97, 8.71
U. of Mich. Biol. Stat.	P 0.02	F 0.00, 0.22, 0.62	F 0.00, 0.23, 0.62	P 0.01, 0.31, 0.62	P 0.00	P 8.47, 14.85
Old Black Spruce	F 0.14	F 0.00, 0.33, 0.68	F 0.00, 0.31, 0.68	F 0.00, 0.15, 0.68	P 0.00	P 15.93, 23.36
Campbell River	P 0.00	F 0.00, 0.37, 0.80	F 0.00, 0.35, 0.83	P 0.00, 0.15, 0.83	P 0.00	F 21.38, 11.59
ARM-SGP	P 0.03	F 0.00, 0.19, 0.39	F 0.00, 0.18, 0.57	P 0.00, 0.32, 0.64	P 0.00	P 5.44, 12.71
Mead-Irrigated	P 0.00	F 0.00, 0.29, 0.67	F 0.00, 0.28, 0.67	P 0.00, 0.19, 0.67	P 0.00	P 10.72, 14.32
Vaira Ranch	P 0.00	F 0.00, 0.40, 0.73	F 0.00, 0.38, 0.70	P 0.00, 0.22, 0.73	P 0.00	P 12.28, 17.81
Lethbridge	P 0.00	F 0.00, 0.18, 0.76	F 0.00, 0.25, 0.76	P 0.02, 0.36, 0.76	P 0.00	P 8.81, 9.49

(B) RESP

Site Name	Paired T-Test P-value	X-Corr (Obs/TS) ΔZ_{crit} (Max, Mean, Min)	X-Corr (TS/Obs) ΔZ_{crit} (Max, Mean, Min)	Autocorr (TS) ΔZ_{crit} (Max, Mean, Min)	Ljung-Box Test P-value	Mean Φ ($\overline{\Phi}$ k=1)
Harvard Forest	P 0.00	F 0.00, 0.14, 0.56	P 0.00, 0.19, 0.39	P 0.01, 0.29, 0.56	P 0.00	P 12.63, 49.46
U. of Mich. Biol. Stat.	F 0.20	P 0.00, 0.00, 0.00	P 0.00, 0.00, 0.00	P 0.00, 0.00, 0.00	P 0.00	P 7.46, 68.68
Old Black Spruce	F 0.14	F 0.00, 0.18, 0.46	F 0.00, 0.18, 0.46	F 0.01, 0.24, 0.46	P 0.00	P 14.12, 65.95
Campbell River	P 0.00	F 0.00, 0.28, 0.56	F 0.00, 0.32, 0.70	P 0.00, 0.17, 0.70	P 0.00	P 21.70, 34.19
ARM-SGP	F 0.09	P 0.00, 0.07, 0.11	P 0.00, 0.07, 0.15	P 0.00, 0.22, 0.40	P 0.00	P 5.39, 32.69
Mead-Irrigated	P 0.00	F 0.00, 0.15, 0.31	F 0.00, 0.14, 0.31	P 0.01, 0.18, 0.34	P 0.00	P 9.05, 54.54
Vaira Ranch	P 0.00	F 0.00, 0.28, 0.58	F 0.00, 0.26, 0.51	P 0.02, 0.30, 0.58	P 0.00	P 12.59, 41.98
Lethbridge	F 0.38	P 0.00, 0.09, 0.32	F 0.00, 0.16, 0.32	P 0.03, 0.19, 0.32	P 0.00	P 5.22, 68.65

(C) NEE

Site Name	Paired T-Test P-value	X-Corr (Control/TS) ΔZ_{crit} (Max, Mean, Min)	X-Corr (TS/Control) ΔZ_{crit} (Max, Mean, Min)	Autocorr (TS) ΔZ_{crit} (Max, Mean, Min)	Ljung-Box Test P-value	Mean Φ ($\overline{\Phi}$ k=1)
Harvard Forest	P 0.00	P 0.00, 0.04, 0.88	P 0.00, 0.05, 0.88	P 0.12, 0.52, 0.92	P 0.00	P 0.40, 0.95
U. of Mich. Biol. Stat.	P 0.02	P 0.01, 0.13, 0.75	P 0.75, 0.75, 0.75	P 0.00, 0.20, 0.87	P 0.00	P 0.47, 1.21
Old Black Spruce	P 0.00	P 0.00, 0.05, 0.88	P 0.00, 0.06, 0.88	P 0.00, 0.11, 0.89	P 0.00	P 0.87, 1.58
Campbell River	P 0.00	P 0.00, 0.17, 0.84	P 0.01, 0.14, 0.84	P 0.07, 0.41, 0.92	P 0.00	P 0.02, 1.21
ARM-SGP	P 0.00	P 0.78, 0.78, 0.78	P 0.78, 0.78, 0.78	P 0.01, 0.32, 0.87	P 0.00	P 0.16, 1.24
Mead-Irrigated	P 0.00	F 0.00, 0.07, 0.84	F 0.00, 0.08, 0.84	P 0.12, 0.50, 0.88	P 0.00	P 0.13, 1.20
Vaira Ranch	P 0.00	P 0.29, 0.29, 0.29	P 0.01, 0.25, 0.72	P 0.06, 0.29, 0.89	P 0.00	P 0.43, 1.73
Lethbridge	P 0.00	P 0.05, 0.40, 0.76	P 0.00, 0.10, 0.76	P 0.00, 0.27, 0.90	P 0.00	F 1.79, 1.41

TABLE 3.3. Results of the suite of statistical tests performed on the data generated from Experiment 3. *P* means the statistical test rejected the null hypothesis and *F* means the statistical test failed to rejected the null hypothesis

(A) GPP

Site Name	Paired T-Test P-value	X-Corr (Obs/TS) ΔZ_{crit} (Max, Mean, Min)	X-Corr (TS/Obs) ΔZ_{crit} (Max, Mean, Min)	Autocorr (TS) ΔZ_{crit} (Max, Mean, Min)	Ljung-Box Test P-value	Mean Φ ($\overline{\Phi}$ k=1)
Harvard Forest	P 0.00	F 0.00, 0.46, 0.89	F 0.00, 0.47, 0.88	P 0.00, 0.11, 0.89	P 0.00	F 9.31, 2.63
U. of Mich. Biol. Stat.	P 0.00	F 0.00, 0.44, 0.85	F 0.00, 0.46, 0.85	P 0.01, 0.12, 0.85	P 0.00	F 6.02, 2.27
Old Black Spruce	P 0.00	F 0.00, 0.51, 0.90	F 0.00, 0.50, 0.87	F 0.00, 0.06, 0.90	P 0.00	F 3.86, 1.56
Campbell River	P 0.00	F 0.00, 0.35, 0.92	F 0.00, 0.31, 0.92	P 0.02, 0.29, 0.92	P 0.00	F 4.40, 1.13
ARM-SGP	P 0.00	F 0.00, 0.37, 0.82	F 0.00, 0.36, 0.82	F 0.01, 0.21, 0.82	P 0.00	P 2.17, 3.28
Mead-Irrigated	P 0.00	F 0.00, 0.33, 0.78	F 0.00, 0.33, 0.78	F 0.00, 0.16, 0.78	P 0.00	P 5.53, 6.32
Vaira Ranch	P 0.00	F 0.00, 0.45, 0.89	F 0.00, 0.45, 0.89	P 0.01, 0.20, 0.89	P 0.00	P 1.31, 1.83
Lethbridge	P 0.00	F 0.00, 0.26, 0.89	F 0.00, 0.26, 0.89	P 0.00, 0.12, 0.89	P 0.00	F 6.68, 2.05

(B) RESP

Site Name	Paired T-Test P-value	X-Corr (Obs/TS) ΔZ_{crit} (Max, Mean, Min)	X-Corr (TS/Obs) ΔZ_{crit} (Max, Mean, Min)	Autocorr (TS) ΔZ_{crit} (Max, Mean, Min)	Ljung-Box Test P-value	Mean Φ ($\overline{\Phi}$ k=1)
Harvard Forest	P 0.00	F 0.00, 0.21, 0.68	F 0.00, 0.18, 0.68	P 0.01, 0.33, 0.68	P 0.00	P 8.97, 20.64
U. of Mich. Biol. Stat.	P 0.00	F 0.00, 0.30, 0.66	F 0.00, 0.39, 0.66	P 0.01, 0.18, 0.66	P 0.00	P 6.05, 12.58
Old Black Spruce	P 0.00	F 0.00, 0.48, 0.84	F 0.00, 0.47, 0.84	P 0.00, 0.10, 0.84	P 0.00	P 4.14, 4.67
Campbell River	P 0.00	F 0.00, 0.42, 0.87	F 0.00, 0.39, 0.87	P 0.01, 0.26, 0.87	P 0.00	F 6.28, 3.90
ARM-SGP	P 0.00	F 0.00, 0.30, 0.76	F 0.00, 0.18, 0.76	P 0.00, 0.27, 0.76	P 0.00	P 2.24, 5.77
Mead-Irrigated	P 0.00	F 0.00, 0.22, 0.54	F 0.00, 0.20, 0.54	P 0.00, 0.15, 0.54	P 0.00	P 5.99, 27.24
Vaira Ranch	P 0.00	F 0.00, 0.34, 0.82	F 0.00, 0.36, 0.82	P 0.01, 0.34, 0.82	P 0.00	P 2.28, 5.51
Lethbridge	P 0.00	F 0.00, 0.28, 0.78	F 0.00, 0.28, 0.78	P 0.00, 0.33, 0.78	P 0.00	P 4.21, 8.63

(C) NEE

Site Name	Paired T-Test P-value	X-Corr (Control/TS) ΔZ_{crit} (Max, Mean, Min)	X-Corr (TS/Control) ΔZ_{crit} (Max, Mean, Min)	Autocorr (TS) ΔZ_{crit} (Max, Mean, Min)	Ljung-Box Test P-value	Mean Φ ($\overline{\Phi}$ k=1)
Harvard Forest	P 0.00	P 0.00, 0.06, 0.82	P 0.01, 0.19, 0.82	P 0.00, 0.15, 0.91	P 0.00	P 1.23, 1.39
U. of Mich. Biol. Stat.	P 0.02	P 0.00, 0.38, 0.75	P 0.01, 0.38, 0.75	P 0.01, 0.23, 0.87	P 0.00	P 0.56, 1.13
Old Black Spruce	F 0.14	F 0.00, 0.05, 0.91	P 0.00, 0.04, 0.91	P 0.00, 0.27, 0.91	P 0.00	P 0.30, 1.02
Campbell River	P 0.00	P 0.00, 0.11, 0.86	P 0.00, 0.11, 0.86	P 0.06, 0.40, 0.92	P 0.00	P 0.09, 1.14
ARM-SGP	P 0.03	P 0.00, 0.07, 0.79	P 0.00, 0.09, 0.79	P 0.01, 0.15, 0.87	P 0.00	P 0.21, 1.66
Mead-Irrigated	P 0.00	F 0.00, 0.07, 0.84	F 0.00, 0.08, 0.84	P 0.12, 0.50, 0.88	P 0.00	P 0.13, 1.58
Vaira Ranch	P 0.00	P 0.23, 0.23, 0.23	P 0.01, 0.21, 0.72	P 0.03, 0.26, 0.89	P 0.00	P 0.46, 1.91
Lethbridge	P 0.00	P 0.00, 0.37, 0.73	P 0.01, 0.12, 0.73	P 0.00, 0.23, 0.90	P 0.00	P 1.42, 1.57

CHAPTER 4

DISCUSSION

This section contains a discussion, interpretations, and conclusions regarding the time smoothing algorithm and the overarching hypotheses that the three experiments were designed to address. Table 4.1 shows a summary of the hypothesis conclusions from this and the results section.

4.1. EXPERIMENT 1 INTERPRETATIONS

The first experiment was an "apples-to-apples" comparison of the time-smoothing algorithm and the control algorithm on level terms from a statistics standpoint. The visual results of the average annual source and sink plots gave the inclination that this version of the time smoothing algorithm was capable of making an estimation of the annual and seasonal NEE signals as good or better than the control. Furthermore, the similar reduction of the RMSE of NEE timeseries suggested that the two timeseries were fitted similarly and could have a similar source and sink comparison. However, this was not the case because the paired T-tests suggested that the interannual mean of the errors for this version of the time smoothing algorithm were greater than the control to within statistical confidence levels. The qualitative and quantitative evidence from experiment 1 suggests that a time smoothing algorithm is not capable of estimating better estimates of interannual and annual NEE estimates over a present day algorithm. Thus, hypothesis 1 is rejected. Despite this finding, the seasonality was suggested to be well recovered.

From the seasonality analysis in the first experiment, the time smoothing algorithm was suggested to be capable of properly estimating the seasonal NEE signal at 6 of the 8 sites. While these were all below the 95th confidence interval, these might not be truly robust as the statistics would require them to be. The four sites shown to contain only relative noise when from the

autocorrelation analysis all showed that the seasonal cycle was estimated by the time smoothing algorithm. This was not seen in the control algorithm for these sites. These inability to properly estimate the seasonal cycle across all sites was due to the fact that some of the NEE signals crossed zero suddenly and formulated faster timescale waves than the slow assumptions. These are caused because of seasonal mismatches between the model and observations, which were not completely accounted for in the bias uncertainty. However, the general pattern of the cites with good estimation showed that given the proper uncertainty in both the model and the observations, the time smoothing algorithm could outperform at estimating the seasonality of NEE than the control. Therefore, these results and explanations indicated that hypothesis 2 was either plausible or confirmed for any site given the proper optimization conditions.

The observational uncertainty analysis showed that the time smoothing algorithm is more robust than the control under increased uncertainty. As previously mentioned, the pattern from the results showed that the estimate would first revert to the prior and then progress toward the pre-assimilation model estimation as uncertainty increased. The time smoothing algorithm was more robust because the ”learning” nature of the algorithm. The design of the algorithm is such that if one year is much more certain than another, then an estimate of the bias coefficients could still be made under a large uncertainty. This cannot happen with the control because the posterior bias coefficient covariance matrix is not carried over from cycle-to-cycle. As a result, this evidence and the results of experiment 1 validates the uncertainty criterion for hypotheses 1 and 2.

4.2. Experiment 2 Interpretations

The second experiment showed the impact the time-smoothing algorithm using NEE to optimize for GPP and RESP. Unlike the first experiment, using the time-smoothing algorithm in this

manner demonstrated nearly exact recovery of the observed annually averaged and interannual pattern of NEE at every site to within error estimates of the observations. This result demonstrated the benefit of using the component fluxes over the NEE flux alone in the time-smoothing algorithm. By using the slower varying component fluxes to formulate an NEE prior, the smaller variations of NEE can still be present in the prior. Sudden crosses of zero in the NEE signal can be accounted for by the two constantly non-negative component fluxes. The suite of statistical tests that estimations of NEE in this manner produced lower RMSE and achieved statistically better estimations of the annual NEE sources and sinks over the control algorithm across all sites. Furthermore, the mean power spectrum of NEE revealed that the seasonality is also confidently estimated by the algorithm as well. Therefore, the second experiment was able to confirm hypotheses 3 and 4.

The same conclusions for NEE are true for the estimation of the GPP and RESP fluxes from the second experiment, but are misleading. The second experiment showed that the cost to a highly accurate NEE signal was the warping and disfiguration of the two component fluxes. It was apparent from the spectral analysis that the disguring harmonics were not the seasonal or mean harmonics, but rather the other optimized waves (k=2, 3, 4, and 5). While this may seem like poor behavior, this is the mathematical behavior of using the Kalman filter. The methodology wants to make the best possible estimate with information it was given. In the second experiment, the underlying mathematical principals are only concerned with retrieving the NEE flux and optimizing the bias coefficients based upon only NEE. Starting with the shortest harmonics, the optimization's methodology warps the the information in the modeled GPP and RESP fluxes in order to make an more accurate estimation of NEE. The presence of low seasonal and annual power in the error confirms hypothesis 5. When summarized with the all estimates this confirmation is misleading because of completely unrealistic estimate for either GPP or RESP.

The results of robustness tests for the second experiment indicated that this version of the time-smoothing algorithm is very robust to changes in uncertainty over all sites. This is because the time-smoothing algorithm is still able to capture the observed NEE flux by consistently warping the GPP and RESP fluxes in different manners to fit NEE, depending on the scenario. By examining the evolving timeseries, it was apparent that while some portions of component fluxes are being pulled toward the prior others are being properly pulled toward the observations. This was caused by the mathematical "struggle" of the Kalman filter between the confidence of the prior and observations during each assimilated year. This suggests that the bias coefficients are consistently changing each year to compensate for individual mismatches in the GPP and RESP patterns. Since NEE is very robust over the all uncertainty increases and over all sites, the uncertainty criterion of hypotheses 3 and 4 are satisfied. Since GPP and RESP are almost constantly changing under various uncertainty scenarios, these estimates are not robust. Therefore, the uncertainty criterion for hypothesis 5 was not satisfied.

4.3. Experiment 3 Interpretations

The third experiment demonstrated that it was possible to estimate all three fluxes given that the net and a component fluxes are used the constraining variables. When using these two contraining quantites, the time smoothing algorithm takes advantage of the methodology wanting to make the best possible estimate with information it was given. Since the filter is trying to fit both NEE and GPP, the added benefit this version of the time smoothing algorithm was the ability to capture the other component flux as well.

The conclusions for NEE are similar to that of the second experiment. The slightly worse NEE RMSE was caused by the addition of the observed GPP as an additional constraint. By adding this second flux, this algorithm is more uncertain of one of the two component fluxes for the NEE

optimization. The visual annual averages, fractional RMSE reduction, and the paired T-test for the NEE estimates revealed that this version of the optimization produced better annual NEE averages than the control and comparable values to that of the second experiment. The issues found at Old Black Spruce were due to bias coefficient covariance numerical instability and not the design of the theory itself. Therefore, the third experiment was able to confirm hypothesis 6. Additionally, the mean spectral and autocorrelation analyses suggested that the residual error term of the time smoothing estimate was completely red noise for all sites. This means that both the mean and seasonal cycles were well estimated. Thus, the third experiment was able to confirm hypotheis 7.

The addition of extra observational constraint allowed for GPP and RESP to be properly optimized for most sites. Visually, the timeseries fits showed that GPP and RESP are really well fit from the third experiment. The presence of a reduction in RMSE across most sites showed improvement from the pre-assimilation flux estimates. Furthermore, nearly indistinguishable flux timesseries from the autocorrelation functions, it was evident that the observations and the component flux estimates were nearly identical. The mean spectral analysis of RESP proved that across all sites both the mean and seasonal cycles of RESP were properly estimated. The spectral analysis of GPP showed that some of the sites were incapable of sub-red noise estimation. While statistically significant, this may be irrelavant because the power retreived by mean spectrum is very low across all sites and only about quarter to half of that produced by the second experiment. Using these results in aggregate, it was seen that GPP and RESP were both well estimated by the third experiment. Therefore, the third experiment confirmed hypothesis 8.

Like the second experiment, this version of time smoothing algorithm showed a robust retrieval of annually averaged NEE and daily fluxes under increases in uncertainty estimates across a variety of PFTs. The rate at which the fluxes revert to the prior and original fluxes occurs sooner for some

sites than others. Like the first experiment, this is because the initial observational uncertainty for some sites is greater than that others. This experiment was able to produce more robust estimates than the control algorithm and reverted toward the pre-assimilation flux only slightly sooner than the second experiment. When applied to the GPP and RESP signals, the increasing uncertainty did not produce the same results as the second experiment. As the observational uncertainty increased, GPP tended to revert toward the prior estimate, but RESP was still able to be well estimated. This pattern kept the NEE estimate relatively well constrained and robust. In summary, this suggested that the uncertainty criterion for GPP, RESP, and NEE in hypotheses 6, 7, and 8 were all met.

TABLE 4.1. A summary of the conclusions about whether the hypotheses were accepted (A) or rejected (R). The uncertainty criteria conclusions were denoted as satisfied (S) or unsatisfied (U)

(A) Experiment 1

Hypothesis 1	Hypothesis 2	Uncertainty Criteria NEE
R	C	S

(B) Experiment 2

Hypothesis 3	Hypothesis 4	Hypothesis 5	Uncertainty Criteria NEE	Uncertainty Criteria GPP/RESP
C	C	C	S	U

(C) Experiment 3

Hypothesis 6	Hypothesis 7	Hypothesis 8	Uncertainty Criteria NEE	Uncertainty Criteria GPP/RESP
C	C	C	S	S

CHAPTER 5

CONCLUSIONS AND FUTURE WORK

The purpose of this study was to create a new inversion framework capable of characterizing and adapting to the long-lived biases between land-model gross CO_2 fluxes and observations. This study has shown that in order to do this both the Kalman Filter and harmonics can be used to time smooth the model data to diagnose these long lived biases. Several PFTs over a range of climate regimes showed that the largest sources of error between model simulations and observations were attributed to low wavenumbers that consists of discrepancies in the "slow-varying" model variables. These results were applied upon the time smoothing assimilation algorithm with a yearly assimilation cycles through three different experiments.

These experiments demonstrated that using a small number of harmonics with greater data constraints can produce as good or better estimates of NEE than a comparable weekly assimilation system. The first experiment produced NEE estimates that were unable to be better annual source and sink estimates over a control algorithm when using observed NEE to optimize modeled NEE. However, this experiment showed the time smoothing algorithm was capable of being more robust to increased observational uncertainty estimates and produced good seasonality estimates of NEE. The second experiment concluded that when using observed NEE to optimize for the component fluxes, there is a dramatic increase in the accuracy of both the magnitude and interannual/seasonal cycles of NEE over just using modeled NEE itself. This accuracy came at the price of a poor recovery of the two component fluxes for sub-seasonal harmonics, but the NEE estimate was very robust over several observational uncertainty increases. The third experiment found that when a observed component flux is used to further constrain the time-smoothing algorithm, all three fluxes are well estimated on all timescales over a variety observational uncertainty increases. For all

variants of the time smoothing algorithm, the posterior estimation was able to overcome seasonal phase shifts, crop and harvest mistimings, and flux magnitude errors present in the prior fluxes. Given there are improvements with better observations and uncertainty estimates, this algorithm could one day serve to really understand the issues in land-models and how ecosystems generally behave under different biological circumstances.

There will be several imporvements to this work in future studies. One way will be to both improve this assimilation algorithm and to apply it in a more general sense. This can be done by incorporating more eddy-covariance data over an even wider assortment of climates to truly obtain the strengths and weaknesses of this algorithm. One adjustment to the algorithm should include a consistent way of estimating the number of harmonics needed for optimization. An example to estimate this number of harmonics required may be the usage of variance explained by the observation-model errors to set a parameter as a cut off point between slow and fast harmonics. This would keep the number of resolved harmonics to minimum number of slow processes. Another adjustment would be a better way to estimate the uncertainty estimate of the land-model. Since this study revolved around an assumption that modeled RESP and GPP did not covary with one another, future studies must make a more realistic assumption and relate these two quanities. A third update would be to address the observational uncertainty matrix. Introduction of a more thorough covariance matrix where the proper relations between NEE and the component flux would dramatically increase the robustness and accuracy of this algorithm beyond its tested capabilities. A final update would be to design an algorithm to adjust the tuning parameter of the covariance update step in such a way so that the model uncertainty matrix does not converge and skew or break the bias coefficient adjustments. A robust way is to use some sort normalized difference between

the model and observations to give a general idea of how uncertain the model is to begin with and how our initial conditions should be shaped.

Future applications of this algorithm should be to apply it to multiple land-models to see how and where these biases exist. Traditionally, these models are balanced on an annual basis, which makes the three gross fluxes all interconnected within the theory and application. Isolation of a variety of "slow-varying" poorly understood parameters should be chosen as the implementation points for this algorithm's influence. Improvements in land-models are always happening and with these improvments land-models can produce better prior constraints for inversion model simulations of regional and global sources and sinks of CO_2.

REFERENCES

Baker, D. F., et al., 2006: TransCom 3 inversion intercomparison: Impact of transport model errors on the interannual variability of regional CO2 fluxes, 19882003. *Global Biogeo. Cyc.*, **20**, GB1002.

Baker, I. T., L. Prihodko, A. S. Denning, M. Goulden, S. Miller, and H. R. da Rocha, 2008: Seasonal Drought Stress in the Amazon: Reconciling Models and Observations. *J. Geophys. Res.*, **113**, G00B01, doi:10.1029/2007JG000644.

Bakwin, P. S., P. P. Tans, D. F. Hurst, and C. Zhao, 1998: Measurements of carbon dioxide on very tall towers: Results of the NOAA/CMDL program. *Tellus*, **50B**, 401–415.

Baldocchi, D., 2008: 'breathing' of the terrestrial biosphere: Lessons learned from a global network of carbon dioxide flux measurement systems. *Aust. J. Bot.*, **56**, 1–26.

Baldocchi, D. and Coauthors, 2001: FLUXNET: A New Tool to Study the Temporal and Spatial Variability of EcosystemScale Carbon Dioxide, Water Vapor, and Energy Flux Densities. *Bull. Amer. Meteor. Soc.*, **82**, 2415–2434.

Ball, J. T., 1988: An analysis of stomatal conductance. Ph.D. thesis, Stanford University.

Barr, A. G., T. A. Black, E. H. Hogg, N. Kljun, K. Morgenstern, and Z. Nesic, 2004: Inter-annual Variability in the Leaf Area Index of a Boreal Aspen-Hazelnut Forest in Relation to Net Ecosystem Production. *Agric. For. Meteor.*, **126**, 237–255, doi:10.1016/j.agrformet.2004.06.011.

Barr, A. G., et al., 2013: NACP Site: Tower Meteorology, Flux Observations with Uncertainty, and Ancillary Data [Dataset]. URL `http://daac.ornl.gov`.

Bolin, B. and W. Bischoff, 1970: Variations of the carbon dioxide content of the atmosphere in the northern hemisphere. *Tellus*, **22**, 431–442.

Bolin, B. and E. Eriksson, 1958: *Changes in the Carbon Dioxide Content of the Atmosphere and Sea due to Fossil Fuel Combustion*. The Rockafeller Int. Press, New York, NY, USA.

Bolin, B. and C. D. Keeling, 1963: Large scale atmospheric mixing as deducted from the seasonal and meridional variations in carbon dioxide. *J. Geophys. Res.*, **68**, 3899.

Bonan, G. B., S. Levis, L. Kergoat, and K. W. Oleson, 2002: Landscapes as patches of plant functional types: An integrating concept for climate and ecosystem models. *Global Biogeo. Cyc.*, **16**, 1021, doi:10.1029/2000GB001360.

CarbonTracker, 2014: *CarbonTracker Documentation CT2013 Release*. ESRL.

Chevallier, F., F.-M. Bréon, and P. J. Rayner, 2007: Contribution of the Orbiting Carbon Observatory to the estimation of CO_2 sources and sinks: Theoretical study in a variational data

assimilation framework. *J. Geophys. Res.*, **112**, D09 307, doi:10.1029/2006JD007375.

Chevallier, F., S. Maksyutov, P. Bousquet, F.-M. Bréon, R. Saito, Y. Yoshida, and T. Yokota, 2009: On the accuracy of the CO_2 surface fluxes to be estimated from the GOSAT observations. *Geophys. Res. Lett.*, **36**, L19 807, doi:10.1029/2009GL040108.

Chevallier, F. and C. W. O'Dell, 2013: Error statistics of Baysian CO_2 flux inversion schemes as seen from GOSAT. *Geophys. Res. Lett.*, **40**, 1252–1256, doi:10.1002/grl.50228.

Ciais, P., P. P. Tans, M. Trolier, J. W. C. White, and R. J. Francey, 1995: A large northern hemisphere terrestrial CO_2 sink indicated by the $^{13}C/^{12}C$ ratio of atmospheric CO_2. *Science*, **269**, 1098–1102.

Collatz, G. J., J. Ball, C. Grivet, and J. A. Berry, 1991: Physiological and environmental regulation of stomatal conductance, photosynthesis and transpiration: a model that includes a laminar boundary layer. *Agric. For. Meteorol.*, **54**, 107–136.

Collatz, G. J., M. Ribas-Carbo, and J. A. Berry, 1992: Coupled Photosynthesis-Stomatal Conductance Model for Leaves of C_4 Plants. *Aust. J. Plant Physiol.*, **19**, 519–513.

Denning, A. S., J. Collatz, C. Zhang, D. Randall, J. Berry, P. Sellers, G. Colello, and D. Dazlich, 1996: Simulations of terrestrial carbon metabolism and atmospheric CO2 in a general circulation model. Part 1: Surface carbon fluxes. *Tellus*, **48B**, 521–542.

Denning, A. S., et al., 1999: Three-dimensional transport and concentration of SF2: A model intercomparison study (TransCom 2). *Tellus*, **51B**, 266–297.

Desai, A. R., et al., 2008: Cross-site evaluation of eddy covariance GPP and RE decomposition techniques. *Agric. For. Meteor.*, **148**, 821 – 383, doi:10.1016/j.agrformet.2007.11.012.

Drever, J. I., 1988: *The Geochemistry of Natural Waters*. Prentice Hall, Englewood Cliffs, NJ, USA.

ESRL, 2014: Earth System Research Laboratory Global Monitoring Division: Up-to-Date Weekly Average CO_2 at Mauna Loa. URL `http://www.esrl.noaa.gov/gmd/ccgg/trends/weekly.html`.

Evensen, G., 1994: Sequential data assimilation with a nonlinear quasi-geostrophic model using Monte Carlo methods to forecast error statistics. *J. Geophys. Res.*, **99**, 10 143–10 162.

Evensen, G., 2009: *Data Assimilation: The Ensemble Kalman Filter*. 2d ed., Springer-Verlag, 307 pp.

Farquhar, G. D., S. von Caemmerer, and J. A. Berry, 1980: A Biochemical Model of Photosynthetic CO_2 Assimilation in Leaves of C_3 Species. *Planta*, **149**, 78–90.

Fischer, M. L., D. P. Billesbach, W. J. Riley, J. A. Berry, and M. S. Torn, 2007: Spatiotemporal Variations in Growing Season Exchanges of CO2, H2O, and Sensible Heat in Agricultural Fields of the Southern Great Plains. *Earth Interact*, **11**, 1–21, doi:10.1175/EI231.1.

Flanagan, L. B. and A. C. Adkinson, 2011: Interacting Controls on Productivity in a Northern Great Plains Grassland and Implications for Response to ENSO Events. *Global Change Biology*, **17**, 3239–3311, doi:10.1111/j.1365-2486.2011.02461.x.

Friedlingstein, P., et al., 2006: Climate-Carbon Cylce Feedback Analysis: Results from the C^4MIP Model Intercomparison. *J. Climate*, **19**, 3337–3353.

Gough, C. M., C. S. Vogel, H. P. Schmid, H.-B. Su, and P. S. Curtis, 2008: Multi-year Convergence of Biometric and Meteorological Estimates of Forest Carbon Storage. *Agric. For. Meteor.*, **148**, 158–170, doi:10.1016/j.agrformet.2007.08.004.

Gurney, K. R. and A. S. Denning, 2007: TransCom 3: Annual Mean CO2 Flux Estimates from Atmospheric Inversions (Level 1). URL `http://daac.ornl.gov/cgi-bin/dsviewer.pl?ds_id=895`, doi:10.3334/ORNLDAAC/895.

Gurney, K. R., et al., 2002: Towards Robust Regional Estimates of CO_2 Sources and Sinks Using Atmospheric Transport Models. *Nature*, **415**, 626–630.

Gurney, K. R., et al., 2004: Transcom 3 Inversion Intercomparison: Model Mean Results for the Estimation of Seasonal Carbon Sources and Sinks. *Global Biogeo. Cyc.*, **18**, GB1010, doi:10.1029/2003GB002111.

Haynes, K. D., , I. T. Baker, A. S. Denning, R. Stöckli, K. Schaefer, and E. Lokupitiya, 2013: Global Self Consistent Carbon Flux and Pool Estimates Utilizing the Simple Biosphere Model (SiB4). *Abstract B31F-01 presented at 2013, Fall Meeting, AGU*.

Hoffman, F. M., et al., 2014: Causes and implications of persistent atmospheric carbon dioxide biases in Earth System Models. *J. Geophys. Res. Biogeosci*, **119**, doi:10.

Houghton, R. A., 1999: The annual net flux of carbon to the atmosphere from changes in land use 1850-1990. *Tellus*, **51B**, 298–313.

Hurtt, G. and C. Kang, 2014: *NASA Carbon Monitoring System Phase 1 Report*. NOAA.

IPCC, 2013: *Climate Change 2013: The Physical Science Basis. Contribution of Working Group 1 to the Fifth Assessment Report of the Intergovernmental Panel on Climate Change*. Cambridge University Press, Cambridge, United Kingdom and New York, NY, USA.

Jolly, W. M., R. Nemani, and S. W. Running, 2005: An analysis of stomatal conductance. *Global Change Biol.*, **11**, 619–632.

Kaminski, T., M. Heimann, and R. Giering, 1999: A coarse grid three-dimensional global inverse model of the atmospheric transport: 2. Inversion of the transport of CO_2 in the 1980s. *J. Geophys. Res.*, **104**, 18 555–18 582.

Kawa, S. R., D. J. E. III, S. Pawson, and Z. Zhu, 2004: Global CO2 transport simulations using meteorological data from the NASA data assimilation system. *J. Geophys. Res.*, **109**, D18 312, doi:10.1029/2004JD004554.

Kljun, N., T. A. Black, T. J. Griffis, A. G. Barr, D. Gaumont-Guay, K. Morgenstern, J. H. McCaughey, and Z. Nesic, 2006: Response of Net Ecosystem Productivity of Three Boreal Forest Stands to Drought. *Ecosystems*, **9**, 1128–1144.

Krishnan, P., T. A. Black, A. G. Barr, N. J. Grant, D. Gaumont-Guay, and Z. Nesic, 2008: Factors Controlling the Interannual Variability in the Carbon Balance of a Southern Boreal Black Spruce Forest. *J. Geophys. Res.*, **113**, D09 109, doi:10.1029/2007JD008965.

Krishnan, P., T. A. Black, A. Jassal, B. Chen, and Z. Nesic, 2009: Interannual variability of the carbon balance of three different-aged Douglas-fir stands in the Pacific Northwest. *J. Geophys. Res.*, **114**, G04 011, doi:10.1029/2008JG000912.

Law, R. M., et al., 1996: Variations in modeled atmospheric transport of carbon dioxide and the consequences for CO2 inversions. *Global Biogeo. Cyc.*, **10**, 783–796.

Liu, J., et al., 2014: Carbon monitoring system flux estimation and attribution: impact of ACOS-GOSAT X_{CO2} sampling on the inference of terrestrial biospheric sources and sinks. *Tellus B*, **66**, 22 486, doi:10.3402/tellusb.v66.22486.

Lokupitiya, E., et al., 2009: Incorporation of Crop Phenology in Simple Biosphere Model (SiBcrop) to Improve Land Atmosphere Carbon Exchanges from Croplands. *Biogeosci.*, **6**, 969–986.

Lokupitiya, R. S., D. Zupanski, A. S. Denning, S. R. Kawa, K. R. Gurney, , and M. Zupanski, 2008: Estimation of global CO2 fluxes at regional scale using the Maximum Likelihood Ensemble Filter. *J. Geophys. Res.*, **113**, D20 110, doi:10.1029/2007JD009679.

Ma, S., D. D. Baldocchi, L. Xu, and T. Hehn, 2007: Inter-annual Variability in Carbon Dioxide Exchange of an oak/grass Savanna and Open Grassland in California. *Agric. For. Meteor.*, **147**, 157–171, doi:10.1016/j.agrformet.2007.07.008.

Michalak, A. M., 2008: Adapting a fixed-lag Kalman smoother to a geostatistical atmospheric inversion framework. *Atmos. Chem. Phys.*, **8**, 6789–6799.

Michalak, A. M., L. Bruhwiler, and P. P. Tans, 2004: A Geostatistical Approach to Surface Flux Estimation of Atmospheric Trace Gases. *J. Geophys. Res.*, **109**, D14 109.

Moffat, A. M., et al., 2007: Comprehensive comparison of gap-filling techniques for eddy covariance net carbon fluxes. *Agric. For. Meteor.*, **147**, 209 – 232, doi: 10.1016/j.agrformet.2007.08.011.

Peters, W., et al., 2007: An Atmospheric Perspective on North American Carbon Dioxide Exchange: CarbonTracker. *Proceedings of the National Academy of Sciences of the United States of America*, **104**, 18 925–18 930.

Peters, W., et al., 2010: Seven years of recent European net terrestrial carbon dioxide exchange constrained by atmospheric observations. *Global Change Biology*, **16**, 1317–1337.

Richardson, A. D. and D. Y. Hollinger, 2007: A method to estimate the additional uncertainty in gap-filled NEE resulting from long gaps in the CO_2 flux record. *Agric. For. Meteor.*, **147**, 199–208, doi:10.

Rödenbeck, C., S. Houweling, M. Gloor, and M. Heimann, 2003: CO_2 flux history 1982-2001 inferred from atmospheric data using a global inversion of atmospheric transport. *Atmos. Chem. Phys.*, **3**, 1919–1964.

Sabine, C. L., et al., 2004: The Oceanic Sink for Anthropogenic CO_2. *Science*, **305**, 367–371.

Schaefer, K., et al., 2012: A model-data comparison of gross primary productivity: Results from the north american carbon program site synthesis. *J. Geophys. Res.*, **117**, doi: 10.1029/2012JG001960.

Schuh, A. E., A. S. Denning, K. D. Corbin, I. T. Baker, M. Uliasz, N. Parazoo, A. E. Andrews, and D. E. J. Worthy, 2010: A regional high-resolution carbon flux inversion of North America for 2004. *Biogeosciences*, **7**, 1625–1644.

Schuh, A. E., A. S. Denning, M. Uliasz, and K. D. Corbin, 2009: Seeing the forest through the trees: Recovering large-scale carbon flux biases in the midst of small-scale variability. *J. Geophys. Res.*, **114**, G03 007, doi:10.1029/2008JG000842.

Schuh, A. E., et al., 2013: Evaluating atmospheric CO2 inversions at multiple scales over a highly-inventoried agricultural landscape. *Global Change Biology*, **19**, 1424–1439, doi: 10.1111/gcb.12141.

Sellers, P. J., S. O. Los, C. J. Tucker, C. O. Justice, D. A. Dazlich, G. J. Collatz, and D. A. Randall, 1996a: A Revised Land Surface Parameterization (SiB2) for Atmospheric GCMs. Part II: The Generation of Global Fields of Terrestrial Biophysical Parameters from Satellite Data. *J. Climate*, **9(4)**, 706–737.

Sellers, P. J., Y. Mintz, Y. C. Sud, and A. Dalcher, 1986: A Simple Biosphere Model (SiB) for Use within General Circulation Models. *J. Atmos. Sci.*, **275**, 502–509.

Sellers, P. J., Y. Mintz, Y. C. Sud, and A. Dalcher, 1992: Canopy Reflectance, Photosynthesis, and Transpiration. III. A Reanalysis Using Improved Leaf Models and a New Canopy Integration Scheme. *Rem. Sens. Enviro.*, **42**, 187–216.

Sellers, P. J., et al., 1996b: A Revised Land Surface Parameterization (SiB2) for Atmospheric GCMs Part I: Model Formulation. *J. Climate*, **9**, 676–705.

Stöckli, R., T. Rutishauser, I. Baker, M. A. Liniger, and A. S. Denning, 2011: A global reanalysis of vegetation phenology. *J. Geophys. Res.*, **116**, G03 020, doi:10.1029/2010JG001545.

Stöckli, R., T. Rutishauser, P. E. Thornton, L. Lu, and A. S. Denning, 2008: Remote sensing data assimilation for a prognostic phenology model. *J. Geophys. Res.*, **113**, G04 021, doi: 10.1029/2008JG000781.

Suyker, A. E. and S. B. Verma, 2010: Coupling of Carbon Dioxide and Water Vapor Exchanges of Irrigated and Rainfed Maize-Soybean Cropping Systems and Water Productivity. *Agric. For. Meteor.*, **150**, 553563, doi:10.1016/j.agrformet.2010.01.020.

Tans, P. P., I. Y. Fung, and T. Takahashi, 1990: Observational Constraint on the Global Atmospheric CO_2 Budget. *Science*, **247**, 1431–1438.

UNH, 2014: Pools, Fluxes, and a Word about Units. URL `http://globecarboncycle.unh.edu/CarbonPoolsFluxes.shtml`.

Urbanski, S., et al., 2007: Factors Controlling CO2 Exchange on Timescales from Hourly to Decadal at Harvard Forest. *J. Geophys. Res.*, **112**, G02 020, doi:10.1029/2006JG000293.

Verma, S. B., et al., 2005: Annual Carbon Dioxide Exchange in Irrigated and Rainfed Maize-based Agroecosystems. *Agric. For. Meteor.*, **131**, 77–96, doi:10.1016/j.agrformet.2005.05.003.

Welch, G. and G. Bishop, cited 2006: An Introduction to the Kalman Filter. University of North Carolina at Chapel Hill, Available online at http://www.cs.unc.edu/ welch/media/pdf/kalman_intro.pdf.

Zhang, F., C. Snyder, and J. Sun, 2004: Impacts of Initial Estimate and Observation Availability on Convective-Scale Data Assimilation with an Ensemble Kalman Filter. *Mon. Wea. Rev.*, **132**, 1238–1253, doi:http://dx.doi.org/10.1175/1520-0493(2004)132⟨1238:IOIEAO⟩2.0.CO;2.

Zupanski, D., et al., 2007: Carbon flux bias estimation employing Maximum Likelihood Ensemble Filter (MLEF). *J. Geophys. Res.*, **112**, D17 107, doi:10.1029/2006JD008371.